

# Multiloop Pseudofermion Functional Renormalization Group Study of the Heisenberg Model with Dipolar Interactions on the Triangular and Square Lattice

Gün Günal



Master's thesis  
Faculty of Physics  
Ludwig-Maximilians-Universität Munich  
Supervisor: Prof. Dr. Jan von Delft

Munich, 22 May 2023



Eine Analyse des  
Heisenberg-Modells mit dipolaren  
Wechselwirkungen auf dem  
dreieckigen und quadratischen  
Gitter anhand pseudofermionischer  
Multischleifen-FRG

Gün Günal



Masterarbeit  
Fakultät für Physik  
Ludwig-Maximilians-Universität München  
Betreuer: Prof. Dr. Jan von Delft

München, den 22 Mai 2023



## Abstract

In this thesis, we utilize the multiloop pseudofermion functional renormalization group method to investigate the Heisenberg model with dipolar interactions on the square and triangular lattice in the zero temperature limit. We compare our results with previous studies conducted using the pseudofermion functional renormalization group [1, 2] and we observe good agreement with their results. However, our work reveals an extended region for the disordered regime that was not captured in previous studies. In the second part of this thesis, we establish a correspondence between the cut-off function used in the functional renormalization group and the impurity Hamiltonian. We conduct a benchmark study by comparing our results with exact diagonalization for the antiferromagnetic Heisenberg dimer and the density matrix renormalization group for the antiferromagnetic Heisenberg chain. The comparison reveals good agreement between the methods in the weak coupling regime.



---

## Acknowledgments

I would like to thank Jan von Delft for supervising my thesis and allowing me to work on this project.

I'm incredibly grateful to Marc Ritter for his endless patience. His guidance and feedback have been crucial in the development of this project.

I would like to extend my thanks to Benedikt Schneider, Marc Ritter, and Björn Sbierski for coming up with the idea for the benchmark project and helping me with fRG-related problems whenever I needed it. I also thank them for the pleasant conversation we had at the mensa. I would like to acknowledge Andreas Gleis for his contributions to generating the DMRG data for the benchmark project and for the valuable discussions we had throughout the course of this work.

I am grateful to thank Marc, Filippo, and Nepomuk for proof-reading my thesis and providing valuable feedback on short notice.

I would like to thank my office mates Dim, Alex, Nick, Korbi, Ming, and Frederic for creating an enjoyable work environment. I thank all my colleagues in the theoretical solid-state physics and the theoretical nanophysics chair for their stimulating conversations during coffee breaks.

I would like to thank Mali and Arda for their insightful discussions on physics and non-physics topics. Their friendship has been invaluable throughout the years. I would like to acknowledge the financial support provided by DAAD (German Academic Exchange Service) for funding my master's studies. I would also like to express my gratitude to the developers of Grammarly and ChatGPT. I have used their services for proofreading and improving the readability of my thesis.

Lastly, I would like to thank my parents and Uğur for listening to my endless complaints even when things are going well.



---

# Contents

<b>Contents</b>	<b>v</b>
<b>1 Introduction</b>	<b>1</b>
<b>2 Theoretical Background</b>	<b>3</b>
2.1 Physical Model . . . . .	3
2.1.1 Quantum Spin Liquids . . . . .	3
2.1.2 Heisenberg Model . . . . .	4
2.2 Multiloop Pseudofermion Functional Renormalization Group . . . . .	5
2.2.1 Pseudofermion Construction . . . . .	6
2.2.2 Preliminary Definitions . . . . .	8
2.2.3 Parquet Formalism . . . . .	9
2.2.4 Multiloop Functional Renormalization Group . . . . .	10
2.2.5 Cutoff Procedure . . . . .	11
2.2.6 Flow Equations . . . . .	12
<b>3 Implementation</b>	<b>15</b>
3.1 Symmetries of the Pseudofermion Action . . . . .	15
3.1.1 Local SU(2) Gauge Redundancy . . . . .	16
3.1.2 Physical Symmetries . . . . .	18
3.1.3 Parameterization of Correlators . . . . .	18
3.1.4 Lattice Symmetries . . . . .	20
3.1.5 Asymptotic Classes . . . . .	22
3.2 Spin Susceptibility . . . . .	25
<b>4 Results</b>	<b>29</b>
4.1 Triangular Lattice . . . . .	29
4.1.1 Next-Nearest-Neighbor Interactions . . . . .	29
4.1.2 Long-range Interactions . . . . .	31
4.2 Square Lattice . . . . .	41

## Contents

---

4.2.1	Next-Nearest-Neighbor Interactions . . . . .	41
4.2.2	Long-range Interactions . . . . .	44
4.3	Discussion . . . . .	53
<b>5</b>	<b>Benchmark</b>	<b>57</b>
5.1	Approximations of pffRG . . . . .	57
5.1.1	Lattice Size Truncation . . . . .	58
5.1.2	Frequency Discretization . . . . .	58
5.1.3	Fulfillment of the Pseudofermion Constraint . . . . .	59
5.1.4	Cutoff Dependence . . . . .	60
5.1.5	Parquet Approximation . . . . .	60
5.1.6	Truncation of Six-point Vertex . . . . .	61
5.2	Physical Interpretation of the Cutoff Function . . . . .	62
5.3	Dimer . . . . .	64
5.4	Infinite Chain . . . . .	66
5.5	Discussion . . . . .	69
<b>6</b>	<b>Summary and Outlook</b>	<b>71</b>
	<b>Bibliography</b>	<b>73</b>

## Introduction

Quantum spin liquids are a novel phase of matter with fascinating features such as anyonic excitations, high degree of entanglement, topological order, and absence of long-range order [3]. This phase can emerge in spin models with geometric frustration, such as the antiferromagnetic Heisenberg model on frustrated geometries. Previously, Thönni et al. has studied this model on the Kagome lattice using the multiloop pseudofermion functional renormalization group [4, 5]. In this thesis, we employ the same method to investigate the Heisenberg model on both the triangular and square lattice, considering both short-range and long-range interactions.

The antiferromagnetic Heisenberg model on the triangular lattice has been extensively studied using various methods involving density matrix renormalization group [6–9], variational Monte Carlo [10] and pseudofermion functional renormalization group [10]. Previous studies of the antiferromagnetic Heisenberg model with short-range interactions [6–10] have suggested the existence of a magnetically disordered state that could be a quantum spin liquid. In this thesis, first we briefly study the short-range interactions and then we turn to a more extensive analysis of the long-range interactions. We compare our findings with the existing literature both on the short-range [6–10] and long-range interactions [1, 11].

Similarly, the antiferromagnetic Heisenberg model on the square lattice is another candidate for hosting a quantum spin liquid phase. Indeed, previous studies employing density matrix renormalization group [12, 13], projected entangled pair states [14], exact diagonalization [15] and pseudofermion functional renormalization group [16] have identified a regime that exhibits characteristics of a quantum spin liquid. Analogous to our triangular lattice study, we also conduct a brief investigation of this model with the short-range interactions and compare our findings with the previous studies [12–15]. Subsequently, we explore the effects of long-range interactions and compare our results with Refs. [2, 17].

To study these models, we employ a method that combines the pseudofermion functional renormalization group originally developed by Reuther and

Wölfle [16, 18, 19], with the extension of the multiloop functional renormalization group developed by Kugler and von Delft [20–23] to study the AFM Heisenberg model on the triangular and the square lattice.

The thesis is structured as follows. In Chapter 2, after giving a concise overview of quantum spin liquids and the Heisenberg model, we explain the multiloop pseudofermion functional renormalization group method. We start our explanation by discussing the pseudofermion representation of the spin operators. Then we discuss the building blocks of the multiloop functional renormalization group following Refs. [20–24].

In Chapter 3, we discuss the numerical implementation of this method previously accomplished by Ritter [24] and Thönnißen [4].

In Chapter 4, we present our results obtained for short and long-range interactions for the Heisenberg model on the triangular and square lattice. Then we proceed to compare our results with the existing literature on the long-range interactions by Keles and Zhao [1, 2, 25].

In Chapter 5, we devise a way to test the validity range of our method by comparing it to other powerful methods, namely the exact diagonalization and the density matrix renormalization group. Our group members Sbierski, Schneider and Ritter developed the idea for this comparison. In this chapter, we discuss the approximations done in previous chapters and present our benchmark results.

Finally, we give an overview of our results and an outlook on further research directions in Chapter 6.

## Theoretical Background

In this chapter, we begin by providing a brief overview of the exotic phase of matter known as the quantum spin liquids. We then discuss the antiferromagnetic Heisenberg model on the triangular and square lattice.

In the second part of this chapter, we offer a concise overview of the pseudofermion functional renormalization group (pffRG) formalism. To achieve this, we first describe the pseudofermion representation of the Heisenberg Hamiltonian. Subsequently, we discuss some preliminary field-theoretical objects that are essential to the construction of the functional renormalization group method. Following that, we touch upon the parquet formalism, which serves as the foundation for the multiloop functional renormalization group. Lastly, we present an overview of the multiloop functional renormalization group by examining the cutoff procedure and the flow equations.

### 2.1 Physical Model

#### 2.1.1 Quantum Spin Liquids

Quantum spin liquids (QSL) are an exotic phase of matter that can be found in frustrated spin systems. These materials are hard to identify both experimentally and theoretically, as they don't have a characteristic local order parameter and don't break the symmetries of the Hamiltonian [3]. They may exhibit unique properties such as topological order, anyonic excitations and also they have a high degree of entanglement [3]. Despite these challenges, we know about their existence and their potential applications. Kitaev demonstrated that the topological order of these unique phases might play an important role in quantum computation and proposed an exactly solvable model on a torus and honeycomb lattice [3, 26, 27], which established the existence and usefulness of QSL.

The first proposal of QSL was for the spin 1/2 antiferromagnetic Heisenberg model on the triangular lattice by Anderson [28]. The triangular lattice

## 2. Theoretical Background

---

exhibits a geometric frustration, which makes finding the ground state of Hamiltonians with antiferromagnetic interactions challenging on this lattice. The geometric frustration is illustrated in Figure 2.1 with an example. For this reason, Anderson proposed resonating valence bond (RVB) state as the ground state of the AFM triangular lattice. The RVB state is composed of two spins forming a spin-0 singlet. By taking the superposition of all configurations of these singlets, a ground state for AFM Heisenberg Hamiltonian can be established on the triangular lattice without breaking the translational invariance. Although it was discovered that the ground state of the AFM Heisenberg model on triangular lattice is not a RVB state, the idea of searching QSL in frustrated geometries persisted [3, 4, 29].

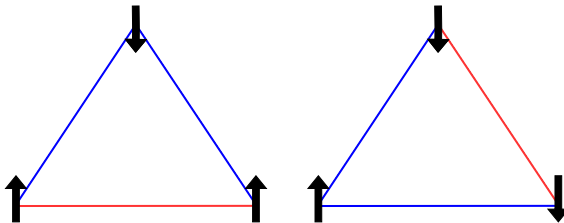


Figure 2.1: An example of geometric frustration on the triangular lattice with antiferromagnetic interaction is illustrated. The excited bonds represented by red lines. As illustrated, there is no configuration in which all three neighboring spins are anti-parallel [30].

### 2.1.2 Heisenberg Model

One of the simplest model for studying frustrated spins is the antiferromagnetic Heisenberg model with nearest-neighbor (NN) and next-nearest-neighbor (NNN) interactions:

$$H = J_1 \sum_{i,j \in NN} \mathbf{S}_i \cdot \mathbf{S}_j + J_2 \sum_{i,j \in NNN} \mathbf{S}_i \cdot \mathbf{S}_j. \quad (2.1)$$

In Eq. (2.1), the first sum is over nearest-neighbors, while the second sum is over next-nearest-neighbors. For the antiferromagnetic model, both  $J_1$  and  $J_2$  are positive.

In this thesis, our initial focus is on the study of the AFM NNN Heisenberg model on triangular lattice using the pseudofermion functional renormalization group (pffRG) approach at  $T = 0$ . Although this model has already been extensively studied using other powerful numerical methods such as Density Matrix Renormalization group (DMRG) [8, 9], pffRG and variational Monte Carlo (VMC) [10], which have discovered a QSL ground state, the nature of this QSL remains a topic of debate. We present our results obtained for phase boundaries of this model using pffRG in Chapter 4.1.1.

The AFM NNN Heisenberg model on the square lattice is also another candidate for having a QSL as a ground state. Although the model is not frustrated with only NN interactions, the inclusion of NNN interactions introduces frustration. This model has been widely studied using other methods including DMRG [12, 13], exact diagonalization (ED) [15], pffRG [16] and more recently with the projected entangled pair states (PEPS) [14]. While the nature of this QSL regime is still under debate, in the recent publication by Liu et al. [14], the authors suggest the presence of a gapless QSL and a valence bond solid (VBS) between the two ordered phases. We utilize the results obtained from other methods to use as a rough benchmark for our method when determining the appropriate types of order.

In this thesis, our main focus will be on the Heisenberg model with dipolar interactions on the triangular and square lattice. The Hamiltonian for this model is defined as [1, 2, 11, 17]

$$H = \frac{1}{2} \sum_{ij} J_{ij} S_i \cdot S_j, \quad (2.2)$$

where the sum is over all lattice sites and  $J_{ij}(\theta, \phi)$  is the dipolar interaction between two lattice sites. This interaction is defined as

$$J_{ij}(\theta, \phi) = J_0 \frac{(1 - 3(\hat{r}_{ij} \cdot \hat{d})^2)}{r_{ij}^3}. \quad (2.3)$$

Here,  $r_{ij}$  represents the displacement vector between lattice sites  $i$  and  $j$ , and  $\hat{d}$  denotes the unit vector for dipole alignment.

$$\hat{d} = (\sin \theta \cos \phi, \sin \theta \sin \phi, \cos \theta). \quad (2.4)$$

Adjusting the alignment of the dipoles enables variation in the interactions between lattice sites, providing two tunable parameters,  $\theta$  and  $\phi$ . These parameters can be used to increase the frustration of the model, giving rise to a paramagnetic phase [1, 2, 11, 17].

Previously, the dipolar Heisenberg model was studied on the triangular and the kagome lattice using DMRG in Ref. [11], using PEPS for the square lattice in Ref. [17] and using pffRG for the triangular lattice in Ref. [1] and for the square lattice Ref. [2]. In this thesis, we study the dipolar interactions for the triangular and square lattices using pffRG and compare our findings with those in Refs. [1, 2] in Chapter 4.

## 2.2 Multiloop Pseudofermion Functional Renormalization Group

In this section we give a brief overview of the multiloop pseudofermion functional renormalization group (mpffRG). We begin by discussing the pseudofermion representation of the Heisenberg Hamiltonian. Next, we define several

## 2. Theoretical Background

---

fundamental objects used in the functional renormalization group. Subsequently, we introduce a set of equations comprised of two particle reducible diagrams, known as the parquet equations. Following this, we offer a brief overview of the multiloop functional renormalization group.

### 2.2.1 Pseudofermion Construction

Parton construction is an important tool used in condensed matter physics to investigate spin Hamiltonians. This approach involves replacing the spin operator in the Hamiltonian with fermionic, bosonic or a combination of both types of creation and annihilation operators [3].

For our purpose, we will utilize Abrikosov's pseudofermion representation, which amounts to re-writing the spin  $\frac{1}{2}$  operators in terms of fermionic creation and annihilation operators [31]. This representation allows us to use the well-established fermionic path integrals and Feynman diagrammatic methods which are the essential tools for building functional renormalization group for fermions [18, 19].

The spin operator  $S$  in pseudofermion representation is represented as

$$S_i^\mu = \frac{1}{2} \sum_{\alpha\beta} f_{i\alpha}^\dagger \sigma_{\alpha\beta}^\mu f_{i\beta}. \quad (2.5)$$

Above  $i$  is the lattice site index,  $\sigma^\mu$  are the Pauli matrices with  $\mu = x, y, z$ , and  $f$  are the fermionic annihilation and creation operators with indices  $\alpha, \beta = \uparrow, \downarrow$ . Note that in this representation, the spin algebra is still satisfied by pseudofermions, i.e.,  $[S_i^\mu, S_j^\nu] = i\delta_{ij}\epsilon_{\mu\nu\lambda}S_i^\lambda$ .

Now if we write the Heisenberg Hamiltonian in terms of pseudofermion operators, we obtain:

$$H = \frac{1}{8} \sum_{\mu\nu} \sum_{ij} \sum_{\alpha\beta\alpha'\beta'} J_{ij}^{\mu\nu} f_{i\alpha}^\dagger \sigma_{\alpha\beta}^\mu f_{i\beta} f_{j\alpha'}^\dagger \sigma_{\alpha'\beta'}^\nu f_{j\beta'}. \quad (2.6)$$

However, the pseudofermion construction introduces two new features that one must account for; enlargement of the Hilbert space and external  $SU(2)$  gauge redundancy [19]. We will deal with the latter in the later chapters.

For each site  $i$ , the original Hilbert space is spanned by two vectors,  $\{|\uparrow\rangle, |\downarrow\rangle\}$ . However, with pseudofermion construction, the Hilbert space is enlarged and spanned by four vectors,  $\{|0\rangle, |\uparrow\downarrow\rangle, |\uparrow\rangle, |\downarrow\rangle\}$ . The unoccupied state  $|0\rangle$  and the doubly occupied state  $|\uparrow\downarrow\rangle$  have no correspondence in the original system, thus, they are deemed unphysical.

To stay in the physically relevant sector of the Hilbert space, a projection

$$P_i = \sum_{\alpha} f_{i\alpha}^\dagger f_{i\alpha} = 1, \quad (2.7)$$

## 2.2. Multiloop Pseudofermion Functional Renormalization Group

---

can be applied at each lattice site. However, this constraint is difficult to enforce numerically, and instead, it is replaced by a weaker constraint [16, 24],

$$\langle P_i \rangle = \sum_{\alpha} \langle f_{i\alpha}^{\dagger} f_{i\alpha} \rangle = 1. \quad (2.8)$$

In order to apply the constraint (2.8), we first need to normal order the Heisenberg Hamiltonian using the fermionic anti-commutation relations,  $\{f_{i\alpha}^{\dagger}, f_{j\beta}\} = \delta_{ij}\delta_{\alpha\beta}$ .

$$\begin{aligned} H &= \frac{1}{8} \sum_{\mu\nu ij} \sum_{\alpha\beta\alpha'\beta'} J_{ij}^{\mu\nu} \sigma_{\alpha\beta}^{\mu} \sigma_{\alpha'\beta'}^{\nu} f_{i\alpha}^{\dagger} f_{j\alpha'}^{\dagger} f_{i\beta} f_{j\beta'} \\ &\quad + \frac{1}{8} \sum_{\mu\nu ij} \sum_{\alpha\beta\alpha'\beta'} J_{ij}^{\mu\nu} \sigma_{\alpha\beta}^{\mu} \sigma_{\alpha'\beta'}^{\nu} f_{i\alpha}^{\dagger} \delta_{ij} \delta_{\beta\alpha'} f_{j\beta'} \\ &= \frac{1}{8} \sum_{\mu\nu ij} \sum_{\alpha\beta\alpha'\beta'} J_{ij}^{\mu\nu} \sigma_{\alpha\beta}^{\mu} \sigma_{\alpha'\beta'}^{\nu} f_{i\alpha}^{\dagger} f_{j\alpha'}^{\dagger} f_{i\beta} f_{j\beta'} + \frac{1}{8} \sum_{\mu\nu i} \sum_{\alpha\beta'} J_{ii}^{\mu\nu} f_{i\alpha}^{\dagger} f_{i\beta'} \underbrace{\sum_{\beta} \sigma_{\alpha\beta}^{\mu} \sigma_{\beta\beta'}^{\nu}}_{\delta^{\mu\nu} \delta_{\alpha\beta'} + i\epsilon_{\mu\nu\nu} \sigma_{\alpha\beta}^{\nu}} \\ &= \frac{1}{8} \sum_{\mu\nu ij} \sum_{\alpha\beta\alpha'\beta'} J_{ij}^{\mu\nu} \sigma_{\alpha\beta}^{\mu} \sigma_{\alpha'\beta'}^{\nu} f_{i\alpha}^{\dagger} f_{j\alpha'}^{\dagger} f_{i\beta} f_{j\beta'} + \frac{1}{8} \sum_{\mu i} \sum_{\alpha} J_{ii}^{\mu\mu} f_{i\alpha}^{\dagger} f_{i\alpha}. \quad (2.9) \end{aligned}$$

In the last line, we have used  $J^{\mu\nu} = J^{\nu\mu}$  and the multiplication of symmetric and anti-symmetric tensor is identically equal to 0, i.e.,  $J^{\mu\nu} \epsilon_{\mu\nu\nu} = 0$ .

The last term in Eq. (2.9) can be interpreted as a shift in the chemical potential in the grand canonical ensemble. To fulfill the projection scheme proposed in Eq. (2.8), the chemical potential can be tuned into particle-hole symmetric value,  $\mu = 0$ , which disfavors the unphysical states [16]. In other words, adding or subtracting fermions from the system with particle-hole symmetry is energetically unfavorable at  $T = 0$ .

Another way to apply this constraint is using a trick developed by Popov and Fedetov [32]. This trick can be applied by coupling the Hamiltonian with an imaginary valued chemical potential such as  $H_{\text{pf}} = -\frac{i\pi T}{2}(n_{\uparrow} + n_{\downarrow} - 1)$ . At first glance, for  $T \rightarrow 0$ , the Popov-Fedetov and pseudofermion projection scheme Eq. (2.8) might appear to be identical. However, this is not the case. The partition function of the Popov-Fedetov is always equal to the partition of the original spin system; meanwhile, in the pseudofermion projection scheme, they differ [18, 33].

In this thesis, we will not use the Popov-Fedetov trick; for further details on the implementation of the Popov-Fedetov trick to pseudofermion functional renormalization group and why both methods are not equivalent at  $T \rightarrow 0$  limit, see Ref. [33].

### 2.2.2 Preliminary Definitions

For the construction of fRG machinery, we need to define some field theoretical objects. For this purpose we start by defining the partition function  $Z$  as an integral over the Grassmann fields  $\psi$  and  $\bar{\psi}$  as,

$$Z = \int D[\psi, \bar{\psi}] e^{-S[\psi, \bar{\psi}]}, \quad (2.10)$$

where  $S[\psi, \bar{\psi}]$  is the action. And the action is defined as,

$$S[\psi, \bar{\psi}] = - \sum_{1',1} \bar{\psi}_{1'} G_0^{-1}(1'; 1) \psi_1 - \frac{1}{4} \sum_{1',2';1,2} \Gamma_0(1', 2'; 1, 2) \bar{\psi}_1 \bar{\psi}_2 \psi_1 \psi_2, \quad (2.11)$$

where the sum is over all quantum numbers, including the Matsubara frequencies, spin, and lattice site indices, and they should be considered as integrals for continuous variables and sum for discrete variables [21, 24]. Because the pseudofermion Hamiltonian has no kinetic term, the bare two-point Green's function is

$$G_0(i\omega) = \frac{1}{i\omega}, \quad (2.12)$$

where the chemical potential is set to  $\mu = 0$ , due to the pseudofermion constraint [4, 18, 24]. The  $\Gamma_0$  in Eq. (2.11) is the bare vertex, which is anti-symmetric under the exchange of indices. Additionally, we need to define the full two-point Green's function as,

$$G^{(2)}(1'; 1) = -\langle \psi_1 \bar{\psi}_1 \rangle = \frac{-1}{Z} \int D[\psi, \bar{\psi}] \psi_1 \bar{\psi}_1 e^{-S[\psi, \bar{\psi}]} \quad (2.13)$$

and similarly the four-point Green's functions as,

$$G^{(4)}(1', 2'; 1, 2) = \langle \psi_1 \psi_2 \bar{\psi}_2 \bar{\psi}_1 \rangle, \quad (2.14)$$

or the 2n-point Green's function as,

$$G^{(2n)}(1', 2' .. n'; 1, 2 .. n) = \langle \psi_1 \psi_2 \dots \psi_n \bar{\psi}_n \dots \bar{\psi}_2 \bar{\psi}_1 \rangle. \quad (2.15)$$

Moreover, we can re-write the two-point Green's function the using self-energy,  $\Sigma$ , with the help of the Dyson equation [21, 24, 34]

$$G = G_0 + G_0 \cdot \Sigma \cdot G \iff G^{-1} = G_0^{-1} - \Sigma, \quad (2.16)$$

and the four-point correlator using the full vertex as [21, 24, 34]

$$\begin{aligned} G^{(4)}(1'2'; 1, 2) &= G(1'; 1)G(2'; 2) - G(1'; 2)G(2'; 1) \\ &+ \sum_{3'4'34} G(1', 3)G(2', 4)\Gamma(3, 4; 3'4')G(3', 1)G(4', 2). \end{aligned} \quad (2.17)$$

The minus sign in the second term of Equation (2.17) account for the anti-commutation of two Grassmann fields. Similarly under odd permutation of indices both  $G^{(4)}$  and  $\Gamma$  pick up a minus sign.

Finally, we give one last definition. An n-particle irreducible diagram is a diagram that cannot be reduced into two disconnected diagrams cutting n lines. Examples of these diagrams are given in Fig. 2.2.

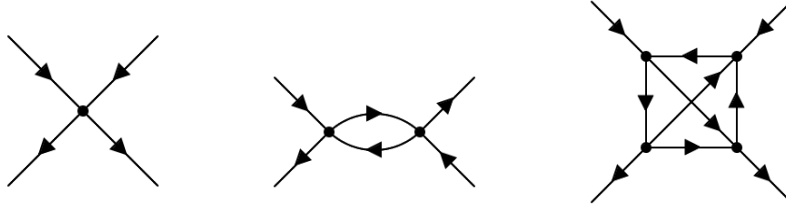


Figure 2.2: The first diagram is the bare vertex denoted by  $\Gamma_0$ . The second diagram is a 1-particle irreducible diagram and 2-particle reducible diagram. The last diagram is a 2-particle irreducible diagram also known as the envelope diagram.

### 2.2.3 Parquet Formalism

Using the definitions provided in the previous section, we can decompose the four-point vertex defined in Eq. (2.17) into three topologically distinct two-particle reducible channels  $\gamma_r$  and one two-particle irreducible channel,  $R$ .

$$\Gamma = R + \gamma_a + \gamma_t + \gamma_p, \quad (2.18)$$

The subscript  $r$  of  $\gamma_r$  denotes in which channel the diagram is reducible. The indices a,t, and p stand for anti-parallel, transverse, and parallel respectively, specifying in which channel they are reducible. Using Eq. (2.18) we can write the two-particle irreducible in channel  $r$  as

$$I_r = \Gamma - \gamma_r = R + \sum_{r \neq r'} \gamma'_r. \quad (2.19)$$

The Eq. (2.19) allows us to define Bethe-Salpeter equations (BSEs) in algebraic form as

$$\gamma_r = I_r \cdot \Pi_r \cdot \Gamma. \quad (2.20)$$

Here,  $\Pi_r$  is made out of a pair of propagators and connected to the vertices in channel  $r$  [5, 20–24].

However, the Bethe-Salpeter equations need an input for  $R$  to provide a self-consistent set of equations. In our study, we adopt the simplest approximation called the parquet approximation, which sets irreducible vertex to bare vertex, i.e.,  $R = \Gamma_0$ . A more complicated choice for  $R$  would increase the method's complexity and its numerical cost [20]. Using the parquet approximation, we obtain a set of self-consistent Bethe-Salpeter equations that are exact up to fourth-order perturbation theory and also include diagrams from higher orders. The envelope diagram, illustrated in Fig. 2.2, is the first diagram excluded by this approximation in the perturbation series.

## 2. Theoretical Background

---

Additionally, we define the Schwinger-Dyson equation(SDE) which is the equation of motion for the Green's function [21].

$$\begin{aligned} \Sigma(1'; 1) = & - \sum_{2'2} \Gamma_0(1', 2'; 1, 2)G(2; 2') \\ & + \frac{1}{2} \sum \Gamma_0(1', 2'; 3, 4)G(2; 2')G(3; 3')G(4; 4')\Gamma(4'3'; 1, 2). \end{aligned} \quad (2.21)$$

The repeated indices are summed over in Eq.(2.21) to make the notation compact. The derivation of SDE in fRG context can be found in Ref. [21]. With the SDE at hand, we can relate the self-energy to the vertex as well [21].

SDE combined with BSEs forms a set of equations that can be solved self-consistently, known as the parquet equations [21, 24]. One way to solve these self-consistent equations for a fixed point is through iteration until convergence to a fixed point occurs. However, this is not always numerically feasible, especially in the high coupling regime, for which we use the functional renormalization group. For implementation details of solving parquet equations in our work, we refer the reader to [5, 24], and for theoretical details to [20, 21].

### 2.2.4 Multiloop Functional Renormalization Group

The functional renormalization group (fRG) is a powerful tool employed for studying interacting fermions in condensed matter physics. As fRG is a non-perturbative method, it is useful for investigating the highly correlated systems where the perturbation theory breaks down. fRG conceptually builds on the Wilsonian renormalization group, as both methods share the common strategy of integrating out the higher energy modes of the theory [18, 21].

In summary, the Wilsonian RG procedure consists of three steps. Starting from the partition function, the first step is the elimination of higher energy modes of the theory. This is done by integrating out the higher energy fields. The second step is rescaling the fields to obtain a rescaled action that has the same form as the initial action. As a result, the action has new coupling parameter due to the change in Hamiltonian. Finally, the third and the last step is to analyze the flow of these parameters under iteration of steps one and two which provides insight into the behavior of the system at different energy scales [34, 35].

The fRG, similar to Wilsonian RG, iteratively eliminates the high-energy modes of the theory. However, instead of starting out with the partition function and eliminating the high-energy modes by integration, the fRG formalism couples the bare propagator to a scale-dependent cutoff function. This approach allows fRG to investigate systems where the functional integral in step one of Wilsonian RG is inaccessible [21]. In fRG, instead of the coupling parameters, objects such as self-energy and vertex flow are considered. The equations governing the behavior of these objects are called the flow equations.

In the following sections, we will briefly discuss the multiloop pseudofermion functional renormalization group using the parquet formalism discussed in Chapter 2.2.3, and examine the flow equations for the vertex and self-energy functions. For a general treatment of fRG, we refer the reader to [34]. The upcoming sections summarize the previous master's theses written on mpffRG by Marc Ritter [24] and Julian Thönniß [4].

### 2.2.5 Cutoff Procedure

To carry out the fRG procedure, the bare propagator  $G_0$  is transformed into a scale dependent function by artificially introducing a cutoff function as follows:

$$G_0^\Lambda(\omega) = \begin{cases} G_0(\omega), & \Lambda \rightarrow 0, \\ 0, & \Lambda \rightarrow \infty. \end{cases} \quad (2.22)$$

This modification leads to the bare propagator becoming a function of  $\Lambda$ ,  $G_0 \rightarrow G_0^\Lambda$ . It is important to recall that the Gaussian part (first term) of the action defined in Eq. (2.11), depends on  $G_0$ . As a result, the action also evolves into a function of  $\Lambda$  i.e,  $S \rightarrow S^\Lambda$ , and the original theory is recovered for  $\Lambda \rightarrow 0$ . Conversely, when  $\Lambda \rightarrow \infty$ , the Gaussian part of the action is suppressed, providing a simple initial condition [34, 36].

As the most of the functions defined in Sec. 2.2.2 depend on the bare propagator, they also become functions of  $\Lambda$ . For example,  $\Gamma \rightarrow \Gamma^\Lambda$ ,  $\Sigma \rightarrow \Sigma^\Lambda$  or  $\gamma_r \rightarrow \gamma_r^\Lambda$ . However, the irreducible vertex  $R$  in the parquet approximation does not depend on the bare propagator, and thus, it is not a function of  $\Lambda$ .

In this thesis we use a multiplicative cutoff function:

$$G_0^\Lambda = \Theta^\Lambda(|\omega| - \Lambda)G_0(\omega), \quad (2.23)$$

where  $\Theta(|\omega| - \Lambda)$  is the regulator and defined as

$$\Theta(|\omega| - \Lambda) = \begin{cases} 0, & |\omega| \ll \Lambda, \\ 1, & |\omega| \gg \Lambda. \end{cases} \quad (2.24)$$

The choice of cutoff function  $\Theta^\Lambda(|\omega| - \Lambda)$  is not unique. Any function that satisfies the condition (2.22) can be used. Since the cutoff function is included to the bare propagator artificially, the physics should not depend on the choice of cutoff. At  $\Lambda \rightarrow 0$ , the original theory should be recovered. However, this does not hold for the conventional fRG treatment in the literature. The flow can diverge before reaching to  $\Lambda = 0$ , and results might deviate from the original theory [23]. In Chapter 5, we discuss more in detail how the cutoff dependence can change the interpretation of the physical results.

In the first part of this thesis, where we investigate the AFM Heisenberg model on square and triangular lattices, we employ the Gaussian cutoff function for our calculations:

$$\Theta^\Lambda(\omega) = 1 - e^{-\omega^2/\Lambda^2}. \quad (2.25)$$

## 2. Theoretical Background

---

Another suitable choice of multiplicative cutoff is the Lorentzian cutoff,

$$\Theta^\Lambda(\omega) = \frac{\omega^2}{\omega^2 + \Lambda^2}, \quad (2.26)$$

which will be relevant in the second part of this thesis

A different strategy for implementing this artificial cutoff is through the use of an additive cutoff

$$G_0^{-1,\Lambda} = G_0^{-1} - A^\Lambda. \quad (2.27)$$

In order to fulfill Eq (2.22), the function  $A$  is chosen such that  $\Lambda \rightarrow \infty$ ,  $R \rightarrow \infty$  and when  $\Lambda \rightarrow 0$ ,  $R \rightarrow 0$  [34, 36].

### 2.2.6 Flow Equations

This section is primarily based on the work of Kugler and von Delft [20, 22] as well as the master thesis of Marc K. Ritter [24] and Julian Thönniß [4].

In fRG, analogous to the flow parameters in the Wilsonian RG that evolve with each RG step, there are functions that evolve with the  $\Lambda$  scale. Our main focus will be on the flow of the four-point vertex  $\Gamma$  and the flow of the self-energy  $\Sigma$ . To analyze the flow of these functions with respect to the change in  $\Lambda$ , we examine their derivatives. For brevity, we omit the  $\Lambda$  superscript in the following equations.

$$\partial_\Lambda \Gamma = \partial_\Lambda R + \sum_r \partial_\Lambda \gamma_r = \sum_r \dot{\gamma}_r. \quad (2.28)$$

Here, we have used Eq. (2.18) along with the fact that the irreducible vertex  $R$  is just the bare vertex  $\Gamma_0$  within the parquet approximation. As a result, it is independent of  $\Lambda$  meaning  $\partial_\Lambda R = \dot{R} = 0$ .

Next, we examine the two-particle reducible diagram in the r-channel:

$$\begin{aligned} \dot{\gamma}_r &= \partial_\Lambda (I_r \cdot \Pi_r \cdot \Gamma) = \dot{I}_r \cdot \Pi_r \cdot \Gamma + I_r \cdot \dot{\Pi}_r \cdot \Gamma + I_r \cdot \Pi_r \cdot \dot{\Gamma} \\ &= \dot{I}_r \cdot \Pi_r \cdot \Gamma + I_r \cdot \dot{\Pi}_r \cdot \Gamma + I_r \cdot \Pi_r \cdot (\dot{I}_r + \dot{\gamma}_r). \end{aligned} \quad (2.29)$$

Here we have used  $\Gamma = I_r + \gamma_r$ . By gathering all terms with  $\dot{\gamma}_r$  on the left side, we obtain:

$$(1 - I_r \cdot \Pi_r) \cdot \dot{\gamma}_r = \dot{I}_r \cdot \Pi_r \cdot \Gamma + I_r \cdot \dot{\Pi}_r \cdot \Gamma + I_r \cdot \Pi_r \cdot \dot{I}_r. \quad (2.30)$$

Finally, we multiply Eq. (2.30) by  $(1 - I_r \cdot \Pi_r)^{-1}$  from left to isolate  $\dot{\gamma}_r$ .

$$\dot{\gamma}_r = \Gamma \cdot \dot{\Pi}_r \cdot \Gamma + \dot{I}_r \cdot \Pi_r \cdot \Gamma + \Gamma \cdot \Pi_r \cdot \dot{I}_r \cdot \Pi_r + \Gamma \cdot \Pi_r \cdot \dot{I}_r. \quad (2.31)$$

This derivation can be obtained by using the identities provided in Chapter 2.2.3. For a more detailed derivation, we refer the reader to Ref. [20]. So far, the only approximation we have used is the parquet approximation and apart from that, the Eq. (2.31) is an exact relation.

## 2.2. Multiloop Pseudofermion Functional Renormalization Group

---

We categorize contributions to the Eq. (2.31) by the number of fermionic loops that connect two vertices,  $\Pi$  present in each term.

$$\dot{\gamma}_r = \sum_{n=1} \dot{\gamma}_r^{(n)}. \quad (2.32)$$

The first term in Eq. (2.31) corresponds to the first loop order, as it is the only term with one fermionic loop [24] :

$$\dot{\gamma}_r^{(1)} \equiv \Gamma \cdot \dot{\Pi}_r \cdot \Gamma. \quad (2.33)$$

The rest of the loop orders can be derived iteratively from each other. For the second-loop contribution in channel  $r$ , we need to consider the derivative of the irreducible vertex in channel  $r$ , which is related to other channels as

$$\dot{I}_r = \sum_{r' \neq r} \dot{\gamma}_{r'}. \quad (2.34)$$

For the second loop order, the second and last term in Eq. (2.31) will contribute, as they are the only ones with two fermionic loops. Thus, the second loop contribution is

$$\dot{\gamma}_r^{(2)} = \sum_{r' \neq r} \dot{\gamma}_{r'}^{(1)} \cdot \Pi_r \cdot \Gamma + \sum_{r' \neq r} \Gamma \cdot \Pi_r \cdot \dot{\gamma}_{r'}^{(1)}. \quad (2.35)$$

Similarly, this procedure can be extended to the third and higher loop orders. The formula for an arbitrary loop order  $\ell$  that is  $\ell \geq 3$ , is given as [24]:

$$\dot{\gamma}_r^{(\ell)} = \sum_{r' \neq r} \left( \dot{\gamma}_{r'}^{(\ell-1)} \cdot \Pi_r \cdot \Gamma + \Gamma \cdot \Pi_r \cdot \dot{\gamma}_{r'}^{(\ell-2)} \cdot \Pi_r \cdot \Gamma + \Gamma \cdot \Pi_r \cdot \dot{\gamma}_{r'}^{(\ell-1)} \right). \quad (2.36)$$

Since this iteration can be continued up to infinite order, at some stage the sum in Eq. (2.32) needs to be truncated to maintain the numerical feasibility of the calculations [24]. In this thesis, we will only utilize the first two loop orders.

Moreover, each term contains a derivative of a bubble  $\Pi$  which is composed of two full propagators,

$$\dot{\Pi}_r = \dot{G}G + G\dot{G}, \quad (2.37)$$

which requires us to compute the derivative of the propagator. To compute the derivative of the propagator, we can make use of the Dyson equation, as given in Eq. (2.16):

$$\begin{aligned} \dot{G} &= \partial_\Lambda (G_0^{-1} - \Sigma)^{-1} = (G_0^{-1} - \Sigma)(-\partial_\Lambda G_0^{-1} + \dot{\Sigma})(G_0^{-1} - \Sigma) \\ &= S + G\dot{\Sigma}G, \end{aligned} \quad (2.38)$$

## 2. Theoretical Background

---

where  $S$  is the single-scale propagator defined as:

$$S = -G[\partial_\Lambda G_0^{-1}]G. \quad (2.39)$$

In the literature inclusion of the  $\dot{\Sigma}$  term corresponds to the Katanin truncation [37]. The importance of this improved truncation scheme is illustrated in Ref. [16] and has become a common practice in the pffRG community [1, 2, 10, 16, 18, 19, 38].

In order to fully evaluate the vertex flow, we also need to compute  $\dot{\Sigma}$ , as Eq. (2.38) contains the derivative of the self-energy. This can be accomplished by taking derivative of the SDE described in Eq. (2.21). Given the lengthy nature of the self-energy flow derivation, we will not re-derive the flow equation here. Instead, we simply state the result and refer the reader to Ref. [20] for further details.

$$\dot{\Sigma} = \underbrace{[-\Gamma \cdot S]}_{\dot{\Sigma}_{std}} + \underbrace{[\dot{\gamma}_t^{(C)} \cdot G]}_{\dot{\Sigma}_{\bar{t}}} + \underbrace{[-\Gamma \cdot (G \cdot \dot{\Sigma}_{\bar{t}} \cdot G)]}_{\dot{\Sigma}_t}. \quad (2.40)$$

The first term is the standard self-energy flow used in the literature. The term  $\dot{\gamma}_t^{(C)}$  is the third term in Eq. (2.31) and is expressed as  $\dot{\gamma}_t^{(C)} = \Gamma \cdot \Pi_t \cdot \dot{I}_t \cdot \Pi_t \cdot \Gamma$ . The last two objects in Eq. (2.40) are the corrections to the self energy coming from the multiloop.

The vertex flow equations, along with the self-energy flow equation, form a differential equation that can be solved at a given  $\Lambda$  value using the initial conditions at  $\Lambda_i \rightarrow \infty$  where  $G_0^{\Lambda_i} \rightarrow 0$  as a result of Eq. (2.22).

$$\Sigma|_{\Lambda_i} = 0, \quad (2.41)$$

$$\Gamma|_{\Lambda_i} = \Gamma_0. \quad (2.42)$$

However, instead of using the initial condition for  $\Lambda \rightarrow \infty$ , we use the solution of the parquet equations at an initial  $\Lambda_i$  value. Throughout this thesis, we initialize the fRG flow at  $\Lambda_i = 2.5J$  by solving the parquet equations for  $\Sigma$ ,  $\Gamma$  and using the obtained results as the initial condition [5, 24]. As discussed in Chapter 2.2.3, the parquet equations can be solved iteratively. Technical details of solving parquet equations within our code can be found in Refs. [5, 24]. To solve the differential equation, we utilize an adaptive fifth-order Runge-Kutta algorithm that was implemented by Marc Ritter and Julian Thönni. For details we refer reader to [5, 24, 39].

For most parts of this thesis, we use the one-loop approximation, which corresponds to truncating the sum in Eq. (2.32) at the first order. Consequently, only diagrams with one fermionic loop contribute to the flow equations. For the self-energy flow given in Eq. (2.40), only the first term  $\dot{\Sigma}_{std}$  contributes. This approximation corresponds to the one-loop approximation with Katanin truncation commonly found in the pffRG literature [1, 2, 16, 18, 38].

## Implementation

### 3.1 Symmetries of the Pseudofermion Action

The 2n-point Green's function is defined as a time-ordered, thermal expectation value of  $n$  Grassmann fields as

$$G^{(2n)}(1' \dots n'; 1 \dots n) = \langle \psi_1 \dots \psi_n \bar{\psi}_n \dots \bar{\psi}_1 \rangle, \quad (3.1)$$

where the correlator in path integral formalism is given as

$$\langle \psi_1 \dots \bar{\psi}_n \rangle = \frac{1}{Z} \int D[\psi, \bar{\psi}] \psi_1 \psi_2 \dots \bar{\psi}_{n-1} \bar{\psi}_n e^{-S[\psi, \bar{\psi}]}. \quad (3.2)$$

The  $Z$  in Eq. (3.2) is the partition function for normalization.

A linear transformation  $\mathcal{F}$  on Grassmann fields defined as

$$\psi \rightarrow \psi' = \mathcal{F}\psi, \quad \bar{\psi} \rightarrow \bar{\psi}' = \bar{\psi}\mathcal{F}^\dagger. \quad (3.3)$$

A linear transformation,  $\mathcal{F}$ , is a symmetry operation if the action is invariant under that transformation.

$$S[\psi', \bar{\psi}'] = S[\psi, \bar{\psi}]. \quad (3.4)$$

The correlator (3.2) under symmetry transformation is also invariant

$$\begin{aligned} \langle \psi'_1 \psi'_2 \dots \bar{\psi}'_{n-1} \bar{\psi}'_n \rangle &= \frac{1}{Z} \int D[\psi', \bar{\psi}'] \psi'_1 \psi'_2 \dots \bar{\psi}'_{n-1} \bar{\psi}'_n e^{-S[\psi', \bar{\psi}']} \\ &= \frac{1}{Z} \int D[\psi, \bar{\psi}] \psi_1 \psi_2 \dots \bar{\psi}_{n-1} \bar{\psi}_n e^{-S[\psi', \bar{\psi}']} \\ &= \frac{1}{Z} \int D[\psi, \bar{\psi}] \psi_1 \psi_2 \dots \bar{\psi}_{n-1} \bar{\psi}_n e^{-S[\psi, \bar{\psi}]} = \langle \psi_1 \psi_2 \dots \bar{\psi}_{n-1} \bar{\psi}_n \rangle. \end{aligned}$$

In the second step, we relabeled the Grassmann fields, and in the last step, we used the fact that the action is invariant under symmetry operations. Hence,

### 3. Implementation

---

the correlators are also invariant under symmetry transformations. This is known as the Ward-Takahashi identity [40].

By analyzing the symmetries of the pseudofermion Hamiltonian, we can determine which components of correlators can be related through symmetry transformations. This, in turn, allows us to reduce the number of independent variables required for solving the flow equations. Implementation of this parametrization in our code was accomplished by Marc Ritter [24] and Julian Thönni [4].

In the next two sections we re-trace the study of Buessen et al. [41, 42] on the symmetries of the pseudofermion Hamiltonian. First, we investigate the local SU(2) gauge redundancy introduced by pseudofermion construction, then we state the results from Refs. [41, 42] compactly in a table with all the symmetries.

#### 3.1.1 Local SU(2) Gauge Redundancy

The mapping of spin operators to fermionic operators introduces an external SU(2) symmetry that is not present in the original Hamiltonian. To make the SU(2) symmetry more visible, we re-write the spin operator as a trace over matrices [41–43].

$$S_i^\mu = \frac{1}{4} \text{tr}(F_i^\dagger \sigma^\mu F_i), \quad (3.5)$$

with  $F_i$  containing the pseudofermion operators

$$F_i = \begin{pmatrix} \psi_{i,\uparrow} & \psi_{i,\downarrow}^\dagger \\ \psi_{i,\downarrow} & -\psi_{i,\uparrow}^\dagger \end{pmatrix}. \quad (3.6)$$

The local linear transformation is defined as the right matrix multiplication and the global linear transformation is defined as the left matrix multiplication,

$$F_i \rightarrow F_i g_{\text{local}}, \quad F \rightarrow g_{\text{global}} F_i. \quad (3.7)$$

For  $g_{\text{local}}$  transformation that satisfies

$$g_{\text{local}} g_{\text{local}}^\dagger = 1, \quad (3.8)$$

the spin operator,  $S^\mu$ , is left invariant due to the cyclic property of the trace. Thus, the pseudofermion Hamiltonian is invariant under local SU(2) transformations. This is not the case for  $g_{\text{global}}$ , it acts as a rotation in spin space

$$\sigma^\mu \rightarrow \sigma^{\mu'} = g_{\text{global}} \sigma^\mu g_{\text{global}}. \quad (3.9)$$

As explained in Refs. [41, 42] instead of dealing with SU(2) directly, we look at the gauge redundancy in two parts; the local U(1) symmetry and the local-particle hole symmetry. The local U(1) symmetry allows us to parameterize correlators in real space, while the particle-hole symmetry allows us to parameterize in frequency space.

**Local U(1) gauge redundancy**

First, we investigate the local U(1) symmetry of the Hamiltonian, which is a subgroup of SU(2). The U(1) symmetry operation is defined as

$$\psi_{i\alpha} \rightarrow e^{-i\phi_i} \psi_{i\alpha}, \quad \bar{\psi}_{i,\alpha} \rightarrow e^{i\phi_i} \bar{\psi}_{i\alpha}. \quad (3.10)$$

where  $\phi_i$  is a complex number.

Spin operators in pseudofermion representation come with a pair of fermionic creation and annihilation operators. Since the phases have equal but opposite signs the complex phases cancel each other out, leaving  $S_i^\mu$  invariant. Thus, the pseudofermion Hamiltonian is invariant under local U(1) transformations, meaning, the correlators of the theory should also be invariant under U(1) transformation. For the two-point correlator this means;

$$\langle \psi_{i_1 \alpha_1}^\dagger \psi_{i_1 \alpha_1} \rangle \stackrel{!}{=} e^{i\phi_{i_1} - i\phi_{i_1}} \langle \psi_{i_1 \alpha_1}^\dagger \psi_{i_1 \alpha_1} \rangle. \quad (3.11)$$

The condition (3.11) is satisfied when  $i_1 = i_1'$ . This means that the two-particle Green's function should be local in real space [41, 42].

$$G(1'; 1) = G(1'; 1) \delta_{i_1, i_1'}. \quad (3.12)$$

Similarly, the four-point correlator is invariant under such transformation.

$$\langle \psi_{i_1 \alpha_1}^\dagger \psi_{i_2 \alpha_2}^\dagger \psi_{i_2 \alpha_2} \psi_{i_1 \alpha_1} \rangle \stackrel{!}{=} e^{i\phi_{i_1} + i\phi_{i_2} - i\phi_{i_1} - i\phi_{i_2}} \langle \psi_{i_1 \alpha_1}^\dagger \psi_{i_1 \alpha_1} \rangle, \quad (3.13)$$

which is fulfilled when  $\phi_{i_1} + \phi_{i_2} - \phi_{i_1}' - \phi_{i_2}' = 0$ . This imposes a bi-local condition on the four-point correlator [41, 42].

$$G(1', 2'; 1, 2) = G(1', 2'; 1, 2) \delta_{i_1 i_1'} \delta_{i_2 i_2'} - G(2', 1'; 1, 2) \delta_{i_2 i_1'} \delta_{i_1 i_2'}. \quad (3.14)$$

**Local particle-hole gauge redundancy**

The local particle-hole transformation acts on fermionic operators as,

$$\psi_{i\alpha} \rightarrow \alpha \psi_{i\bar{\alpha}}^\dagger, \quad \psi_{i\alpha}^\dagger \rightarrow \alpha \psi_{i\bar{\alpha}}. \quad (3.15)$$

where  $\alpha = +1(-1)$  for the spin index  $\alpha = \uparrow(\downarrow)$  and  $\bar{\alpha}$  is the flipped spin index. Under this transformation, the two-point correlator transforms as

$$\langle \psi_{i_1 \omega_1 \alpha_1}^\dagger \psi_{i_1 \omega_1 \alpha_1} \rangle \stackrel{!}{=} -\alpha' \alpha \langle \psi_{i_1 - \omega_1 \bar{\alpha}_1}^\dagger \psi_{i_1 - \omega_1 \bar{\alpha}_1} \rangle, \quad (3.16)$$

meaning the 2-point Green's function transforms as

$$G(1'; 1) = -\alpha' \alpha G(i_1 - \omega_1 \bar{\alpha}_1; i_1' - \omega_1 \bar{\alpha}_1'). \quad (3.17)$$

The local particle-hole transformation can be applied to any local pair of creation-annihilation operators. To make it more compact we combine this with the local U(1) symmetry to obtain [41, 42]

$$G(1', 2'; 1, 2) \delta_{i_1 i_1'} \delta_{i_2 i_2'} = -\alpha_1' \alpha_1 G(i_1 - \omega_1 \bar{\alpha}_1, i_2 \omega_2 \alpha_2'; i_1 - \omega_1 \bar{\alpha}_1', i_2 \omega_2 \alpha_2) \quad (3.18a)$$

$$= -\alpha_2' \alpha_2 G(i_1 \omega_1 \alpha_1', i_2 - \omega_2 \bar{\alpha}_2; i_1 \omega_1 \alpha_1, i_2 - \omega_2 \bar{\alpha}_2') \quad (3.18b)$$

### 3. Implementation

symmetry	$G(1'; 1)$	$G(1', 2'; 1, 2)\delta_{i_1' i_1} \delta_{i_2' i_2}$
H	$G(-1; -1')^*$	$G(-1, -2; -1', -2')^*$
TR	$\alpha_1 \alpha_1' G(-1', 1)^*$	$\alpha_1 \alpha_1' \alpha_2 \alpha_2' G(-\bar{1}, -\bar{2}; \bar{1}, \bar{2})^*$
EC	$G(1'; 1)\delta_{\omega_1 \omega_1'}$	$G(1', 2'; 1, 2)\delta_{i_1' i_1} \delta_{i_2' i_2} \delta_{\omega_1 + \omega_2, \omega_1' + \omega_2'}$
U(1)	$G(1'; 1)\delta_{i_1, i_1'}$	$G(1', 2'; 1, 2)$
PH1	$-\alpha_1' \alpha G(-\bar{1}; -\bar{1}')$	$-\alpha_1' \alpha_1 G(-\bar{1}, 2'; -\bar{1}', 2)$
PH2	$-\alpha_1' \alpha G(-\bar{1}; -\bar{1}')$	$-\alpha_2' \alpha_2 G(1', -\bar{2}; 1, -\bar{2}')$

Table 3.1: Symmetries of pseudofermion Hamiltonian and constraints on correlation functions according to Refs. [41, 42]

#### 3.1.2 Physical Symmetries

Physical symmetries are the second type of symmetry in the pseudofermion Hamiltonian. These symmetries are model specific, present in the original Hamiltonian and are not introduced by the pseudofermion representation.

To keep this section brief, we introduce a compact notation as in Ref. [24]

$$1 = (i_1, \omega_1, \alpha_1), \quad (3.19)$$

$$-1 = (i_1, -\omega_1, \alpha_1), \quad (3.20)$$

$$\bar{1} = (i_1, \omega_1, \bar{\alpha}_1). \quad (3.21)$$

Physical symmetries discussed in Refs. [41, 42] namely are;

**Hermitian symmetry (H)** is fulfilled as the Hamiltonian of our model is Hermitian<sup>1</sup>. It acts on the fermionic operators as  $\psi_{i\alpha} \rightarrow \psi_{i\alpha}^\dagger$ .

**Time reversal symmetry (TR)** is fulfilled by the pseudofermion Hamiltonian as spin operators come in pairs<sup>2</sup>, it acts on the fermionic operators as  $\psi_{i\alpha} \rightarrow e^{i\pi \frac{\alpha}{2}} \psi_{i\bar{\alpha}}$  [41, 42].

**Energy conservation (EC)** is fulfilled by time translation symmetry.

#### 3.1.3 Parameterization of Correlators

Using the symmetries derived in the previous subsection we can finally parameterize the 2 and 4-point correlation functions.

The 2-point correlation function can be parameterized as [41, 42]

$$G(1'; 1) = \delta_{i_1', i_1} \delta_{\omega_1', \omega_1} G_{i_1}(\omega) \delta_{\alpha_1', \alpha_1}. \quad (3.22)$$

The first two Dirac delta functions in Eq.(3.22) come from the combination of H and EC symmetries. And the combination of the rest of the symmetries suggests that the two-point correlator is diagonal in spin space [41, 42].

<sup>1</sup>Hermitian symmetry is broken for the Popov-Fedetov projection scheme as the Hamiltonian is no longer hermitian [33]

<sup>2</sup>Time reversal symmetry is broken for the Popov-Fedetov projection scheme due to the chemical potential term [33]

### 3.1. Symmetries of the Pseudofermion Action

---

Also, due to the Hermitian symmetry, the two-point correlator is purely imaginary and anti-symmetric

$$G(\omega) = -G(-\omega). \quad (3.23)$$

The symmetries of the two-point correlator also apply to the self-energy due to the Dyson equation,

$$G(\omega) = \frac{1}{i\omega - \Sigma(\omega)}. \quad (3.24)$$

Thus, the self-energy also has the same form as the two-particle correlator

$$\Sigma(1'; 1) = \delta_{i'_1, i_1} \delta_{\omega'_1, \omega_1} \Sigma_{i_1}(\omega) \delta_{\alpha'_1 \alpha_1}, \quad \Sigma(\omega) = -\Sigma(-\omega). \quad (3.25)$$

The vertex function is obtained from the 4-point connected correlation function as

$$G_{\text{connected}}^{(4)}(1', 2'; 1, 2) = \sum_{3'4'34} G(1'; 3') G(2'; 4') \Gamma(3', 4'; 3, 4) G(3; 1) G(4; 2). \quad (3.26)$$

From Eq. (3.22) we know that the two-point correlators can be written diagonally in real space, frequency-space, and spin-space. Thus, the vertex has to fulfill the same constraints as the 4-point correlator, and we can parameterize the  $\Gamma(1', 2'; 1, 2)$  as

$$\begin{aligned} \Gamma(1', 2'; 1, 2) = \sum_{\mu, \nu=0}^3 \left[ \Gamma_{i'_1 i'_2}^{\tilde{\mu\nu}}(\omega'_1, \omega'_2; \omega_1, \omega_2) \sigma_{\alpha'_1 \alpha_1}^{\mu} \sigma_{\alpha'_2 \alpha_2}^{\nu} \delta_{i'_1 i_1} \delta_{i'_2 i_2} \right. \\ \left. - \Gamma_{i_1 i_2}^{(\mu\nu)}(\omega'_1, \omega'_2; \omega_2, \omega_1) \sigma_{\alpha'_1 \alpha_2}^{\mu} \sigma_{\alpha'_2 \alpha_1}^{\nu} \delta_{i'_1 i_2} \delta_{i'_2 i_1} \right] \delta_{\omega'_1 + \omega'_2, \omega_1 + \omega_2}, \end{aligned} \quad (3.27)$$

where  $\sigma^{\mu}$  is the Pauli matrix with  $\sigma^0$  being the identity matrix.

In this thesis, we investigate the isotropic Heisenberg model with SU(2) symmetry, where the interaction  $J$  is diagonal with respect to the  $\mu, \nu$  indices,

$$J_{ij}^{\mu\nu} = \delta^{\mu\nu} J_{ij}^{\mu}, \quad (3.28)$$

and equal in all three directions

$$J^1 = J^2 = J^3 = J. \quad (3.29)$$

As a result of Eq. (3.28), the vertex has a diagonal structure that can be expressed as  $\Gamma^{\mu\nu} = \delta^{\mu\nu} \Gamma^{\mu}$ . And with Eq. (3.29), we can decompose the vertex object into two distinct vertex types: the spin interaction (s) vertex,  $\Gamma^s = \Gamma^1 = \Gamma^2 = \Gamma^3$ , and the density interaction (d) vertex,  $\Gamma^0 = \Gamma^d$  [16, 18].

### 3. Implementation

---

Using the crossing symmetries, we can also relate the  $\Gamma^{\sim}$  to  $\Gamma^{)\leftarrow}$  as discussed in Ref. [5]

$$\gamma_{a;i_1 i_2}^{\sim}(1', 2'; 1, 2) = \gamma_{t;i_1 i_2}^{)\leftarrow}(2', 1'; 1, 2), \quad (3.30a)$$

$$\gamma_{t;i_1 i_2}^{\sim}(1', 2'; 1, 2) = \gamma_{a;i_1 i_2}^{)\leftarrow}(2', 1'; 1, 2), \quad (3.30b)$$

$$\gamma_{p;i_1, i_2}^{\sim}(1', 2'; 1, 2) = \gamma_{p;i_1 i_2}^{)\leftarrow}(2', 1'; 1, 2), \quad (3.30c)$$

$$\Gamma_{i_1 i_2}^{\sim}(1', 2'; 1, 2) = \Gamma_{i_1 i_2}^{)\leftarrow}(2', 1'; 1, 2). \quad (3.30d)$$

#### 3.1.4 Lattice Symmetries

So far, we have mentioned symmetries involving frequency and spin dependency of the vertices. In this section, we will examine the lattice symmetries inherent to the model under consideration.

Throughout this thesis, we examine lattice structures that exhibit translational invariance, meaning any lattice site can be mapped to another by employing translation operators,  $\hat{T}_j$ , which utilize primitive lattice vectors to map one site to another using the translational invariance. These operators act on the indices of the vertices as follows [18, 24]:

$$\hat{T}_j \Gamma_{i_1, i_2} = \Gamma_{i_1 - j, i_2 - j}. \quad (3.31)$$

By employing the translation operators, every  $i_1, i_2$  pair can be mapped into  $0, i_2'$  pair

$$\Gamma_{i_1, i_2} \rightarrow \hat{T}_{i_1} \Gamma_{i_1, i_2} = \Gamma_{0, i_2'}. \quad (3.32)$$

This enables us to store vertices with the first index fixed to  $i_1 = 0$  [18, 24].

Moreover, by introducing symmetry operators,  $\hat{Q}$ , that map the lattice structure onto itself using rotation and reflection operations consistent with lattice symmetries, we can further decrease the number of independent vertices.

$$\Gamma_{i_1, i_2} \rightarrow \hat{Q} \Gamma_{i_1, i_2} = \Gamma_{i_1', i_2'} = \Gamma_{i_1, i_2}. \quad (3.33)$$

As a result, we can discard the set of vertices that can be related through symmetry operations, retaining only one copy for each vertex set in memory.

Throughout the thesis, we will utilize two distinct boundary conditions. For the long-range interactions on the triangular and square lattices, we assume an infinite lattice, whereas in the second part, we employ periodic boundary conditions in one direction and keep an infinite lattice in the other direction.

#### Long-range interactions on the triangular and the square lattice

In order to investigate long-range interactions, we employ an infinite lattice. However, due to the finite resources of computers, it is necessary to truncate the lattice at a certain distance. We implement this truncation by introducing

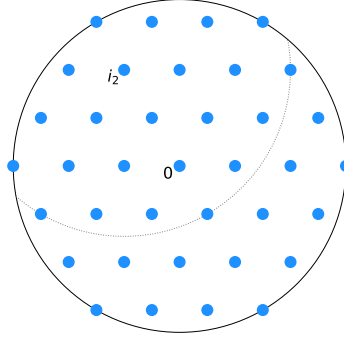


Figure 3.1: The triangular lattice centered around the lattice site 0 and with  $R_{\max} = 3$ . The region enclosed by the dotted line highlights vertices featuring pairings that involve the  $i_2$  index.

a cutoff distance,  $R_{\max}$ , and discarding every vertex with an index  $i_2$  that satisfies  $|\mathbf{r}_0 - \mathbf{r}_{i_2}| > R_{\max}$  [18, 24]. This procedure is illustrated in Fig. 3.1.

As previously discussed, by using lattice symmetries, we can reduce the number of vertices stored in the memory. For the Heisenberg model without the interactions, the full symmetry of the lattice structure enables us to decrease the number of stored vertices. However, once the dipolar interactions are introduced the rotational symmetries are broken, making our calculations more computationally demanding.

The dipolar interaction is defined as [1, 2]

$$J_{i_1 i_2} = J_0 \frac{(1 - 3(\hat{\mathbf{r}}_{i_1 i_2} \cdot \hat{\mathbf{d}})^2)}{r_{i_1 i_2}^3}, \quad (3.34)$$

where  $\mathbf{r}_{i_1 i_2} = \mathbf{r}_{i_1} - \mathbf{r}_{i_2}$  represents the displacement vector between lattice sites  $i_1$  and  $i_2$ , and  $\mathbf{d}$  represents the alignment of the dipoles, in spherical coordinates as  $\hat{\mathbf{d}} = (\sin \theta \cos \phi, \sin \theta \sin \phi, \cos \theta)$ . Eq. (3.34) breaks the lattice symmetries as interaction is direction dependant, yet the inversion symmetry is still preserved. This invariance can be observed by noting that the Eq. (3.34) is invariant for  $\mathbf{r}_{i_1 i_2} \rightarrow -\mathbf{r}_{i_1 i_2}$ .

### Periodic boundary condition for infinite chain

In the second part of the thesis, we will study the antiferromagnetic Heisenberg model on a one-dimensional infinite chain.

We implement the cutoff procedure described earlier for the infinite portion of the lattice. We select a cutoff distance  $R_{max}$  and discard vertices that lie out of this chosen region.

However, we require periodic boundary conditions in the other direction to couple these chains and position them on a cylinder. In this direction, when we encounter a vertex  $\Gamma_{i_1 i_2}$  such that  $|\mathbf{r}_{i_1} - \mathbf{r}_{i_2}| > R_{\text{period}}$  instead of discarding it, we relate to another vertex by leveraging the periodicity of the lattice [18]. This procedure is illustrated in Fig. 3.3.

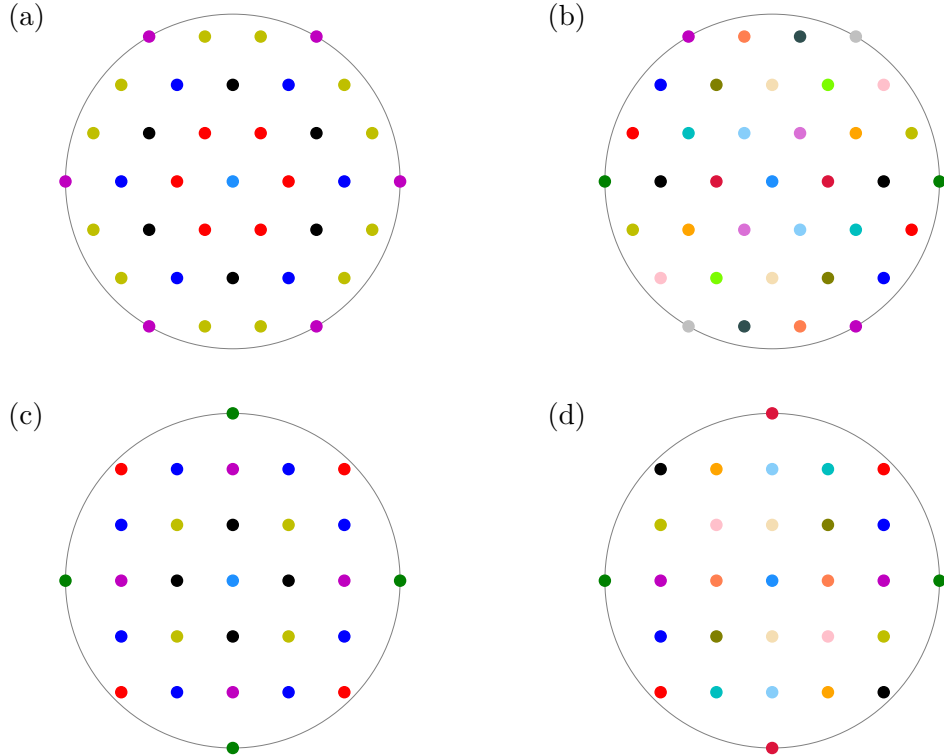


Figure 3.2: Triangular (first row) and square lattice (second row) with  $R_{\max} = 3$ . Sites with the same color represent vertices that are obtainable from each other through symmetry operations. We keep one vertex of each color in memory. The first column is for isotropic interactions when the model exhibits full symmetry, and the second column illustrates model with only inversion symmetry.

### 3.1.5 Asymptotic Classes

In this chapter, we discuss the efficient parameterization of two-particle reducible channels into the so-called asymptotic classes, as introduced by Wentzell et al. in Ref. [44]. The implementation of these classes to our method has been carried out by Julian Thönniß and Marc Ritter in the past years, and we direct the reader interested in the details of the implementation to Refs. [4, 5, 24]. Since this implementation represents one of the key distinctions between our work and existing literature, it is valuable to provide a concise overview.

As discussed in Sec. 2.2.3, the parquet decomposition of a vertex separates contributions into a totally irreducible channel and three two-particle reducible channels

$$\Gamma = R + \sum_r \gamma_r. \quad (3.35)$$

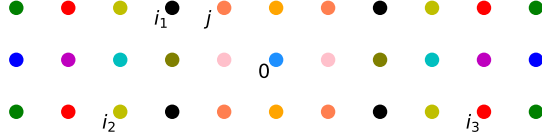


Figure 3.3: Three infinite coupled chains on a cylinder with  $R_{\max} = 5$  and  $R_{\text{period}} = 1$ . Coloring is applied using lattice symmetries.  $\Gamma_{i_1 i_3}$  and  $\Gamma_{i_2 i_3}$  are two example vertices that are discarded, but  $\Gamma_{i_1 i_2}$  is related to  $\Gamma_{0j}$  using periodic boundary conditions.

Similar to a vertex, a two-particle channel,  $\gamma_r$ , also possesses four frequency arguments. However, only three independent frequency parameters exist due to the energy conservation,  $\omega_1 + \omega_2 = \omega'_1 + \omega'_2$ . Throughout this thesis, we compare our results with existing literature [1, 2, 10, 18] where typically three bosonic frequencies are used to parameterize the vertices. However, in our work, we parameterize the two-particle reducible channel in terms of two fermionic frequencies  $(\nu, \nu')$  and one bosonic frequency  $(\Omega)$ . Furthermore, we separate the two-particle reducible vertex into so-called asymptotic classes,  $\mathcal{K}$ , which contain diagrams that are classified based on their dependence on these two fermionic frequencies [44]

$$\gamma_r = \mathcal{K}_{1r}^{\Omega} + \mathcal{K}_{2r}^{\Omega, \nu} + \mathcal{K}_{2'r}^{\Omega, \nu'} + \mathcal{K}_{3r}^{\Omega, \nu, \nu'}. \quad (3.36)$$

The  $\mathcal{K}_{1r}^{\Omega}$  class includes diagrams where each pair of external legs is connected to a bare vertex. Since the frequency is conserved at each vertex, the incoming and outgoing frequencies counterbalance each other at these bare vertices, causing diagrams in this set to depend only on the bosonic transfer frequency  $\Omega$ .

The  $\mathcal{K}_{2r}^{\Omega, \nu}$  class contains diagrams that have  $\nu'$  frequency carrying legs that are connected to the same bare vertex, removing the  $\nu'$  dependency. Similarly, the  $\mathcal{K}_{2'r}^{\Omega, \nu'}$  class contains diagrams that have  $\nu$  frequency carrying legs connected to the same bare vertex, removing the  $\nu$  dependence.

The  $\mathcal{K}_{3r}^{\Omega, \nu, \nu'}$  class consists of diagrams that have all external legs connected to distinct bare vertices. Consequently, these diagrams retain all three frequency dependencies.

The main idea behind this decomposition is that diagrams containing bubbles carrying external frequencies decay faster compared to those without, as Green's functions are inversely proportional to their frequency dependence. This concept is illustrated in Fig. 3.4. For the first bubble, we have

$$\lim_{\nu \rightarrow \infty} \Pi(\Omega, \nu) = \lim_{\nu \rightarrow \infty} G(\Omega)G(\nu) \rightarrow 0, \quad (3.37)$$

Thus, we can separate the contribution of asymptotic classes to the two

### 3. Implementation

---

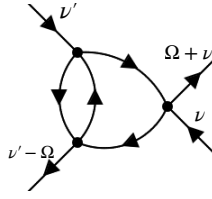


Figure 3.4: The "eye" diagram in a channel given in Ref.[24]. This types of diagrams are included in  $\mathcal{K}_{2'a}^{\Omega\nu}$  class. The  $\nu$  dependence is canceled at the second vertex but  $\nu'$  dependence is still remains.

particle-reducible vertices at the high-frequency limit as

$$\lim_{\nu' \rightarrow \infty} \gamma_r = \mathcal{K}_{1r}^{\Omega} + \mathcal{K}_{2r}^{\Omega, \nu}, \quad (3.38a)$$

$$\lim_{\nu \rightarrow \infty} \gamma_r = \mathcal{K}_{1r}^{\Omega} + \mathcal{K}_{2r}^{\Omega, \nu'}, \quad (3.38b)$$

$$\lim_{\nu' \rightarrow \infty} \lim_{\nu \rightarrow \infty} \gamma_r = \mathcal{K}_{1r}^{\Omega}. \quad (3.38c)$$

Because we work at  $T = 0$  the frequency domain is continuous, and we must sample this domain by choosing an appropriate number of frequency points. With this decomposition, we can better resolve vertices in frequency space by choosing a different number of frequency points for each channel to optimize our vertex resolution.

Additionally, the symmetries discussed in the previous chapter are applicable to the asymptotic classes, reducing the numerical cost of our calculations. As the implementation of these symmetries was completed by our other group members Ritter and Thönniß, we direct readers interested in the specifics to Refs. [4, 5, 24] for further details.

#### Frequency Grid

In order to resolve vertices properly an adaptive frequency grid consisting of a linear and an algebraic part implemented by Julian Thönniß and Marc Ritter [5, 24, 39]. Here we give a brief overview of the frequency grid, as it is one of the key differences between our work and the pffRG literature.

The linear portion of the frequency grid covers the lower frequency regime,  $\omega \in [0, \omega_{\text{linear}}]$ , where the vertex functions have sharper features, while the algebraic part of the grid covers the higher frequency regime,  $\omega \in (\omega_{\text{linear}}, \omega_{\text{high}}]$ , where the vertex has a structure with fewer characteristics [24, 39]. This separation of the frequency grid allows us to better resolve the feature of the vertex functions and choose a different grid for each of the asymptotic classes. We obtain the negative region of the grid by taking reflection symmetry with respect to the origin. Additionally, an adaptive algorithm is utilized to adjust the spacing of the frequency grid to accommodate the sharp features of the vertex functions that might change after each  $\Lambda$  step. Details of this algorithm can be found in Refs. [24, 39].

## 3.2 Spin Susceptibility

Up until now, we have only looked at the vertices and efficient ways to calculate their flow. However, the vertex object alone is not an easy object to interpret. Instead, we now introduce the spin susceptibility which is a more comprehensible concept that can be directly accessed via experimental methods.

The spin susceptibility,  $\chi(\Omega)$ , is the main physical observable that can be computed from solving the flow equations. While the flow parameter  $\Lambda$  flows from large cutoff limit  $\Lambda_i$  to small cutoff limit  $\Lambda_0$ , we calculate the spin susceptibility at each  $\Lambda$  step.

The spin susceptibility is defined as [16]

$$\chi_{ij}^{\mu\nu}(\Omega) = \int_0^\beta d\tau e^{i\tau\Omega} \langle T_\tau S_i^\mu(\tau) S_j^\nu(0) \rangle, \quad (3.39)$$

$i, j$  are the lattice sites and  $\mu, \nu = x, y, z$ . As we are working in  $T = 0$  regime the upper bound of the integral will be  $\beta \rightarrow \infty$ .

Due to the  $SU(2)$  symmetry of the Heisenberg Hamiltonian and the Ward-Takahashi identity, the correlation functions are also invariant under  $SU(2)$  symmetry operations. This implies that the spin susceptibility must be diagonal in  $\mu, \nu$  indices.

Thus, we only need to calculate

$$\chi_{ij}^{\mu\mu}(\Omega) = \int_0^\beta d\tau e^{i\tau\Omega} \langle T_\tau S_i^\mu(\tau) S_j^\mu(0) \rangle. \quad (3.40)$$

And in pseudofermion representation, Eq. (3.40) equals to:

$$\chi_{ij}^{\mu\mu}(\Omega) = \int_0^\beta d\tau e^{i\tau\Omega} \sum_{\alpha\alpha'\gamma\gamma'} \frac{1}{4} \sigma_{\alpha\alpha'}^\mu \sigma_{\gamma\gamma'}^\mu \langle T_\tau \psi_{i\alpha}^\dagger(\tau) \psi_{i\alpha'}(\tau) \psi_{j\gamma}^\dagger(0) \psi_{j\gamma'}(0) \rangle. \quad (3.41)$$

Now applying all the possible Wick contractions and using the time translational invariance [4, 24], we obtain:

$$\begin{aligned} \chi_{ij}^{\mu\mu}(\Omega) = \int_0^\beta d\tau e^{i\tau\Omega} \sum_{\alpha\alpha'\gamma\gamma'} \frac{1}{4} \sigma_{\alpha\alpha'}^\mu \sigma_{\gamma\gamma'}^\mu & \left( -\delta_{ij} \delta_{\alpha\gamma'} \delta_{\alpha'\gamma} G(\tau) G(-\tau) + \delta_{\alpha\alpha'} \delta_{\gamma\gamma'} G(0)^2 \right. \\ & \left. + \int_0^\beta d\tau' G(\tau - \tau') G(\tau' - \tau) G(\tau') G(-\tau') \Gamma(1', 2'; 1, 2) \right). \end{aligned} \quad (3.42)$$

Here the  $1 = \{\tau, i, \alpha\}$  represents all the indices and similarly  $1' = \{\tau, i, \alpha'\}$ ,  $2 = \{0, j, \gamma\}$ , and  $2' = \{0, j, \gamma'\}$ . Now, we will investigate each term separately.

### 3. Implementation

---

The first term:

$$\begin{aligned} & \sum_{\omega_1 \omega_2} \int_0^\beta d\tau e^{i\tau\Omega} e^{i\omega_1\tau} e^{-i\omega_2\tau} G(\omega_1) G(\omega_2) \frac{-\delta_{ij}}{4} \sum_{\alpha\alpha'} \sigma_{\alpha\alpha'}^\mu \sigma_{\alpha'\alpha}^\mu \\ &= \frac{-\delta_{ij}}{4\beta} \sum_{\omega_1} G(\omega_1) G(\omega_1 + \Omega) \underbrace{\sum_{\alpha\alpha'} \sigma_{\alpha\alpha'}^\mu \sigma_{\alpha'\alpha}^\mu}_2 = \frac{-\delta_{ij}}{2\beta} \sum_{\omega_1} G(\omega_1) G(\omega_1 + \Omega). \end{aligned} \quad (3.43)$$

We do not need to evaluate the second term explicitly because the sum yields  $\text{tr}(\sigma^\mu)$ , which is 0 for every  $\mu$ .

The third term:

$$\begin{aligned} & \int_0^\beta d\tau e^{i\tau\Omega} \sum_{\alpha\alpha'\gamma\gamma'} \frac{1}{4} \sigma_{\alpha\alpha'}^\mu \sigma_{\gamma\gamma'}^\mu \int_0^\beta d\tau' G(\tau - \tau') G(\tau' - \tau) G(\tau') G(-\tau') \Gamma(1', 2'; 1, 2) \\ &= \sum_{\omega_1 \omega_2 \omega_3 \omega_4} \underbrace{\int_0^\beta d\tau e^{i\tau(\Omega + \omega_1 - \omega_2)}}_{\frac{1}{\beta} \delta(\Omega + \omega_1 - \omega_2)} \underbrace{\int_0^\beta d\tau' e^{i\tau'(\omega_2 + \omega_3 - \omega_1 - \omega_4)}}_{\frac{1}{\beta} \delta(\omega_2 + \omega_3 - \omega_1 - \omega_4)} \\ &\times G(\omega_1) G(\omega_2) G(\omega_3) G(\omega_4) \sum_{\alpha\alpha'\gamma\gamma'} \frac{1}{4} \sigma_{\alpha\alpha'}^\mu \sigma_{\gamma\gamma'}^\mu \Gamma(1', 2'; 1, 2) \\ &= - \sum_{\omega_1 \omega_3} G(\omega_1) G(\omega_1 + \Omega) G(\omega_3) G(\omega_3 + \Omega) \sum_{\alpha\alpha'\gamma\gamma'} \frac{1}{4\beta^2} \sigma_{\alpha\alpha'}^\mu \sigma_{\gamma\gamma'}^\mu \Gamma(1', 2'; 2, 1). \end{aligned} \quad (3.44)$$

Now the multi indices have fermionic frequency terms,  $\omega$ , instead of imaginary time term,  $\tau$ , i.e.  $1 = \{\omega_1 + \Omega, i, \alpha\}$ ,  $1' = \{\omega_1, i, \alpha'\}$ ,  $2 = \{\omega_2, j, \gamma\}$  and  $2' = \{\omega_2 + \Omega, j, \gamma'\}$ .

Gathering all these terms, we finally obtain a computable expression from the flow equations [4, 24].

$$\begin{aligned} \chi_{ij}^{\mu\mu}(\Omega) &= \frac{-1}{2\beta} \sum_{\omega_1} G(\omega_1) G(\omega_1 + \Omega) \delta_{ij} \\ &- \sum_{\omega_1 \omega_2} G(\omega_1) G(\omega_1 + \Omega) G(\omega_2) G(\omega_2 + \Omega) \sum_{\alpha\alpha'\gamma\gamma'} \frac{1}{4\beta^2} \sigma_{\alpha\alpha'}^\mu \sigma_{\gamma\gamma'}^\mu \Gamma(1', 2'; 2, 1), \end{aligned} \quad (3.45)$$

where we relabeled  $\omega_3$  as  $\omega_2$ . Now we can insert the vertex parametrization (3.27) discussed in the previous chapter to obtain

$$\begin{aligned} \chi_{ij}^{\mu\mu}(\Omega) &= \frac{-1}{2\beta} \sum_{\omega_1} G(\omega_1) G(\omega_1 + \Omega) \delta_{ij} - \frac{1}{4\beta^2} \sum_{\omega_1 \omega_2} G(\omega_1) G(\omega_1 + \Omega) G(\omega_2) G(\omega_2 + \Omega) \\ &\times \sum_{\lambda=0}^3 \sum_{\alpha\alpha'\gamma\gamma'} \sigma_{\alpha\alpha'}^\mu \sigma_{\gamma\gamma'}^\mu \left[ \delta_{ij} \Gamma_{ii}^{\lambda}(\omega_1, \omega_2 + \Omega; \omega_2, \omega_1 + \Omega) \sigma_{\alpha'\gamma}^\lambda \sigma_{\gamma'\alpha}^\lambda \right. \\ &\quad \left. - \Gamma_{ij}^{(\lambda)}(\omega_1, \omega_2 + \Omega; \omega_2, \omega_1 + \Omega) \sigma_{\alpha'\alpha}^\lambda \sigma_{\gamma'\gamma}^\lambda \right]. \end{aligned} \quad (3.46)$$

To simplify we need the following Pauli matrix identities :

$$\sum_{\alpha\alpha'\gamma\gamma'} \sigma_{\alpha\alpha'}^\mu \sigma_{\gamma\gamma'}^\mu \sigma_{\alpha'\alpha}^\lambda \sigma_{\gamma'\gamma}^\lambda = \text{tr}(\sigma^\mu \sigma^\lambda \sigma^\mu \sigma^\lambda) = \begin{cases} 2, & \lambda = 0, \\ 4\delta^{\mu\lambda} - 2, & \lambda \neq 0. \end{cases} \quad (3.47)$$

$$\sum_{\alpha\alpha'\gamma\gamma'} \sigma_{\alpha\alpha'}^\mu \sigma_{\gamma\gamma'}^\mu \sigma_{\alpha'\gamma}^\lambda \sigma_{\gamma'\alpha}^\lambda = \text{tr}(\sigma^\lambda \sigma^\mu)^2 = \begin{cases} 0, & \lambda = 0, \\ 4\delta^{\mu\lambda}, & \lambda \neq 0. \end{cases} \quad (3.48)$$

With these identities and using  $\Gamma^1 = \Gamma^2 = \Gamma^3$  we arrive at:

$$\begin{aligned} \chi_{ij}^{\mu\mu}(\Omega) &= \frac{-1}{2\beta} \sum_{\omega_1} G(\omega_1) G(\omega_1 + \Omega) \delta_{ij} - \frac{1}{4\beta^2} \sum_{\omega_1 \omega_2} G(\omega_1) G(\omega_1 + \Omega) G(\omega_2) G(\omega_2 + \Omega) \\ &\times \left[ 2\delta_{ij} \Gamma_{ii}^{\tilde{0}}(\omega_1, \omega_2 + \Omega; \omega_2, \omega_1 + \Omega) - 2\delta_{ij} \Gamma_{ii}^{\tilde{\mu}}(\omega_1, \omega_2 + \Omega; \omega_2, \omega_1 + \Omega) \right. \\ &\quad \left. - 4\Gamma_{ij}^{\mu}(\omega_1, \omega_2 + \Omega; \omega_2, \omega_1 + \Omega) \right]. \end{aligned} \quad (3.49)$$

Eq. (3.49) is derived following the same steps as in Refs. [4, 24], but we introduced minor corrections to the derivation.

As evident from Eq. (3.49), the spin susceptibility is constructed using vertices and Green's functions, indicating that it also flows with the renormalization flow.

To investigate the phases of the model, we use the static susceptibility, defined by setting  $\Omega = 0$ , denoted as  $\chi_{ij}(0)$  [16]. To obtain the momentum-resolved spin susceptibility we can Fourier transform Eq. (3.49) at  $\Omega = 0$  as follows [4, 24]:

$$\chi_{ij}^{\mu\mu}(\Omega = 0, \mathbf{q}) = \sum_{ij} e^{i\mathbf{q}(\mathbf{r}_i - \mathbf{r}_j)} \chi_{ij}^{\mu\mu}(0). \quad (3.50)$$

Here,  $i$  and  $j$  represent the lattice sites, while  $\mathbf{r}_i$  and  $\mathbf{r}_j$  are the real space vectors pointing to the respective lattice site. As discussed earlier in 3.1.4, we assume an infinite lattice, resulting in a continuous Brillouin zone [18].

Throughout the renormalization flow, we monitor the flow of momentum-resolved static susceptibility. As the system enters an ordered phase, a long-range order forms. This long-range order, for an infinite system, has an infinite correlation length that can be tracked by a divergence in the susceptibility flow. This effect can be observed in the static susceptibility flow as a divergence or sometimes as a cusp due to the finite size of the lattice [18, 25]. We will discuss this in more detail with examples in the following section.

Additional valuable information that can be extracted from the momentum-resolved static susceptibility is the type of order exhibited by the system. By plotting the static susceptibility in momentum space, we can identify the order of the phase by examining the peaks of  $\mathbf{q}$ . If these peaks are localized, we conclude that an ordered phase is present.

### 3. Implementation

---

Furthermore, the type of order can be inferred from the pattern in the momentum space plot. Conversely, if the flow continues down to small  $\Lambda \ll J$  values and peaks are not localized, we conclude that the system does not exhibit a symmetry-breaking order, thus it is a disordered state like a paramagnetic phase or a spin liquid phase.

Additionally, by summing Eq. (3.49) over  $\Omega$ , the equal-time correlator can be evaluated [5, 24],

$$\chi_{ij}^{\mu\mu} \Big|_{\tau=0} = \frac{1}{\beta} \sum_{\Omega} \chi_{ij}^{\mu\mu}(\Omega). \quad (3.51)$$

This equation can be evaluated efficiently by considering contributions from each two-particle reducible channel,  $\gamma_r$ , separately. Furthermore, each of these contributions can be decomposed into separate sums depending on their respective asymptotic class dependence. For more details on the evaluation of Eq. (3.51), refer to Refs. [5, 24].

## Results

In this section, we discuss the results obtained from our one-loop and two-loop pffRG calculations. First, we compare our findings with existing literature on the antiferromagnetic Heisenberg model with next-nearest-neighbor (NNN) interactions on the triangular lattice. Subsequently, we introduce long-range dipolar interactions for the same model and present our one-loop and two-loop calculation results.

In the second part of this section, we extend our analysis to the Heisenberg model on the square lattice. As in the triangular lattice case, we initially present our results for the AFM NNN interactions and then proceed to the long-range dipolar interactions. We display our results for long-range interactions by comparing them to the existing literature, and additionally, we emphasize the findings obtained from two-loop calculations.

### 4.1 Triangular Lattice

First, we present our findings for the antiferromagnetic Heisenberg model with next-nearest-neighbor interactions on the triangular lattice, comparing our results with the work of Iqbal et al. [10]. Subsequently, we examine the antiferromagnetic Heisenberg Model with dipolar long-range interactions on the triangular lattice, and we compare our one-loop results with the work of Keles and Zhao [1]. Lastly, we present our two-loop results for the same model.

#### 4.1.1 Next-Nearest-Neighbor Interactions

The NNN AFM Heisenberg model has been studied in the literature extensively, making it an ideal test case for us before moving on to the more complicated model with long-range interactions. The Hamiltonian for this model is defined as

$$H = \sum_{i,j \in \text{NN}} \mathbf{S}_i \cdot \mathbf{S}_j + \alpha \sum_{i,j \in \text{NNN}} \mathbf{S}_i \cdot \mathbf{S}_j, \quad (4.1)$$

## 4. Results

---

	$n_\Omega$	$n_\mu$	$n'_\mu$
$\Sigma(\Omega)$	4000	-	-
$\mathcal{K}_1$	400	-	-
$\mathcal{K}_2$	100	80	-
$\mathcal{K}_{2'}$	100	-	80
$\mathcal{K}_3$	50	40	40

Table 4.1: Frequency parameters for the NNN Heisenberg model on the triangular lattice

where the first sum is over nearest neighbors (NN) and the second sum over is next nearest neighbors (NNN) and  $\alpha = J_2/J_1$  and  $J_1, J_2 > 0$ . DMRG calculations [6–9] and variational Monte Carlo calculations [10] show that for  $\alpha \lesssim 0.07$ , there is a  $120^\circ$  Néel order, for  $0.07 \lesssim \alpha \lesssim 0.15$  there is a QSL, and for  $0.15 \lesssim \alpha$  there is a stripe phase. However, the nature of the QSL phase is still under debate.

As our main interest for this study lies in long-range interactions, we only compare our one-loop results with the existing literature, and we don't proceed with higher loop order calculations. As described in Chapter 3.1.5, we select a different number of points for the frequency grid of each asymptotic class. These parameters can be seen in Table 4.1. Additionally, as discussed in Chapter 3.1.4 we need to choose a cutoff radius. We select a cutoff radius of  $r_{\text{cut}} = 12$  lattice sites, which encloses a total of 517 sites which is reduced to 53 sites after using lattice symmetries.

In Fig. 4.1 we present the momentum-resolved susceptibility for different values of  $\alpha$ . By examining the position of the peaks, we can determine the type of phase observed. For  $\alpha = 0$  we see well-localized peaks at the  $K$  points of the Brillouin zone. This suggests an ordered phase with  $120^\circ$  Néel order. For  $\alpha = 0.5$  we see localized peaks at the edges of the Brillouin zone suggesting a stripe order. Moreover, within the range  $0.10 \lesssim \alpha \lesssim 0.25$ , we observe that the peaks are not well localized, which indicates the presence of a paramagnetic phase. These results are consistent with the pffRG calculations performed by Iqbal et al. [10] with a slightly narrower paramagnetic regime. However, we find a bigger paramagnetic regime compared to the results obtained by reliable methods, e.g DMRG [6, 8, 9], on the extent of the paramagnetic regime.

These results demonstrate that the pffRG can be used to provide a qualitative understanding of the phase diagram under investigation but may fall short in pinpointing the precise location of these phase transitions. Additionally, as evidenced by the number of lattice sites used in the calculation, pffRG can simulate larger systems with long-range interactions where the truncation of the system may impact the results.

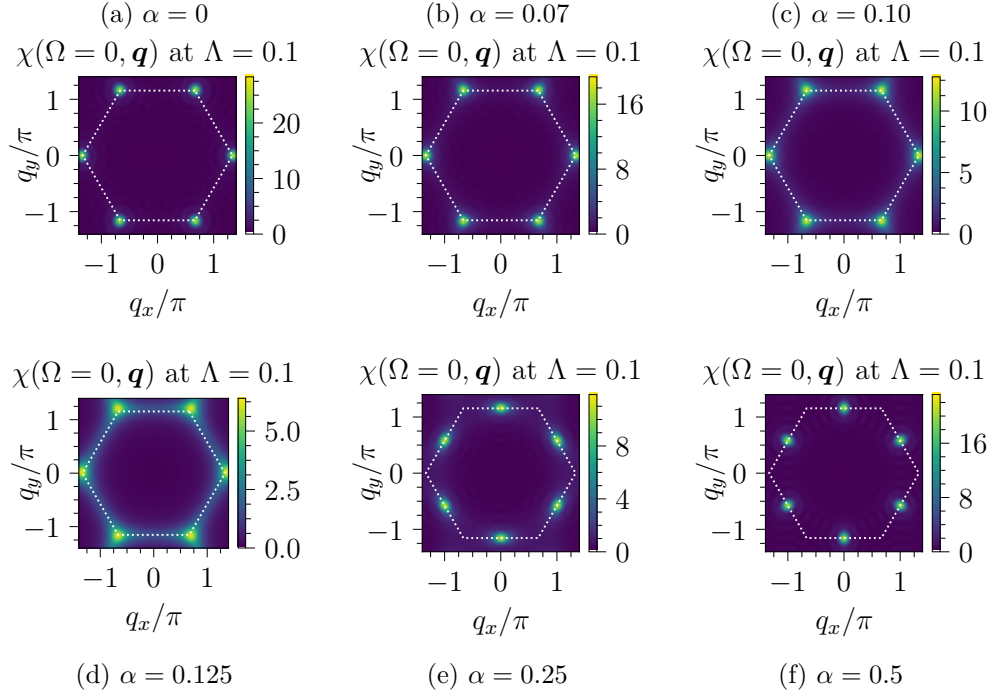


Figure 4.1: Momentum-resolved static susceptibility,  $\chi(\Omega = 0, \mathbf{q})$ , for different values of  $\alpha$ .

### 4.1.2 Long-range Interactions

In this section, we present our findings on long-range interactions for the triangular lattice, comparing them to work by Keles and Zhao [1]. Employing the same tools for investigating the phase diagram with Ref. [1], we discover a similar phase diagram that features an enlarged paramagnetic region. In the second part of this section, we present our two-loop calculations. However, we didn't analyze the phase diagram as detailed as we did for one-loop for two-loop case because of the increased numerical cost. Furthermore, we refrained from doing higher loop calculations, as the loop convergence is not guaranteed, and the recent publication by Schneider et al. [33] suggests that higher loop orders may not yield more reliable results than the first loop order.

The Hamiltonian for long-range interactions is defined as

$$H = \frac{1}{2} \sum_{ij} J_{ij} \mathbf{S}_i \cdot \mathbf{S}_j, \quad (4.2)$$

where the sum is over all lattice sites and dipolar interaction  $J(\theta, \phi)$  is defined as, [1]

$$J_{ij}(\theta, \phi) = J_0 \frac{(1 - 3(\hat{r}_{ij} \cdot \hat{d})^2)}{r_{ij}^3}. \quad (4.3)$$

## 4. Results

---

Here,  $r_{ij}$  represents the displacement vector between lattice sites  $i$  and  $j$ , and  $\hat{d}$  denotes the unit vector for dipole alignment.

$$\hat{d} = (\sin \theta \cos \phi, \sin \theta \sin \phi, \cos \theta). \quad (4.4)$$

By varying the alignment of dipoles, we observe different phases on both the triangular and the square lattice.

In the previous section, we observed that the geometric frustration of the triangular lattice leads to a paramagnetic phase. With long-range interactions, the frustration becomes more severe, leading to a broader paramagnetic region in the phase diagram.

For the dipolar interactions, we use the frequency parameters given in Table 4.2. We chose the number of frequency points such that the vertices in the flow are resolved properly. Unresolved vertices might lead to an early breakdown of the flow, or missing a divergence. We select a cutoff radius of  $r_{\text{cut}} = 8$  lattice sites, which encloses a total of 241 sites and 121 sites after using lattice symmetries. Although the lattice size is smaller compared to the previous calculations for the NNN interactions, the symmetry-reduced lattice is still four times larger, making our calculations more costly. Additionally, we tried to keep the lattice size as large as possible to better accommodate the spiral phase.

### One-loop Results

In Fig. 4.2, we present our findings for one-loop calculations. We scan the phase diagram by varying the tuning parameters  $\theta$  and  $\phi$ . Each point on the diagram represents a  $(\theta, \phi)$  pair we simulated. In total, we have simulated 82 different points. Grey points indicate the paramagnetic phase, blue points represent the stripe phase and red points correspond to the spiral phase.

Due to the expensive nature of the calculations, we were limited in the number of simulations we could perform. Consequently, we did not draw phase boundaries. In Ref. [1], the authors propose a function for calculating the smoothness of the susceptibility flow to determine the phase boundaries. However, since we can resolve vertices in more detail, these fluctuations in

	$n_{\Omega}$	$n_{\mu}$	$n'_{\mu}$
$\Sigma(\Omega)$	4000	-	-
$\mathcal{K}_1$	400	-	-
$\mathcal{K}_2$	110	110	-
$\mathcal{K}_{2'}$	110	-	110
$\mathcal{K}_3$	45	40	40

Table 4.2: Frequency parameters for the dipolar interactions on the triangular lattice

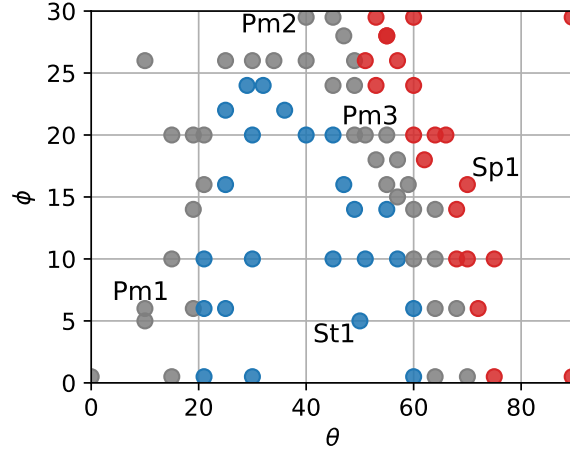


Figure 4.2: Phase diagram obtained from one-loop calculations for the Heisenberg model with dipolar interactions on the triangular lattice. The red points represent the spiral phase, the blue points indicate the stripe phase and the grey points indicate the disordered phase.

the susceptibility flow are not present in our calculations, rendering their method inapplicable. Similar to the findings in Ref. [1], we observe a wide paramagnetic regime. Our results indicate that this paramagnetic regime is even larger. Additionally, we identify the stripe and spiral phase regions in agreement with Ref. [1].

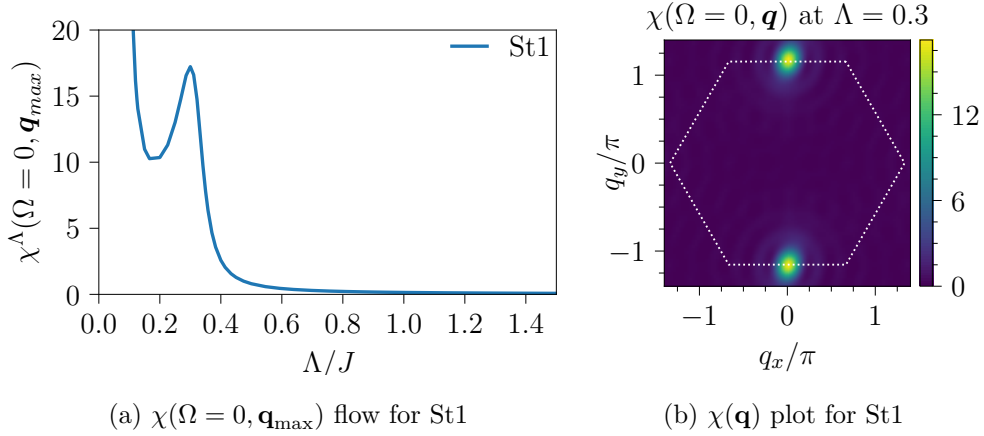


Figure 4.3: Plots for point St1, ( $\theta = 50^\circ, \phi = 5^\circ$ )

To illustrate our findings more clearly, we select several points on the phase diagram. We start with the point St1 where  $\theta = 50^\circ$  and  $\phi = 5^\circ$ , corresponding to the M1 point in Ref. [1]. In Fig. 4.3b, we depict the momentum resolved susceptibility at  $\Lambda/J = 0.35$ . The susceptibility  $\chi(\mathbf{q})$  exhibits localized peaks

## 4. Results

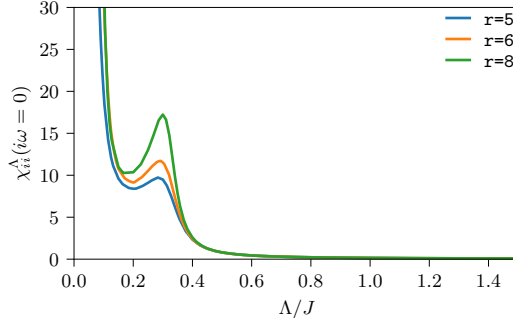
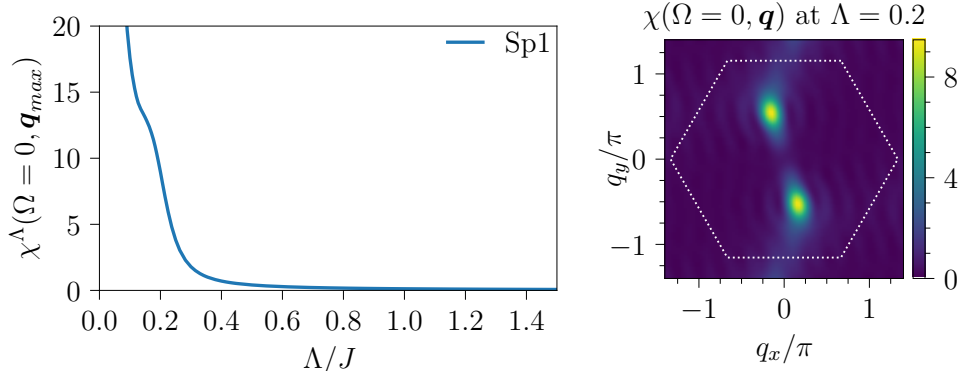


Figure 4.4: Scaling of local maximum with  $r_{\text{cutoff}}$  for St1 point. The blue curve has  $r_{\text{cutoff}} = 5$ , and as we increase the cutoff radius we observe the local maximum scales. Extrapolating this to the thermodynamic limit, we observe a divergence instead of a local maximum.

at the M point of the Brillouin zone, indicating a stripe order. Moreover, by examining the flow of susceptibility at  $\mathbf{q}_{\text{max}}$ , we observe a local maximum occurring around  $\Lambda/J \sim 0.3$ . In order to interpret this local maximum we vary the  $r_{\text{cut}}$  and perform more calculations. In Fig. 4.4, we observe that this local maximum scales with the number of lattice sites. Consequently, in the thermodynamic limit, this point can be extrapolated to infinity suggesting a divergence for  $\chi(\mathbf{q}_{\text{max}})$  at a critical  $\Lambda_c$ . This is also consistent with our findings of momentum space plots exhibiting an ordered phase. Therefore, we conclude that point St1 exhibits characteristics of a stripe phase.



(a)  $\chi(\Omega = 0, \mathbf{q}_{\text{max}})$  flow for Sp1

(b)  $\chi(\mathbf{q})$  plot for Sp1

Figure 4.5: Plots for point Sp1, ( $\theta = 70, \phi = 16$ )

Next, we investigate the other ordered phase, the spiral order. We select the point labeled Sp1 as a demonstrative example. Upon examining the susceptibility flow (see Fig. 4.5a), we observe that the susceptibility flow extends to low  $\Lambda$  values without diverging. Although the flow is not smooth and has some features around  $\Lambda/J \sim 0.2$ , we don't make any conclusive inferences from

the susceptibility flow. However, by analyzing the contour plot for  $\chi(\mathbf{q})$  at  $\Lambda/J = 0.2$  in Fig. 4.5b, we find that the peaks are localized inside the Brillouin zone and do not coincide with any of the high-symmetry points. This evidence suggests the existence of a spiral phase.

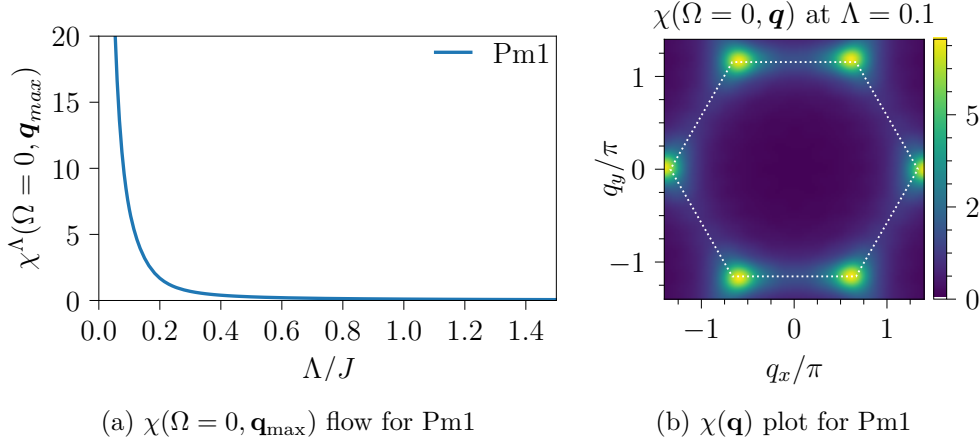
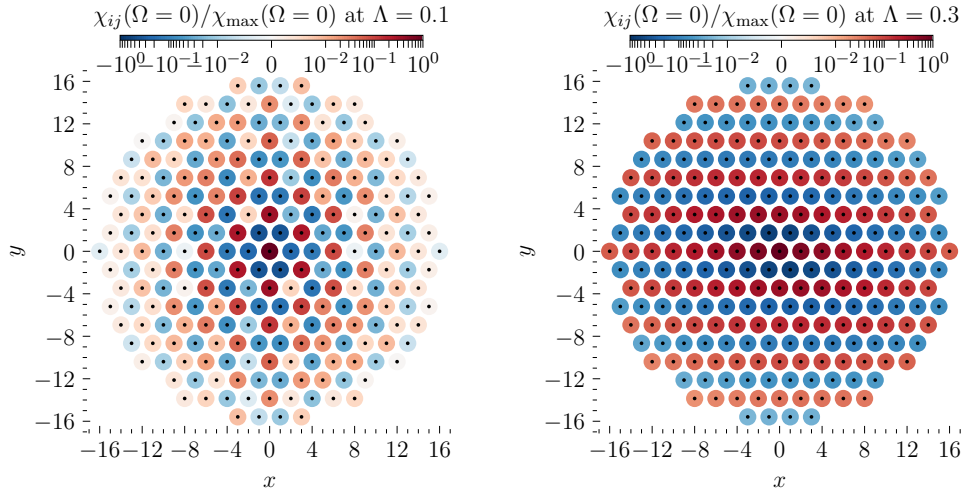


Figure 4.6: Plots for point Pm1, ( $\theta = 10, \phi = 6$ )



(a) Real space plot of Pm1 at  $\Lambda/J = 0.1$  (b) Real space plot for St1 at  $\Lambda/J = 0.3$

Figure 4.7: We can see that at the lattice boundaries St1 has high correlations at  $\Lambda/J = 0.3$  but Pm1 has correlations that are limited to the short-range scale at  $\Lambda/J = 0.1$ . This shows that Pm1 has no long-range order.

Having explored the ordered phases, we will now shift our focus to disordered phases, starting with the point designated as Pm1 at ( $\theta = 10, \phi = 6$ ). We note that the susceptibility flow for the Pm1 point is smooth and continuous for  $\Lambda \rightarrow 0$ . Moreover, upon examining the contour plot in Fig. 4.6b we see

#### 4. Results

that peaks are not well localized compared to the ordered phases, even at a low  $\Lambda$  value  $\Lambda/J \ll 0.1$ . Although the susceptibility plot in momentum space suggests a  $120^\circ$  Néel order, it only exhibits short-range correlations, with a lack of long-range order. In Fig. 4.7, we also present a plot of the real space correlations for the point PM1 at  $\Lambda/J = 0.1$ . To demonstrate the absence of long-range correlations, and for comparison, we also include an example of an ordered phase, the real space correlations for point St1 at  $\Lambda/J = 0.3$ .

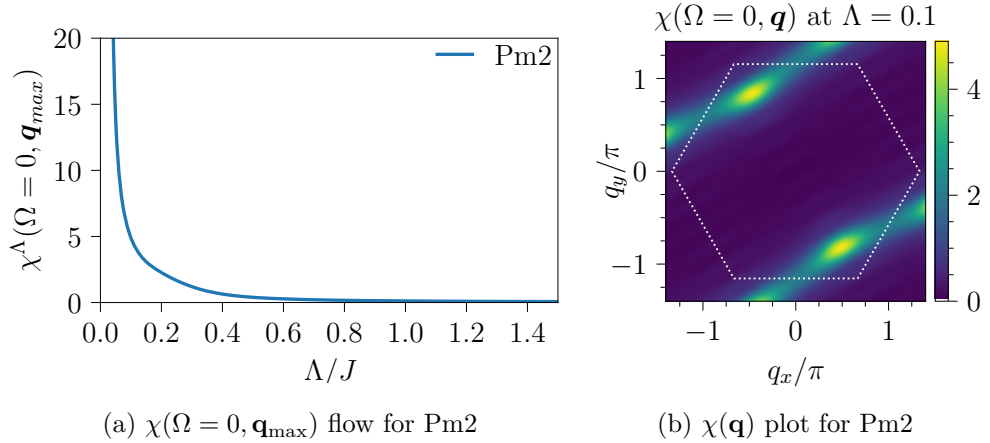


Figure 4.8: Plots for point Pm2, ( $\theta = 40, \phi = 30$ )

Next, we choose another disordered phase labeled as Pm2 located at ( $\theta = 40, \phi = 30$ ). The momentum-resolved susceptibility at  $\Lambda/J = 0.1$  in Fig. 4.8b shows peaks inside the Brillouin zone. However, it is evident that these peaks are not well localized and smeared out. Moreover, in Fig. 4.8a we see that the flow goes smoothly  $\Lambda \rightarrow 0$ . These two findings suggest that we find a paramagnetic phase at the Pm2 location in agreement with Ref. [1].

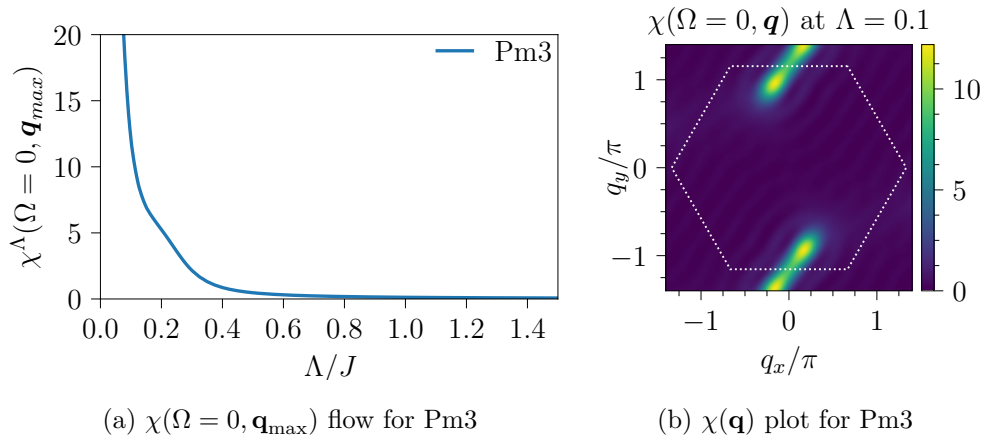


Figure 4.9: Plots for point Pm3, ( $\theta = 51, \phi = 20$ )

Lastly, we choose another point located between the stripe and spiral phase boundaries, labeled as Pm3 and located at  $(\theta = 51, \phi = 20)$  (See Fig. 4.9). The susceptibility flow has a feature around  $\Lambda/J \sim 0.2$ , but yet the flow does not diverge or break down. Furthermore, upon examining the contour plot, we observe that the peak is not well-localized at lower lambda values. These two findings lead us to believe that the Pm3 point is also a disordered phase.

### Two-loop Results

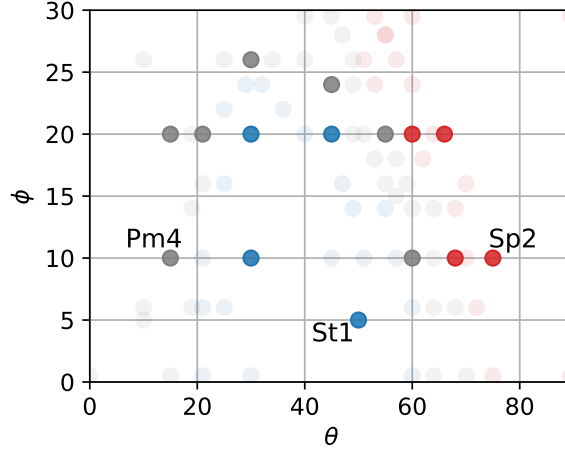


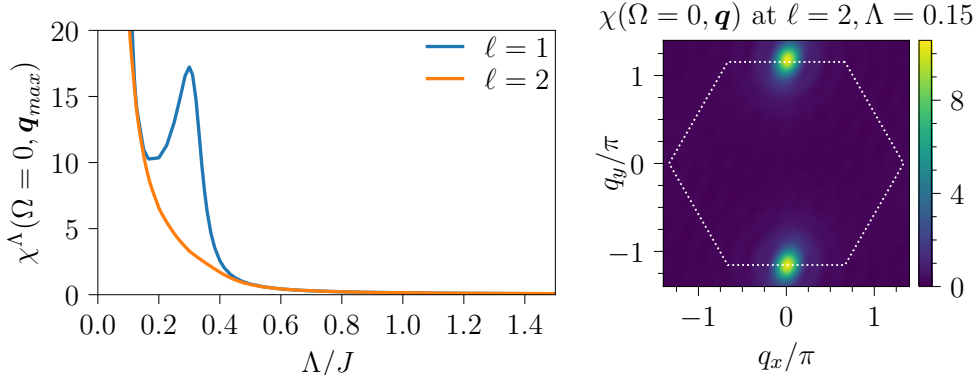
Figure 4.10: Phase diagram obtained from two-loop calculations for the Heisenberg model with dipolar interactions on the triangular lattice. The color code is identical to the one-loop phase diagram. The transparent points represent the one-loop results, and the thick-colored points represent the two-loop results.

In this section, we present our two-loop calculations. We limited our calculations to the second loop order, as the numerical cost would exceed available resources. We sample only 15 points for the two-loop calculations to determine if there are alterations in the phase diagram.

Previously, by including more diagrams in the flow equation, changes in the phase boundary were observed for the AFM Heisenberg model on the kagome lattice [4, 5]. Surprisingly, we didn't observe any change in the long-range interactions on the triangular lattice. We present our findings in Fig. 4.10 for two-loop calculations, retaining the phase boundaries obtained from one-loop calculations.

First, we focus our attention on the St1 point which we thoroughly investigated in the previous section. We compare the one-loop and two-loop results in Fig. 4.11. We observe that the local maximum in one loop calculation disappears when we transition to the two-loop, but there still is a clear divergence occurring at a finite  $\Lambda$ . Thus, by the inclusion of more diagrams into the flow equations, the critical value of  $\Lambda$  changed. Moreover, upon examining the contour plot, we observe that peaks are well localized at a high-symmetry point of the Brillouin zone, suggesting the presence of a stripe order.

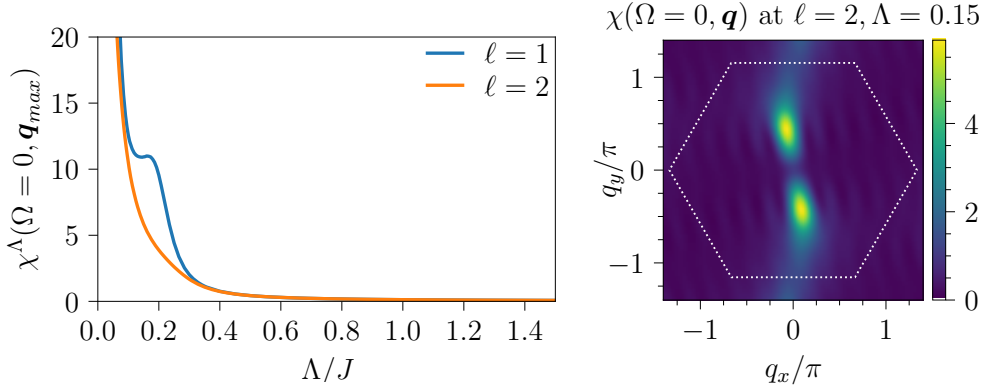
Next, we turn our attention to the results for a spiral-ordered point on the phase diagram, specifically the point Sp2 located at  $(\theta = 75, \phi = 10)$ . We present our results for this point in Fig. 4.12. Similar to the St1 point, we



(a)  $\chi$  flow for St1. The orange curve is the two-loop (b)  $\chi(\mathbf{q})$  plot for two-loop at St1. flow and the blue curve is the one-loop flow.

Figure 4.11: Plots for point St1, ( $\theta = 50, \phi = 5$ ) from two-loop calculations

observe that the local maximum disappears. However, the flow diverges at a finite  $\Lambda$  value. Moreover, observing the contour plot, we note the localized peaks inside the Brillouin zone, indicative of a spiral phase.



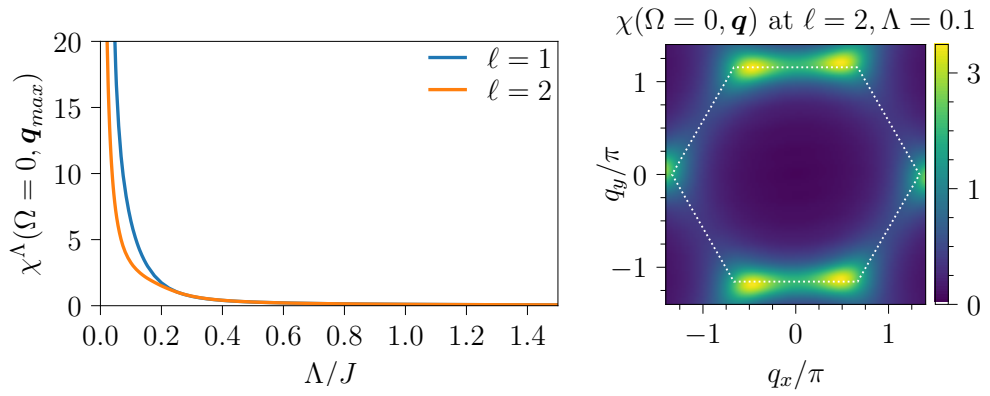
(a)  $\chi$  flow for Sp2. The orange curve is the two- (b)  $\chi(\mathbf{q})$  plot for two-loop at St1. loop flow and the blue curve is the one-loop flow.

Figure 4.12: Plots for point Sp2, ( $\theta = 75, \phi = 10$ ) from two-loop calculations

Lastly, we investigate one of the paramagnetic points on the phase diagram. For this analysis, we select the Pm4 point located at ( $\theta = 15, \phi = 10$ ). As illustrated in Fig. 4.13b, both the one-loop and two-loop susceptibility flows smoothly progress down to low  $\Lambda$  values. With the inclusion of more diagrams into flow equations, we see that divergence occurs at a smaller  $\Lambda$  values for two-loop calculation at this point. Examining the susceptibility contour plot in Fig. 4.13b, we notice that peaks are not localized and the maximum of the peaks are spread out around the high symmetry points of the Brillouin zone. This indicates the Pm4 point exhibits characteristics of a disordered phase.

#### 4. Results

---



(a)  $\chi$  flow for Pm4. The orange curve is the two-loop flow and the blue curve is the one-loop flow. (b)  $\chi(\mathbf{q})$  plot for two-loop at Pm4.

Figure 4.13: Plots for point Pm4, ( $\theta = 15, \phi = 10$ ) from two-loop calculations

In conclusion, we did not observe any changes to the phase boundaries for the two-loop calculations.

## 4.2 Square Lattice

Now, we shift our focus to the Heisenberg model on the square lattice. In the first part of this section, we briefly discuss the NNN AFM Heisenberg model on the square lattice. Following that, we move on to the long-range interactions, providing a more detailed analysis.

### 4.2.1 Next-Nearest-Neighbor Interactions

	$n_\Omega$	$n_\mu$	$n'_\mu$
$\Sigma(\Omega)$	4000	-	-
$\mathcal{K}_1$	400	-	-
$\mathcal{K}_2$	110	110	-
$\mathcal{K}_{2'}$	110	-	110
$\mathcal{K}_3$	45	40	40

Table 4.3: Frequency parameters for the NNN interactions on the square lattice

As previously discussed in Chapter 2.1.2, the NNN model has been the subject of extensive research using other reliable methods such as DMRG [12, 13], ED [15] and, more recently, PEPS [14] to investigate the phase diagram of the square lattice and the nature of the underlying QSL phase. Although all methods [12–15] including a previous pffRG study by Reuther and Wölfle [18] agree that between the two ordered phases, there is a magnetically disordered phase, the nature of this regime is under discussion.

The Hamiltonian for this model is identical to the triangular lattice Hamiltonian as defined in Eq. (4.1). As found in the literature, for  $\alpha \lesssim 0.35 \dots 0.45$ , the model exhibits a Néel ordered phase and for  $0.6 \dots 0.65 \gtrsim \alpha$ , it exhibits the stripe phase. Furthermore, it has been shown that there is a non-magnetic region between the two ordered phases [12–15, 18].

We compare our findings for the AFM NNN Heisenberg model with previous pffRG calculations [16] and the rest of the literature [12–15] to evaluate the consistency of the phases we find for different parameters.

For our calculation in this section, we use the frequency parameters given in Table 4.4. We choose cutoff radius as  $r_{\text{cutoff}} = 8$  enclosing 197 lattice sites which is reduced to 32 lattice sites using lattice symmetries.

First, we examine the two ordered phases. For this purpose, we first look at  $\alpha = 0.35$  where we anticipate a Néel order. Examining the flow illustrated in Fig. 4.14a, we observe a small kink around  $\Lambda/J = 0.25$  where the flow already shows diverging behavior, hinting at a possible phase transition. To substantiate this hypothesis, we inspect the contour plot depicted in Fig. 4.14 at  $\Lambda/J = 0.25$  for the momentum-resolved susceptibility peaks. We observe that the plot has well-localized peaks at the corners of the Brillouin zone at a relatively high  $\Lambda$  value, confirming our expectations of finding a Néel order.

#### 4. Results

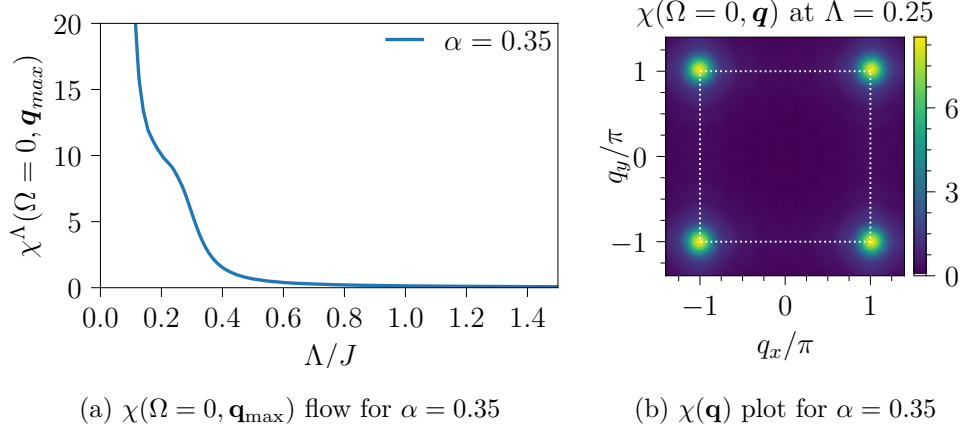


Figure 4.14: Plots for  $\alpha = 0.35$

For the second ordered phase, we examine the  $\alpha = 0.75$  calculations, where we expect to find a stripe order. In Fig. 4.15a, we observe a noticeable kink in the susceptibility flow around  $\Lambda = 0.2$ . However, since a local maximum does not appear, we investigate the contour plot before confidently concluding that this is an ordered phase. In Fig. 4.15b, we observe that the maxima are well-localized at the edges of the Brillouin zone, and there is no significant smearing of the peaks. Taking both observations into account, we conclude that for  $\alpha = 0.75$  the model exhibits stripe ordering.

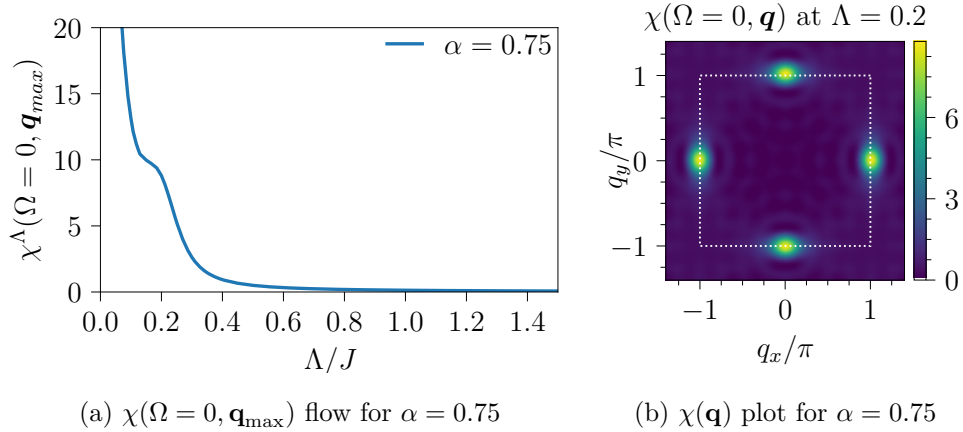


Figure 4.15: Plots for  $\alpha = 0.75$

For the paramagnetic region, we present the results obtained at  $\alpha = 0.6$ . In Fig. 4.16a, we observe that the susceptibility flow is smooth down to  $\Lambda \rightarrow 0$ . Moreover, examining the susceptibility plot at  $\Lambda/J = 0.05$  in Fig. 4.16b, we observe that the peaks are not localized and the maximum is smeared out evenly along the entire Brillouin zone boundary. However, because pffRG

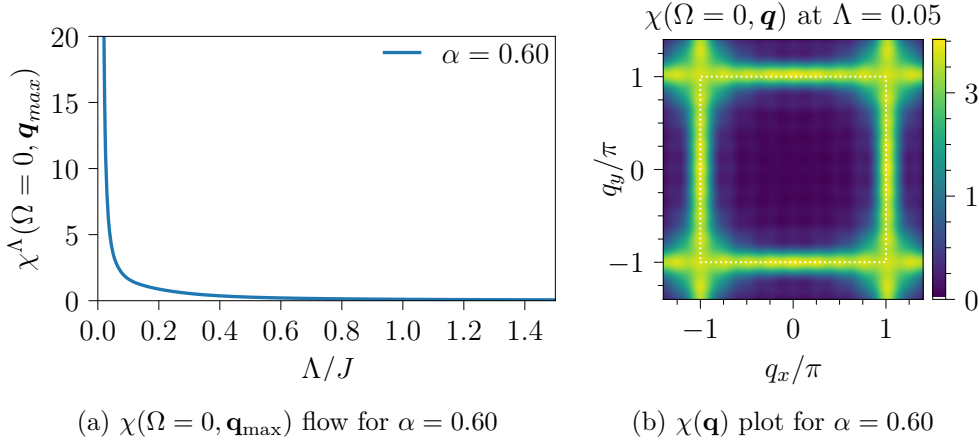
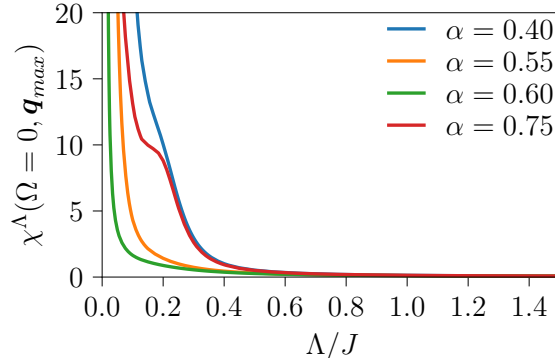
Figure 4.16: Plots for  $\alpha = 0.60$ 

Figure 4.17: Flow of maximum of the susceptibility for  $\alpha = 0.40$  in blue,  $\alpha = 0.55$  in orange,  $\alpha = 0.60$  in green and  $\alpha = 0.75$  in red. The orange and green curves that are classified as magnetically disordered are smooth down to  $\Lambda \rightarrow 0$ . Conversely, the curves representing magnetically ordered phases (blue and red) have kinks and have diverging behavior before around  $\Lambda/J \sim 0.3$ .

calculations do not break the lattice symmetries, we cannot probe into the paramagnetic regime to check if it is a QSL or a VBS.

We observe the emergence of this paramagnetic phase around  $0.50 \lesssim \alpha$ , where the susceptibility flow becomes smooth down to  $\Lambda \rightarrow 0$ . As the value of  $\alpha$  increases, the flow remains smooth, and the smearing of the peaks becomes more visible along the Brillouin zone boundary. Around  $\alpha \sim 0.65$ , the peaks begin to localize again, and a kink appears in the susceptibility flow, and we observe a stripe phase forming. Thus, we estimate the paramagnetic regime to be situated between  $0.50 \lesssim \alpha \lesssim 0.65$  which is a narrower range compared to the literature [12–15].

We believe further investigation is required to accurately determine the phase boundaries and the nature of the paramagnetic regime. For a more

detailed study of AFM Heisenberg model with NNN interactions on the square lattice using pffRG, we refer the reader to the Ref. [18].

### 4.2.2 Long-range Interactions

In this section, we present our results obtained from one-loop and two-loop pffRG calculations for the Heisenberg model with long-range interactions on the square lattice. This model exhibits three ordered phases [2, 17].

The Heisenberg model with long-range interactions on the square lattice has been previously investigated by Keles and Zhao using pffRG in Ref. [2], and by Zou et.al. through the use of PEPS, Schwinger-boson mean field (SBMF) and modified spin wave theory in Ref. [17]. In their research, Zou et al. find a paramagnetic regime between stripe and Néel phases using PEPS and SBFM, while with the use of spin wave theory, they locate a paramagnetic regime at the intersection of three ordered phases [17]. However, their method of solving the model retained only the NN and NNN couplings. In addition, the finite lattice size limitations of the tensor network ansatz prevent an accurate representation of the spiral phase, thus precluding the extension of the phase diagram towards the region where the spiral phase exists. To circumvent these constraints, Keles and Zhao employed pffRG in Ref. [2], which can be extended to infinite lattice sizes and can accommodate long-range interactions. In their investigation, they identified a paramagnetic regime at the juncture of the three ordered phases. In the next section, we will compare our one-loop results to the work of Keles and Zhao [2].

For our calculations in the next section, we use the frequency parameters given in Table 4.4. Analogous to the triangular lattice, we select a cutoff radius of 8 lattice sites, encompassing a total of 197 sites, which is reduced to 99 sites after applying lattice symmetries.

	$n_\Omega$	$n_\mu$	$n'_\mu$
$\Sigma(\Omega)$	4000	-	-
$\mathcal{K}_1$	400	-	-
$\mathcal{K}_2$	110	110	-
$\mathcal{K}_{2'}$	110	-	110
$\mathcal{K}_3$	45	40	40

Table 4.4: Frequency parameters for the dipolar interactions on the square lattice

### One-loop Results

In this section, we explore the phase diagram by varying the orientation of dipoles, similar to our approach with the triangular lattice. Each point on the diagram represents a  $(\theta, \phi)$  pair we simulated. Following the same color

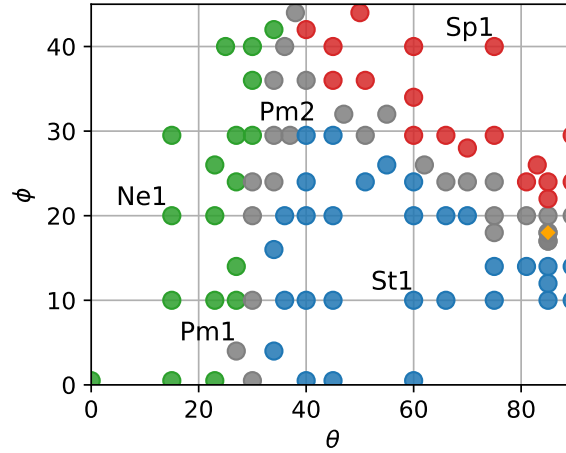


Figure 4.18: Phase diagram obtained from one-loop calculations for the dipolar Heisenberg model on the square lattice. Green points represent the Néel order phase, blue points represent the stripe order phase, red points represent the spiral order phase, and grey points represent the disordered phase.

scheme as with the triangular lattice, the grey points indicate the disordered phase, the blue points represent the stripe order, the red points denote the spiral order, and introducing green points, which now represent the Néel order. The phase diagram resulting from 94 one-loop calculations is depicted in Fig. 4.18. Due to the limited number of calculations performed, we did not attempt to pinpoint the exact phase boundaries.

In Ref. [2], the authors identify a paramagnetic region along the phase boundaries of the Néel phase, expanding notably where three phase boundaries intersect. Consistent with their result, we also identify a wider paramagnetic regime where the three-phase boundaries meet. Overall, the paramagnetic regime we find is slightly smaller compared to the findings in Ref. [2], but we mostly agree with the results. However, unlike in Ref. [2], we observe a paramagnetic regime between the spiral and stripe phases, located along the boundary of the stripe and spiral phase.

To illustrate the different ordered phases of the model, we inspect a few illustrative points. We start with the Néel order. As an example, we choose the point labeled as Ne1 located at  $(\theta = 15^\circ, \phi = 20^\circ)$ . Examining the susceptibility flow in Fig. 4.19a, we observe that the flow is smooth up to  $\Lambda/J \sim 0.2$ . At around  $\Lambda/J \sim 0.2$ , a kink emerges within the susceptibility flow, indicating a potential phase transition. To substantiate this, we examine the contour plot at  $\Lambda = 0.2$ , as illustrated in Fig. 4.19b. The contour plot presents well-localized peaks at the corners of the Brillouin zone, characteristic of a Néel order. Based on these observations, we infer that the Ne1 point corresponds to a Néel ordered phase.

#### 4. Results

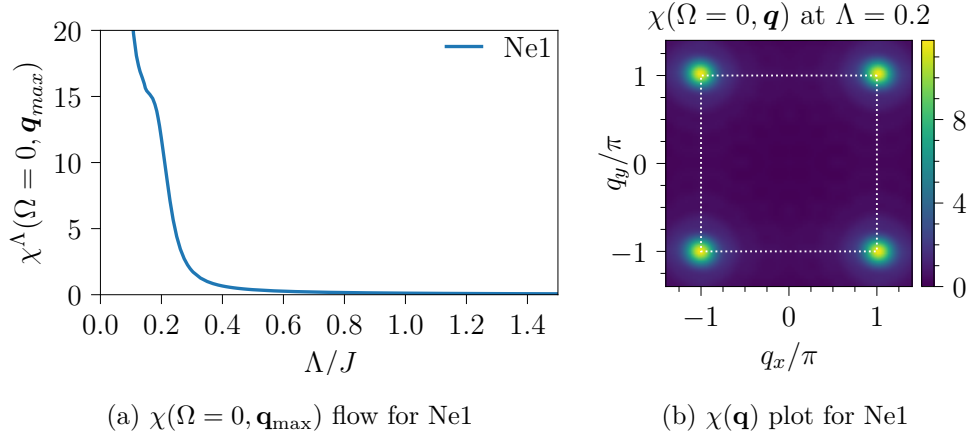


Figure 4.19: Plots for point Ne1, ( $\theta = 15^\circ, \phi = 20^\circ$ )

Next, we inspect the second ordered phase, the stripe phase. For this purpose, we select the point labeled as St1 situated at ( $\theta = 60^\circ, \phi = 10^\circ$ ). Initially, we observe the flow of susceptibility with respect to the flow parameter  $\Lambda$  where a local maximum occurs around  $\Lambda/J \sim 0.25$ . Mirroring our approach in the triangular model, we investigate this point using different lattice sizes and find that this local maximum scales with an increasing number of lattice sites. The scaling of the local maximum with lattice sites is illustrated in Fig. 4.21. Hence, we conclude that at the thermodynamic limit there is a phase transition at around  $\Lambda/J \sim 0.25$ . To identify the type of order for this point, we inspect the contour plot depicted in Fig. 4.20. We see that the peaks are well localized at the edges of the Brillouin zone suggesting a stripe order.

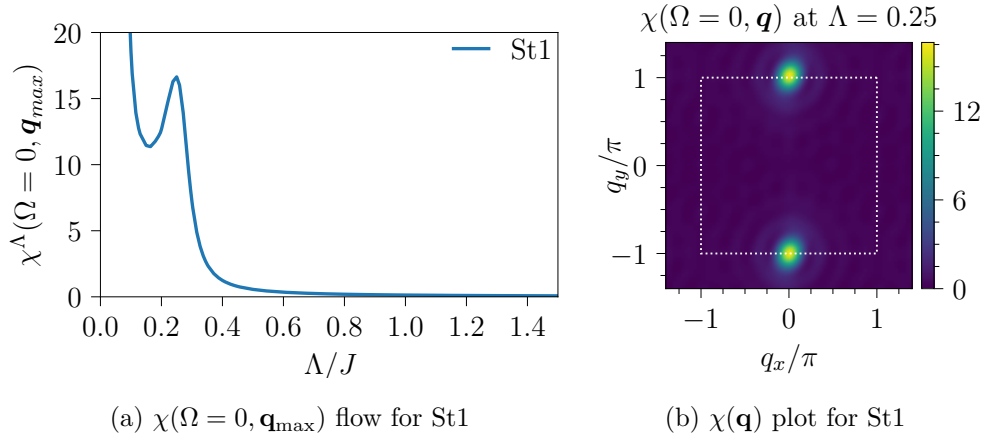


Figure 4.20: Plots for point St1, ( $\theta = 10^\circ, \phi = 6^\circ$ )

For the final ordered phase, we undertake an analysis of the point labeled as Sp1, located at ( $\theta = 75^\circ, \phi = 40^\circ$ ). Upon inspecting the flow of the susceptibility, we observe a local maximum appearing around  $\Lambda/J \sim 0.4$ . Varying

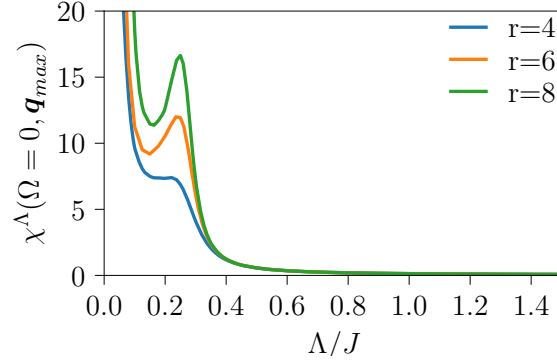


Figure 4.21: Susceptibility flow of point St1 with different lattice sizes. The blue line, orange line, and green line represent susceptibility flow with  $r_{\text{cutoff}} = 4$ ,  $r_{\text{cutoff}} = 6$ , and  $r_{\text{cutoff}} = 8$ . We observe a local maximum around  $\Lambda/J \sim 0.25$ , which scales with increasing lattice size.

the lattice size, we notice that the peak scales with the number of lattice sites included in the calculation, as is evident from Fig. 4.23. Additionally, we observe that the  $\Lambda$  value at which the local maximum emerges shifts towards lower values as the number of lattice sites decreases. This is likely because the spiral phase necessitates a larger lattice size for an accurate representation, an aspect that has posed challenges for the other methods. By inspecting the contour plot around  $\Lambda = 0.4$ , where the local maximum occurs, we observe localized peaks at a non-high symmetry point of the Brillouin zone suggesting a spiral order.

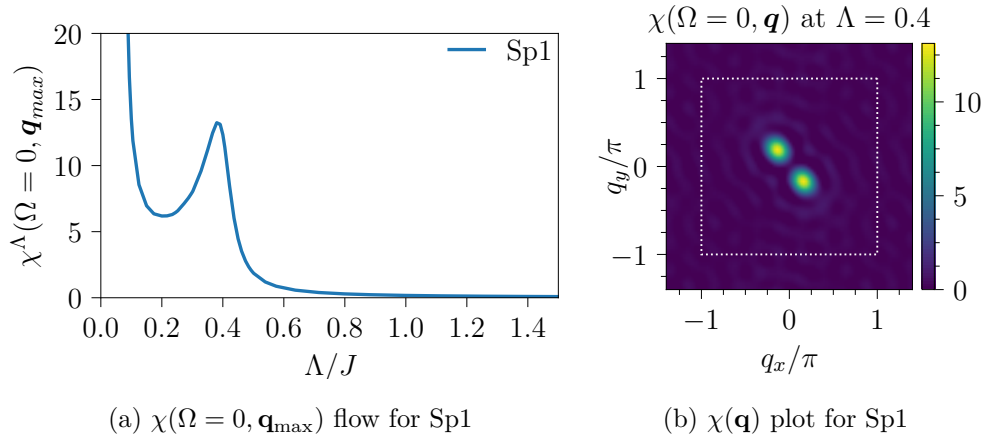


Figure 4.22: Plots for point Sp1, ( $\theta = 75^\circ$ ,  $\phi = 40^\circ$ )

Next, we investigate the paramagnetic points on the phase diagram. For the initial example, we select the point labeled as PM1 located at ( $\theta = 27^\circ$ ,  $\phi = 4^\circ$ ), positioned between the stripe and the Néel order. The susceptibility flow for this point is illustrated in Fig. 4.24a. We notice that the flow remains smooth

#### 4. Results

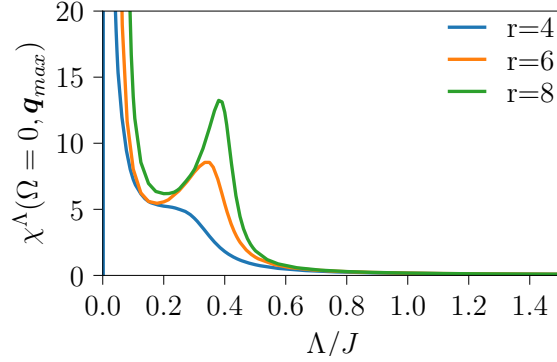
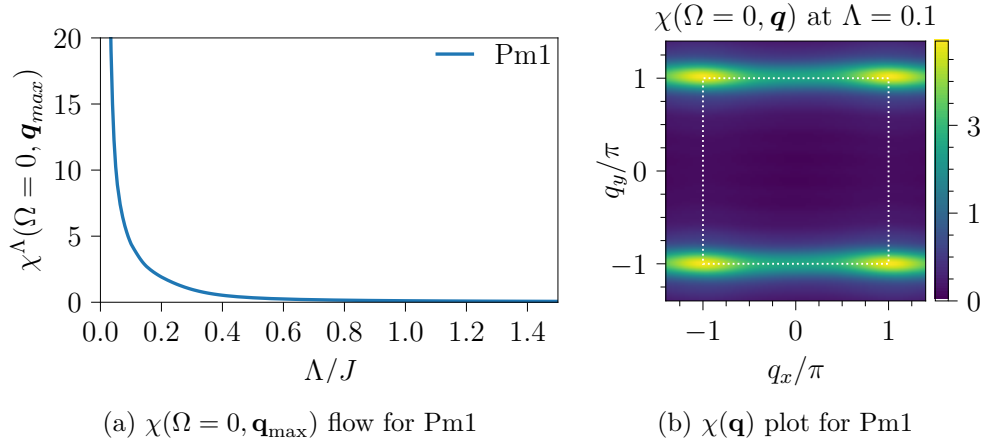


Figure 4.23: Susceptibility flow of point Sp1 with different lattice sizes. The blue line, orange line, and green line represent susceptibility flow with  $r_{\text{cutoff}} = 4$ ,  $r_{\text{cutoff}} = 6$ , and  $r_{\text{cutoff}} = 8$ . We observe a local maximum around  $\Lambda/J \sim 0.4$  for  $r_{\text{cutoff}} = 8$  which shifts to lower  $\Lambda$  values for decreasing lattice size.

down to  $\Lambda \rightarrow 0$ , hinting at an absence of order. We then turn our attention to the contour plot for the momentum-resolved static susceptibility. We observe that the peaks in the contour plot are smeared out along the boundary of the Brillouin zone and do not exhibit clear localization. These combined observations lead us to categorize this point as a paramagnetic phase.

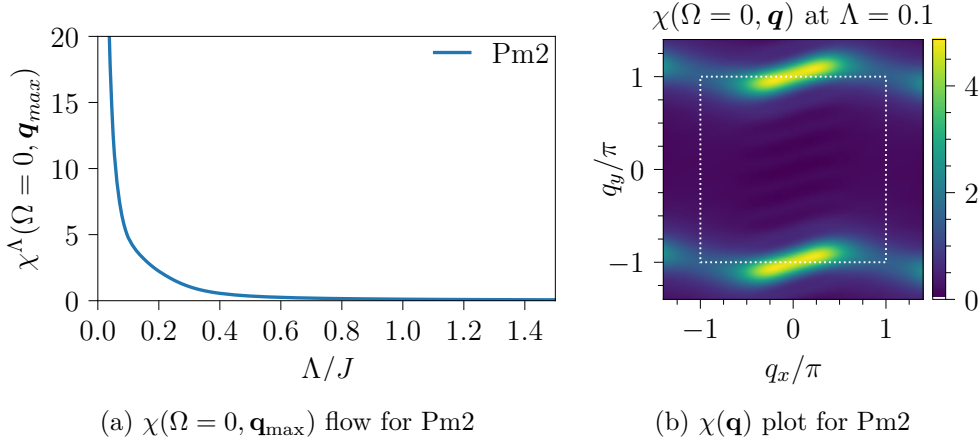


(a)  $\chi(\Omega = 0, \mathbf{q}_{\text{max}})$  flow for Pm1

(b)  $\chi(\mathbf{q})$  plot for Pm1

Figure 4.24: Plots for point Pm1, ( $\theta = 27^\circ, \phi = 4^\circ$ )

Next, we select a point situated around where the three ordered phases intersect, labeled as PM2 at ( $\theta = 37^\circ, \phi = 30^\circ$ ). Similar to the Pm1 point, we observe that the susceptibility flow in Fig. 4.25a goes smoothly to  $\Lambda \rightarrow 0$ . We then examine the contour plot depicted in Fig. 4.25b. We note that the peaks are not well localized and appear smeared out, extending from the edges of the Brillouin zone towards the center. Moreover, we observe a considerable shift in the smear of the peaks compared to the PM1 point. Based on these

Figure 4.25: Plots for point Pm2, ( $\theta = 37^\circ, \phi = 30^\circ$ )

observations, we conclude that the PM2 point is indicative of a paramagnetic phase.

Finally, we turn our attention to the Pm3 point located at ( $\theta = 85^\circ, \phi = 18^\circ$ ) denoted by an orange rhombus, which lies between the boundary of the spiral and stripe phase. Upon inspecting the susceptibility flow in Fig. 4.26a, we observe that the flow is almost smooth down to  $\Lambda \rightarrow 0$ . Further analysis of the contour plot depicted in Fig. 4.26b at  $\Lambda/J = 0.1$  reveals that the peaks are smeared out, extending from the edges of the Brillouin zone towards the center. Based on these observations, we classify PM3 as a paramagnet.

In Ref. [17] Zout et al., the TN ansatz couldn't extend to this region due to lattice size limitations, and no trace of a paramagnetic phase was found using SBMF. Moreover, in Ref. [2] Keles and Zhao using pffRG find a narrow region of width  $\phi \sim 2^\circ$  where they observed smearing of peaks in the contour plot of momentum resolved static susceptibility and an almost smooth flow of susceptibility to the infrared cutoff. However, they did not classify it as a paramagnet as they did not observe a significantly different behavior of the flow around this boundary. Conversely, we find this region to have a width around  $\phi \sim 5^\circ$ , and we observe a qualitative difference in the susceptibility flow. To justify this claim, we take a vertical cut of the phase diagram at  $\theta = 85^\circ$  starting from the stripe phase at  $\phi = 14^\circ$ . We present the maximum of the susceptibility flow of the four points that have  $\phi = 14^\circ, \phi = 18^\circ, \phi = 20^\circ$  and  $\phi = 22^\circ$  in Fig. 4.27. We observe that disordered points have a noticeably suppressed susceptibility flow compared to the ordered ones. Therefore, we conclude that there is a disordered phase with no long-range order in this region.

## Two-loop Results

In this section, we present our two-loop calculations for the dipolar interactions on the square lattice. However, as the cost of higher loop calculations

#### 4. Results

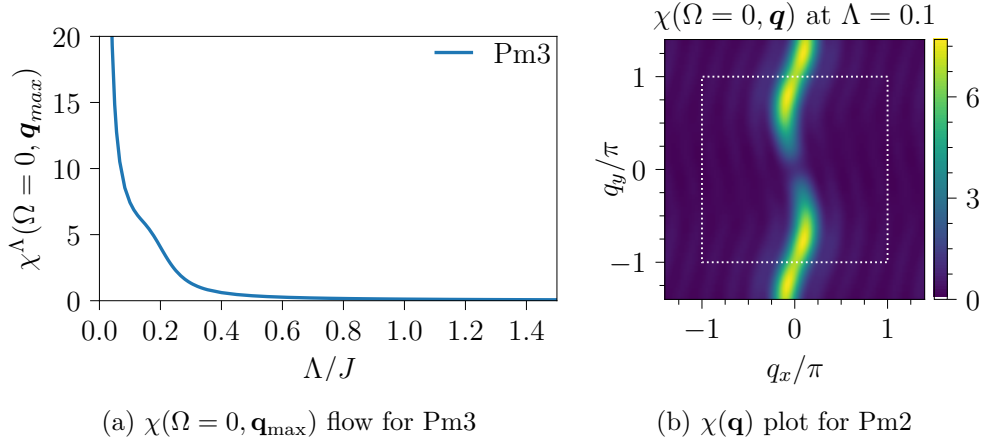


Figure 4.26: Plots for point Pm3, ( $\theta = 85^\circ, \phi = 18^\circ$ )

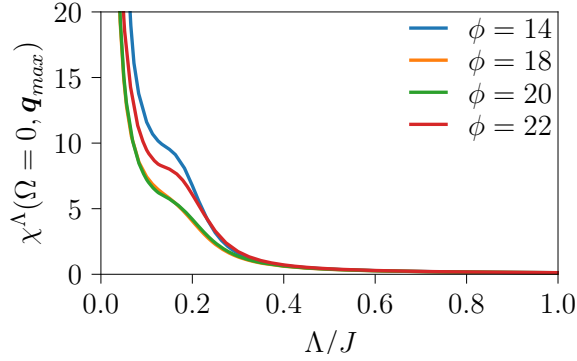


Figure 4.27: The plot for the susceptibility flow along the cut taken at  $\theta = 85^\circ$ . The stripe (blue,  $\phi = 14^\circ$ ) order and the spiral (red,  $\phi = 2^\circ$ ) order susceptibility flow have a diverging behavior around  $\Lambda/J \sim 0.2$  where a kink appears in the flow. We observe a suppression for the susceptibility flow of the paramagnetic points in green ( $\phi = 20^\circ$ ) and orange ( $\phi = 18^\circ$ ) curves.

scales linearly with the loop order, these calculations become more expensive. As such, we have chosen to refrain from higher-loop calculations and limit ourselves to a few exemplary points for the two-loop calculations. Our results from these 12 calculations are presented in Fig. 4.29. We selected points near the phase boundaries for sampling. Interestingly, the results from the one-loop calculations largely coincide with those from the two-loop order, showing no significant differences in the phase boundaries. We replicate the same analysis we conducted in the previous sections for the chosen points.

Firstly, we examine a point labelled as Ne2, which is Néel ordered and located at ( $\theta = 23^\circ, \phi = 20^\circ$ ). In Fig. 4.30a the susceptibility flow of both one-loop and two-loop susceptibility flow is depicted. We observe that for the two-loop susceptibility, flow is almost smooth down to  $\Lambda \rightarrow 0$ . Yet, upon inspecting the contour plot, we notice that the localization of peaks starts

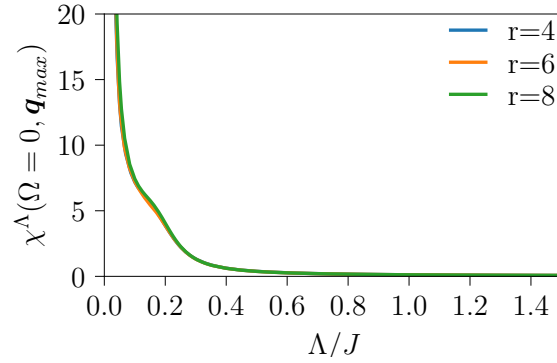


Figure 4.28: The Pm3 point, evaluated with various lattice sizes, shows that the kink in the susceptibility flow does not scale with an increase in lattice size.

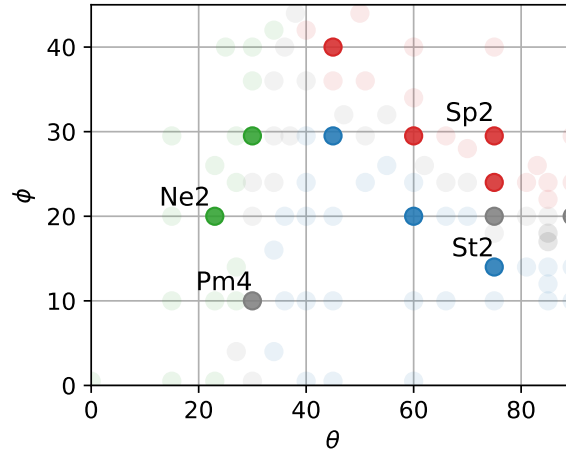
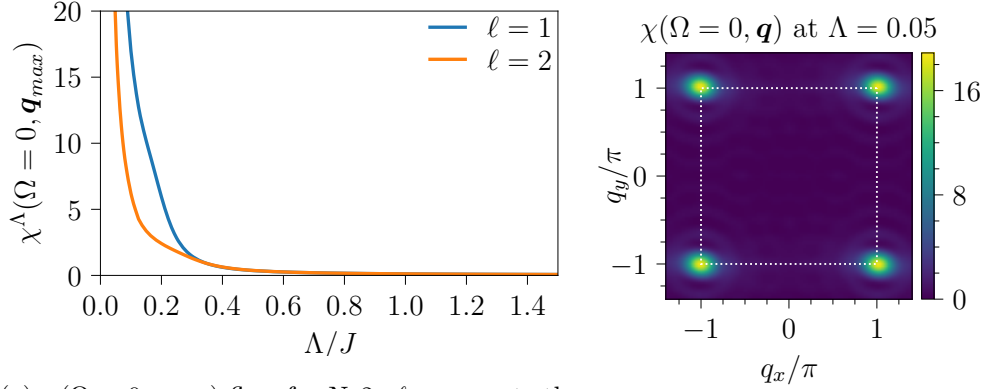


Figure 4.29: Phase diagram obtained from two-loop calculations for the Heisenberg model with dipolar interactions on the square lattice. The color code is identical to the one-loop phase diagram. The transparent points represent the one-loop results, and the thick-colored points represent the two-loop results.

occurring at lower  $\Lambda$  values. For this point, the peaks are localized at the corners of the Brillouin zone, which is indicative of a Néel order.

Next, we analyze a point that exhibits the stripe order. For this purpose, we analyze the point labeled as St2 located at  $(\theta = 75^\circ, \phi = 14^\circ)$ . In Fig. 4.31, the susceptibility flow obtained from two-loop calculation (depicted in orange) appears to be mostly smooth down to  $\Lambda \rightarrow 0$ . This contrasts with the susceptibility flow obtained from one-loop calculation (shown in blue) that exhibits a local maximum around  $\Lambda/J \sim 0.2$ . However, upon examining the contour plot illustrated in Fig. 4.31 at  $\Lambda = 0.05$ , we note that the peaks are localized at the edges of the Brillouin zone, thus suggesting a stripe order.

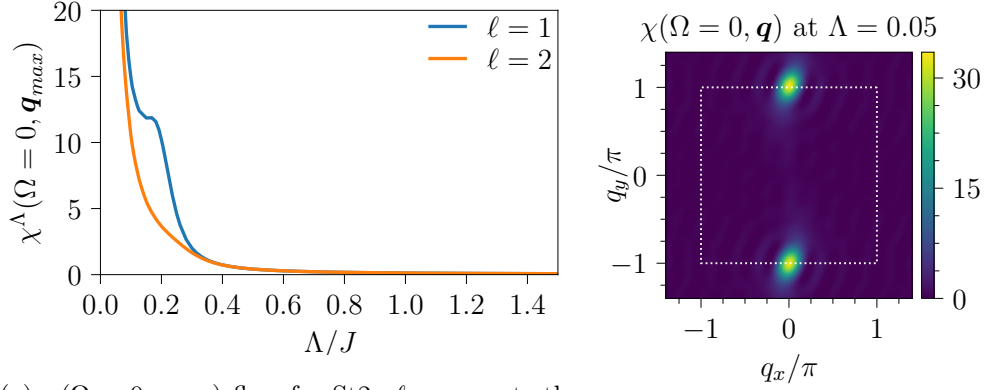
#### 4. Results



(a)  $\chi(\Omega = 0, \mathbf{q}_{max})$  flow for Ne2.  $\ell$  represents the loop order

(b)  $\chi(\mathbf{q})$  plot for Ne2

Figure 4.30: Plots for point Pm3,  $(\theta = 23^\circ, \phi = 20^\circ)$



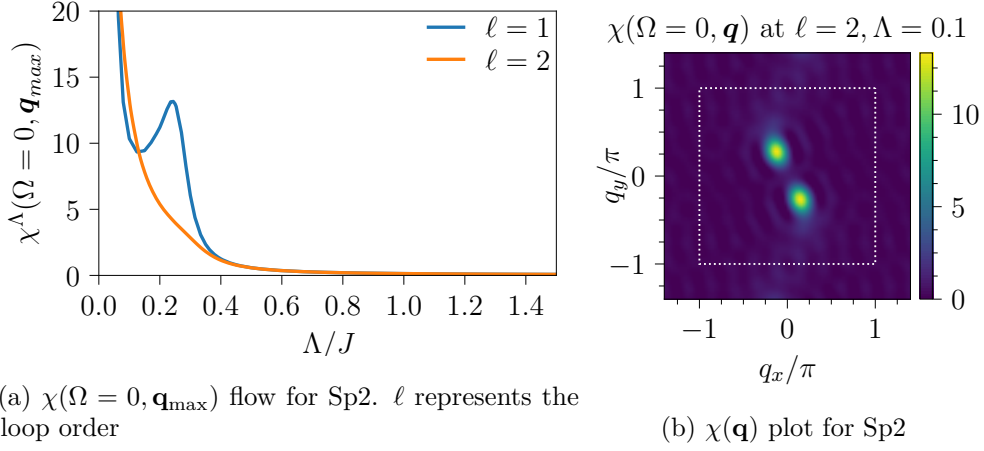
(a)  $\chi(\Omega = 0, \mathbf{q}_{max})$  flow for St2.  $\ell$  represents the loop order

(b)  $\chi(\mathbf{q})$  plot for St2

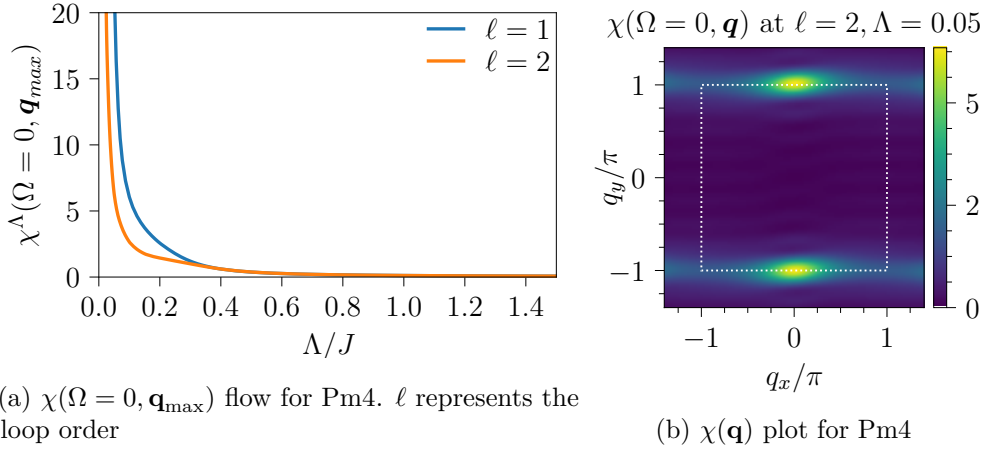
Figure 4.31: Plots for point St2,  $(\theta = 75^\circ, \phi = 14^\circ)$

The final example of an ordered phase is the spiral order. Specifically, we analyze the point labeled Sp2, which is situated at  $(\theta = 75^\circ, \phi = 30^\circ)$ . We once again focus on the flow of the susceptibility maximum. It's noticeable that the flow obtained from two-loop calculation is smooth down to  $\Lambda \rightarrow 0$  meanwhile in contrast the flow obtained from one-loop calculation has a local maximum around  $\Lambda/J \sim 0.3$ . Upon examining the contour plot in Fig. 4.32b at  $\Lambda/J = 0.1$ , it's apparent that the peaks are localized inside the Brillouin zone, indicative of a spiral order.

As an example of a paramagnetic phase, we choose to investigate the point Pm4 located at  $(\theta = 30^\circ, \phi = 10^\circ)$ . From Fig. 4.33a, we note that both the one-loop and two-loop susceptibility flows are smooth to lower  $\Lambda$  values. However, it's noteworthy that the two-loop susceptibility flow appears subdued in comparison to the one-loop susceptibility flow. Inspecting the contour plot in Fig. 4.33b, we observe peaks that appear smeared out around the edges

Figure 4.32: Plots for point Sp2,  $(\theta = 75^\circ, \phi = 30^\circ)$ 

of the Brillouin zone at  $\Lambda = 0.05$ . This point is therefore classified as a paramagnet, a finding that aligns with the one-loop calculation.

Figure 4.33: Plots for point Pm4,  $(\theta = 30^\circ, \phi = 10^\circ)$ 

### 4.3 Discussion

First, we consider the results obtained for the triangular lattice, considering both the next-nearest-neighbor interactions in Sec. 4.1.1 and the long-range interactions discussed in Sec. 4.1.2.

We employed NNN interactions on the triangular lattice to test our code and determine if we could accurately identify the phase boundaries in line with the pffRG literature [10]. Our findings revealed a narrower region around  $0.10 \lesssim \alpha \lesssim 0.25$  for the disordered phase. This aligns more closely with other methods such as DMRG [6, 8, 9] opposed to the previous pffRG calculations

[10]. Nonetheless, we still face challenges in precisely determining the phase boundary, as the methods employed in the literature for distinguishing phases within pffRG are limited to inspecting the fRG flow and contour plots.

In Sec. 4.1.2, we examined the results of one and two-loop calculations for long-range interactions on the triangular lattice. Unlike methods such as DMRG, which excel in shorter-range interactions and lower-dimensional systems, fRG is well-suited for simulating larger systems, making it an ideal approach for studying long-range interactions. Moreover, by employing the efficient vertex parametrization required for the multi-loop calculations, we can generate a more stable susceptibility flow compared to the existing literature.

In the first part of Sec. 4.1.2, we presented the one-loop calculation results for the triangular lattice, which are mostly in agreement with the work of Keles and Zhao [1]. Different from their work, we find a bigger paramagnetic regime spread through the phase boundary of spiral and stripe phase. However, as discussed in Sec. 4.1.2, distinguishing phases near the phase boundaries can be challenging. Thus, we abstain from drawing phase boundaries as we believe a more comprehensive investigation is required to precisely locate the phase transition points.

In the latter part of Sec. 4.1.2, we present our two-loop calculations for the same model. We did not observe any changes to the phase diagram. Due to the higher computational cost of the two-loop calculations, we had a limited number of sample points, and we did not scan the whole phase diagram.

In Sec. 4.2.1, we compared the phases we found from one-loop calculations for the NNN AFM Heisenberg model on the square lattice with existing literature [12–14, 18]. We found the magnetically disordered phase to be situated between  $0.50 \lesssim \alpha \lesssim 0.65$  which is narrower compared to the literature [12–14, 18]. Additionally, as we did not break the lattice symmetries, we were not able to confirm the existence of a VBS ground state. Since our main focus was on dipolar interactions, we used the NNN model as a test case.

In Sec. 4.2.2 we presented our one and two-loop calculations for the dipolar Heisenberg model on the square lattice. Our results agree with previous pffRG calculations conducted in Ref. [2], where a paramagnetic regime along the phase boundary of Néel phase was identified. Contrary to Ref. [2], we found another paramagnetic regime situated along the boundary of the stripe and the spiral phase. We confirmed this finding by examining the scaling of the susceptibility flow in this regime with lattice size. Nevertheless, a more detailed investigation is required to understand the extent of this paramagnetic regime.

Moreover, we also presented our two-loop calculations for the dipolar interactions. We did not observe any significant alternations to the phase boundaries. Due to the increased numerical cost of the two-loop calculations, we did not further pursue a more detailed scan of the phase diagram.

Overall, our one-loop calculations mostly agree with previous pffRG calculations in Ref. [1] for the triangular lattice and in Ref. [2] for the square lattice. In the two-loop calculations, the inclusion of new diagrams to the

flow equations resulted in a decrease in susceptibility for both geometries, which consequently rendered the susceptibility flow more smooth. However, we did not identify a novel phase or observe a significant shift in the phase boundaries. Furthermore, considering that the loop convergence in multi-loop fRG is not always guaranteed at a finite loop order, and considering that the computational cost scales linearly with the loop order, we chose not to pursue higher loop order computations. Additionally, given the recent publication by Schneider et al. [33], there is still a degree of uncertainty regarding the potential benefits and precision of higher loop order calculations.



## Benchmark

In Chapter 2 and in Chapter 3, we have discussed the construction and implementation of the mpffRG. Throughout these chapters, we have made use of certain approximations, in order to make mpffRG numerically feasible. These approximations, namely are the fulfillment of the pseudofermion constraint covered in Chapter 2.2.1, the parquet approximation covered in Chapter 2.2.3, the cutoff dependence of the flow equations examined in Chapter 2.2.5, the representation of the continuous Matsubara frequencies at  $T = 0$  with a discrete spectrum discussed in Chapter 3.1.5, the finite size truncation of the infinite lattice discussed in 3.1.4 and the truncation of the six-point vertex that corresponds to the one-loop mpffRG that is also a common practice in the literature. In the first section of this chapter, we will discuss the effects of these approximations on the calculations.

In the second part of this chapter, we benchmark pffRG by comparing it to DMRG and ED in their reliable domains. Differing from our previous approach for the NNN AFM Heisenberg model on the triangular and square lattice in Chapter 4, where we compared results obtained at the end of the flow, here, we compare the flow directly with other methods. To make this possible, we show that the cutoff function can be interpreted as a modification to the Hamiltonian as a coupling to a fermionic bath. Then, we simulate this modified Hamiltonian using DMRG and ED, and compare with the flow obtained from pffRG. Given that this is ongoing research, we share our preliminary findings at this stage.

### 5.1 Approximations of pffRG

In this section, we look at the approximations employed in the construction of mpffRG and its effects on the results. First, we will look briefly at the lattice size truncation and frequency discretization. Then we will look at the pseudofermion constraint and to what to what degree it is not satisfied. Then we will discuss the cutoff dependence which will be revisited again in the next second part of this chapter.

### 5.1.1 Lattice Size Truncation

In Chapter 3.1.4, we discussed how an infinite lattice could be approximated for pffRG calculations using a finite-sized lattice. The implications of this truncation were already explored in Chapter 4. We have discussed that the local maximum that scales with lattice sizes can be extrapolated to infinity in the thermodynamic limit. The scaling of these local maxima can be observed in Fig 4.4 and Fig. 4.21.

Moreover, we observed that larger lattice sizes may be necessary to accommodate various phases, as observed for the spiral phase in Sec. 4.2.2. We also observed that for the spiral phase, the critical  $\Lambda$  value shifted by lattice size yet the phase we find at the end of flow remained the same. An example of shifting of the local maximum can be seen in Fig. 4.23.

Furthermore, we have also observed that for the disordered phases where no breakdown occurs in the flow, we noted the absence of flow scalings can be seen in Fig. 4.28.

Therefore, we conclude that the truncation of the lattice size does not affect the end result obtained from the pffRG calculations but might influence the critical  $\Lambda$  value for certain phases.

### 5.1.2 Frequency Discretization

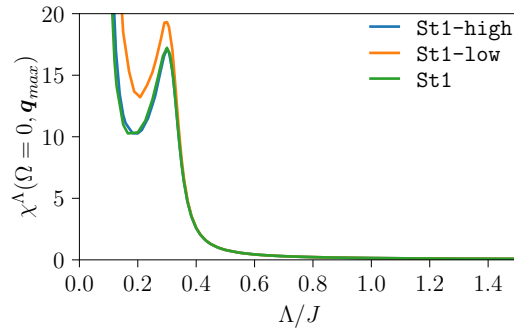


Figure 5.1: St1 point defined for the Heisenberg model with dipolar interactions on the triangular lattice with various frequency parameters.

The Matsubara frequencies at  $T = 0$  are a continuous spectrum. However, due to the discrete structure of computers, we cannot fully reproduce the frequency grid of this continuous spectrum. Instead, we sample discrete of this continuous spectrum and try to resolve fRG objects accurately. In Chapter 3.1.5 we briefly discussed the sampling procedure of this adaptive frequency grid which was implemented by Marc Ritter and Julian Thönniß. For the details of implementation, see Refs. [5, 24, 39].

For our calculations in Chapter 4 we have confirmed that increasing the frequency parameters from the current parameters does not affect the flow. Fig. 5.1 displays the St1 point results obtained from one-loop calculations of

the Heisenberg model with dipolar interactions on the triangular lattice using various frequency parameters. The green curve corresponds to the results obtained with the parameters used in Chapter 4, while the blue (orange) curve corresponds to the results obtained using higher (lower) frequency parameters. We observe that the behavior of the flow remains unchanged when the frequency parameters are increased.

### 5.1.3 Fulfillment of the Pseudofermion Constraint

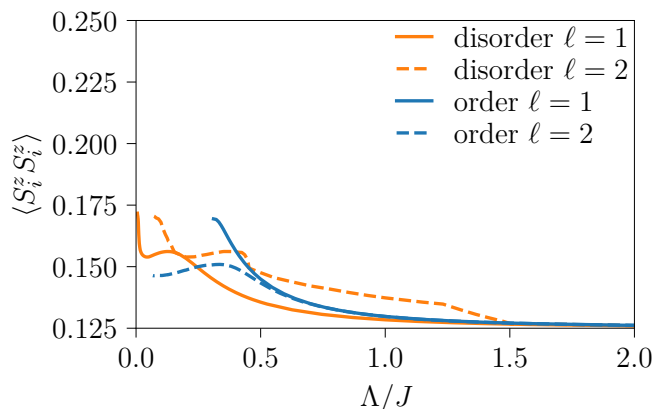


Figure 5.2: These results were obtained from the dipolar interactions on the triangular lattice. The disordered phase is at  $(\theta = 15, \phi = 10)$  and the ordered phase is at  $(\theta = 50, \phi = 5)$ . The blue (orange) line is the flow of the ordered (disordered) phase. The  $\ell$  represents the loop order. The pseudofermion constraint is fulfilled when  $\langle S_i^z S_i^z \rangle = 0.250$ .

In Chapter 2.2.1, we introduced the decomposition of spin operators to the fermionic language through pseudofermion creation and annihilation operators. However, this construction enlarges the Hilbert space by introducing unphysical states namely, unoccupied and doubly occupied states. We also discussed that this condition is fulfilled on average by setting the chemical potential to the particle-hole symmetric value [16].

A way to verify the fulfillment of this constraint is through examining the local equal-time spin-spin correlator [5, 24]. It is defined as follows:

$$\chi_{ii}^{zz}|_{\tau=0} = \langle S_i^z S_i^z \rangle. \quad (5.1)$$

For the unphysical sector of the Hilbert space  $\chi_{ii}^{zz}|_{\tau=0} = 0$ , while for the physical sector,  $\chi_{ii}^{zz}|_{\tau=0} = \frac{1}{4}$ . When the pffRG flow starts at  $\Lambda \rightarrow \infty$ , the physical and unphysical sector of the Hilbert space is equally populated, resulting in  $\chi_{ii}^{zz}|_{\tau=0} = \frac{1}{8}$ . However, when we recover the original system at  $\Lambda \rightarrow 0$  we expect the local equal-time spin-spin correlator to be populated by only the physical sector of the Hilbert space, hence  $\chi_{ii}^{zz}|_{\tau=0} = \frac{1}{4}$ .

Thönniß et al. highlighted the shortfall of the fulfillment of this constraint for the AFM Heisenberg model on kagome lattice [5] and Ritter highlighted it for the XXZ model on the pyrochlore lattice [24]. Most recently, Schneider et al. in Ref. [33] showed that at  $T = 0$  this constraint is not fulfilled for smaller systems such as trimer using exact diagonalization (ED).

In Fig. 5.2, we present the local equal-time spin-spin correlator obtained from various calculations presented in Chapter 4 for the long-range Heisenberg model on the triangular lattice. We observe that at the start of the flow the  $\chi_{ii}^{zz}|_{\tau=0}$  is around 0.125 just as expected. As the flow continues to  $\Lambda \rightarrow 0$ , the occupancy of the physical sector of the Hilbert space increases [5]. However, regardless of the phase and the loop order, the pseudofermion constraint is far from being fulfilled, which makes pffRG quantitatively less reliable.

### 5.1.4 Cutoff Dependence

In Chapter 2.2.5, we introduced a scale dependant cutoff to the bare Green's function. While the choice of cutoff is arbitrary, for  $\Lambda \rightarrow 0$ , one recovers the original physical theory. However, in practice, we observe that the flow might diverge before reaching  $\Lambda \rightarrow 0$ , preventing us from reaching the physical theory [33]. As demonstrated in Ref. [23], the choice of cutoff can influence the results of one-loop calculations for the x-ray edge singularity. Nevertheless, cutoff independence can be realized by achieving loop convergence in mfRG [23].

For the calculations in Chapter 4, we have employed the Gaussian cutoff function introduced in Eq. (2.25). To investigate the impact of cutoff dependency on our results, we replicated a calculation from the previous chapter, this time utilizing the Lorentzian cutoff introduced in Eq. (2.26). In Fig. 5.3, we present the results obtained for the stripe-ordered phase with both cutoff functions. The blue (orange) curve represents the Gaussian (Lorentzian) cutoff. The flow obtained from using the Lorentzian cutoff function suddenly diverges around  $\Lambda/J \sim 0.35$ . Meanwhile, the flow obtained from the Gaussian cutoff has a local maximum around  $\Lambda/J \sim 0.3$ , which, as previously discussed, scales with lattice size and can be extrapolated to infinity in the thermodynamic limit. Therefore, it is evident that both cutoff functions give rise to an ordered phase with slightly different critical  $\Lambda$ , but they generate quantitatively distinct flows. We will revisit cutoff dependence in the next section.

### 5.1.5 Parquet Approximation

In Chapter 2.2.3, we have discussed the parquet approximation. The SDE and BSEs form a set of self-consistent equations, given a choice of  $R$  as an input. The parquet approximation corresponds to the simplest choice  $R = \Gamma_0$ , ensuring that all diagrams up to the fourth order in perturbation series are included in this set of equations [20, 24]. At the fourth order, the so-called envelope diagram, which is irreducible in all three two-particle reducible

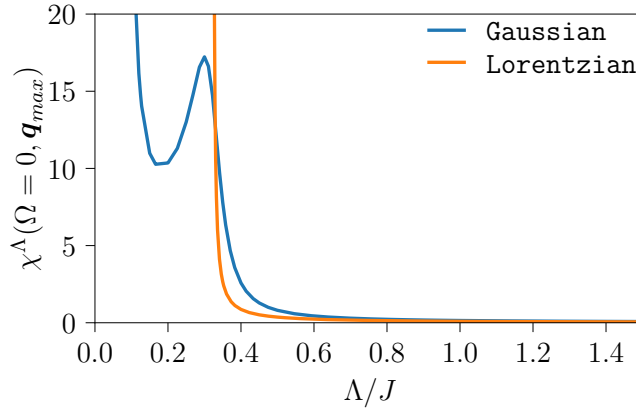


Figure 5.3: The one-loop flow for the dipolar Heisenberg interaction on a triangular lattice with  $(\theta = 50, \phi = 5)$ , calculated using two different cutoff functions, is represented here. The orange curve corresponds to the flow obtained with the Lorentzian cutoff, whereas the blue curve is obtained with the Gaussian cutoff.

channels, is missing. Since this diagram contains a double momentum integral, it is hard to compute numerically.

For a more non-trivial choice of  $R$  in the fRG treatment, obtaining the irreducible vertex using DMFT and using that irreducible vertex as an initial condition for the flow equations is possible. This method known as DMF<sup>2</sup>RG and more details can be found in Ref. [20].

The parquet approximation also allows us to generate all ladder diagrams and their combinations through iteration without any bias towards a single type of ladder. By incorporating these ladder diagrams, the parquet equations exceed the fourth-order perturbation theory [20].

An important property of the parquet equations is that they fulfill the Mermin-Wagner theorem, which states that there can be no long-range order at a finite temperature for 2D systems with short-range interactions [45]. The conventional one-loop fRG does not obey the Mermin-Wagner theorem. However, at  $\ell \rightarrow \infty$  mfRG is equivalent to the parquet equations. Therefore by achieving loop convergence in mfRG, one can fulfill the Mermin-Wagner theorem [23].

### 5.1.6 Truncation of Six-point Vertex

As previously discussed in Chapter 2.2.6, the conventional pffRG used in the literature [1, 2, 16, 18, 19, 25, 38] corresponds to the first loop order in our scheme. This approximation omits any contributions to the flow equations coming from the six-point vertex [20].

In a recent study by Schneider et al. [33], the one-loop pffRG, pffRG with Popov-Fedetov trick, and parquet equations (which corresponds to the mpffRG

with loop convergence) with Popov-Fedetov trick were compared to ED results obtained for the AFM Heisenberg model on the dimer and trimer. It was demonstrated that the truncation of the six-point vertex in the flow equations is an uncontrolled approximation in the high coupling regime.

To investigate the extent of validity of this approximation, we will compare the equal-time susceptibility flow obtained from pffRG to the equal-time susceptibility flow obtained from quantitatively more reliable methods such as DMRG and ED in one-dimensional systems in the next section.

## 5.2 Physical Interpretation of the Cutoff Function

In Chapter 2.2.5, we deformed the original theory by artificially introducing a cutoff function to the bare two-particle propagator and the original theory reinstated at the limit  $\Lambda \rightarrow 0$ . In this section, we aim to give physical meaning to the deformed theory by showing a correspondence between the cutoff function and coupling to a fermionic bath. To do this, we first consider the pseudofermion Hamiltonian, as given in Eq. (2.6), for the SU(2) symmetric Heisenberg model

$$H_{\text{sys}} = \frac{1}{8} \sum_{\alpha\beta\alpha'\beta'} \sum_{\mu} \sum_{ij} J_{ij} \sigma_{\alpha\beta}^{\mu} \sigma_{\alpha'\beta'}^{\mu} f_{i\alpha}^{\dagger} f_{j\beta} f_{j\alpha'}^{\dagger} f_{i\beta'}. \quad (5.2)$$

We will now proceed to couple the system's fermions with those present in the fermionic bath. The bath fermions are denoted by  $c_{i\alpha}$  where  $\alpha$  represents the spin index and  $i$  indicates the lattice site to which this bath is coupled. We establish the dynamics of these bath fermions by defining a coupling Hamiltonian and a bath Hamiltonian as follows:

$$H_{\text{hyb}} = \sum_{i\alpha k} [V_k f_{i\alpha}^{\dagger} c_{i\alpha k} + V_k^* c_{i\alpha k}^{\dagger} f_{i\alpha}], \quad (5.3)$$

$$H_{\text{bath}} = \sum_{i\alpha k} \epsilon_k c_{i\alpha k}^{\dagger} c_{i\alpha k}. \quad (5.4)$$

The full Hamiltonian of this modified theory becomes

$$H_{\text{mod}} = H_{\text{sys}} + H_{\text{bath}} + H_{\text{hyb}}. \quad (5.5)$$

$H_{\text{mod}}$  being non-interacting and quadratic in  $c$  fermions, allows us to integrate out the bath fermions within the path integral formalism, leading to the action of this modified theory to be,

$$S = \sum_1 \bar{\psi}_1 \left( -i\omega + \underbrace{\sum_k \frac{|V_k|^2}{i\omega - \epsilon_k}}_{\equiv \Delta(i\omega)} \right) \psi_1 - \frac{1}{4} \sum_{1',2';1,2} \Gamma_0(1',2';1,2) \bar{\psi}_1 \bar{\psi}_2 \psi_1 \psi_2. \quad (5.6)$$

Here we have adopted the multi-index notation from earlier chapters and defined the hybridization term  $\Delta(i\omega)$ . Unlike the pseudofermion action, we note that this action has a kinetic term. And this term modifies the bare Green's function as follows,

$$G_0(i\omega) = \frac{1}{i\omega - \Delta(i\omega)}. \quad (5.7)$$

We observe that the new Green's function has the same form of an additive cutoff described in Eq. (2.27),

$$G_0^{-1,\Lambda} = i\omega - \Delta^\Lambda(i\omega). \quad (5.8)$$

Hence, a cutoff function, as in Eq. (2.27), can be understood as a coupling to a fermionic bath. The selection of the cutoff function dictates the Hamiltonian of this newly deformed theory.

Since we employ multiplicative cutoffs in our approach, we can also identify a correspondence between them and to the coupling of fermionic baths.

For the multiplicative Gaussian cutoff described in Eq. (2.25) we have the following correspondence,

$$G_0^{-1,\Lambda} = \frac{i\omega}{\Theta^\Lambda(\omega)} = \frac{i\omega}{1 - e^{-\omega^2/\Lambda^2}} = i\omega + \frac{i\omega}{e^{\omega^2/\Lambda^2} - 1}. \quad (5.9)$$

This means that the Gaussian cutoff is equivalent to a hybridization of the form,

$$\Delta^\Lambda(i\omega) = \frac{-i\omega}{e^{\omega^2/\Lambda^2} - 1}. \quad (5.10)$$

Similarly, for the multiplicative Lorentzian cutoff described in Eq. (2.26) we have,

$$G_0^{-1,\Lambda} = \frac{i\omega}{\Theta^\Lambda(\omega)} = i\omega \frac{\omega^2 + \Lambda^2}{\omega^2} = i\omega + i \frac{\Lambda^2}{\omega}. \quad (5.11)$$

This means that the Lorentzian cutoff is equivalent to a hybridization of the form,

$$\Delta^\Lambda(\omega) = \frac{\Lambda^2}{\omega}. \quad (5.12)$$

Hence, the multiplicative Lorentzian cutoff is equivalent to a Hamiltonian where the system couples to a fermionic bath with  $\epsilon_k = 0$  and the coupling strength controlled by  $\Lambda = V$ .

## 5. Benchmark

---

	$n_\Omega$	$n_\mu$	$n'_\mu$
$\Sigma(\Omega)$	4000	-	-
$\mathcal{K}_1$	400	-	-
$\mathcal{K}_2$	100	100	-
$\mathcal{K}_{2'}$	100	-	100
$\mathcal{K}_3$	80	80	80

Table 5.1: Frequency parameters for the AFM Heisenberg dimer

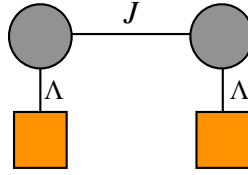


Figure 5.4: Illustration of the dimer coupled to non-interacting fermionic baths.

### 5.3 Dimer

To assess the pffRG flow's reliability, we examine the AFM Heisenberg dimer model. The dimer model is a simple model with only two interacting spins. Hence, the Hamiltonian for the dimer Hamiltonian contains only two spin operators and it can be written as

$$H_{\text{dimer}} = J \mathbf{S}_1 \cdot \mathbf{S}_2, \quad (5.13)$$

where  $J > 0$  for. Since it is a fairly simple model, it can be solved exactly using ED. However, as we use the Lorentzian cutoff for solving this model in pffRG, for ED treatment we need to address a larger system that includes coupling to fermionic baths. Nonetheless, solving this extended system is still manageable with ED.

Now, the flow parameter  $\Lambda$  can be interpreted as the coupling strength between the fermionic baths and the system fermions. In the limit  $\Lambda \rightarrow 0$  the bath fermions are decoupled from the system fermions, and the original system is recovered. On the other hand, in the high  $\Lambda$  limit, the systems fermions become non-interacting, and only the coupling between the bath and system fermions become relevant.

Before proceeding with the comparison of the two methods, it is important to highlight an unexpected divergence of the pffRG flow around  $\Lambda/J \sim 0.2$ . This divergence of the flow is illustrated in Fig. 5.5. We suspect that at  $\Lambda/J = 0.2$  there might be a phase transition where the system fermions form a singlet state. However, further investigation is needed to fully understand the nature of this breakdown, as the research is still ongoing.

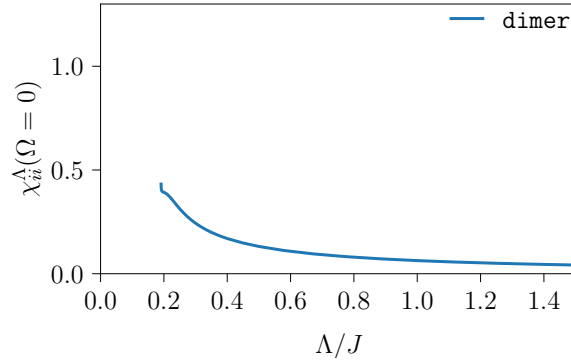


Figure 5.5: The static susceptibility flow of the dimer using the Lorentzian cutoff. We observe a break-down of the flow around  $\Lambda/J \sim 0.2$ .

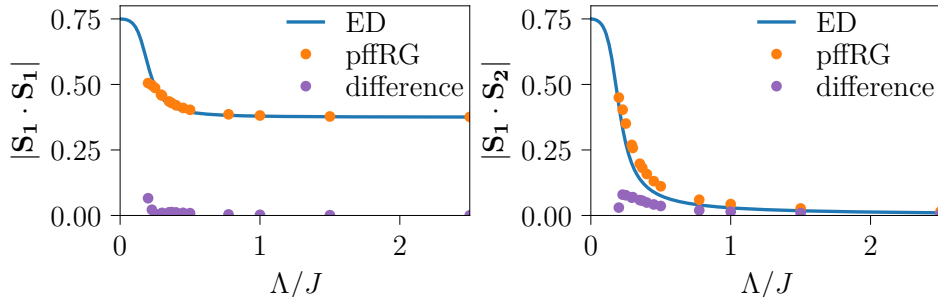


Figure 5.6: The equal-time susceptibility flow obtained from pffRG is shown in orange, while the flow obtained from ED is shown in blue. The absolute difference between the two methods is depicted in purple. On the left, the on-site equal time susceptibility is depicted, and on the right, the equal time susceptibility of two neighboring sites is shown. It is observed that at the weak coupling limit, the absolute difference is small but scales, as we approach to lower  $\Lambda$  limit the absolute difference increases.

Next, we compare the equal-time susceptibility flow obtained from pffRG and ED for various values of  $\Lambda$ . In Fig. 5.6, the zero-time susceptibility flow is illustrated for the onsite correlation  $|\mathbf{S}_1 \cdot \mathbf{S}_1|$  in the first row and for neighboring sites  $|\mathbf{S}_1 \cdot \mathbf{S}_2|$  in the second row. In Fig. 5.6, the orange dots represent the pffRG results, the blue line is the exact result obtained from ED, and the purple dots are the absolute error.

We observe that at the start of the flow, in both methods, the onsite correlation is  $|\mathbf{S}_1 \cdot \mathbf{S}_1| = 0.375$ . This is because, at the high  $\Lambda$  limit, the probability of finding a double occupancy of a site equals the probability of finding a single occupancy of a site. On the other hand, in the high  $\Lambda$  limit, the correlation of neighboring sites is  $|\mathbf{S}_1 \cdot \mathbf{S}_2| = 0$  as the system fermions are decoupled. However, with decreasing  $\Lambda$  values, the system fermions become more and more correlated, resulting in an increase in the absolute value of

## 5. Benchmark

---

correlation functions. For ED, at  $\Lambda = 0$ , this value reaches to 0.75, which is the exact value when two neighboring spins are aligned, and there are no contributions from bath fermions.

Consistent with our expectations, we observe that as the flow goes to the high coupling limit the difference between the ED and pffRG value increases with fRG flow.

### 5.4 Infinite Chain

	$n_\Omega$	$n_\mu$	$n'_\mu$
$\Sigma(\Omega)$	4000	-	-
$\mathcal{K}_1$	400	-	-
$\mathcal{K}_2$	100	80	-
$\mathcal{K}_{2'}$	100	-	80
$\mathcal{K}_3$	40	40	40

Table 5.2: Frequency parameters for the AFM Heisenberg chain.  $r_{\text{cutoff}} = 60$

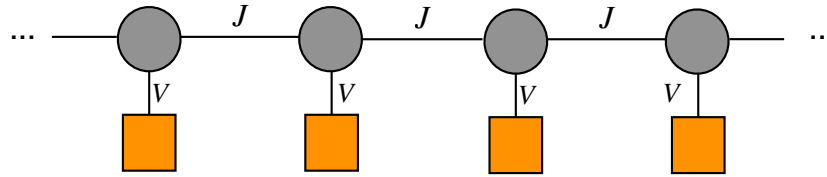


Figure 5.7: Illustration of the infinite chain coupled to non-interacting fermionic baths.

As for a second test for pffRG, we consider another one-dimensional model, the Heisenberg infinite chain with AFM NN interactions. The Hamiltonian of this model is defined as:

$$H = J \sum_i \mathbf{S}_i \cdot \mathbf{S}_{i+1}. \quad (5.14)$$

where  $J$  is positive for AFM interactions. In our calculations, we set  $J = 1$  for simplicity. For spin 1/2 systems, this model has a gapless energy spectrum and has no magnetic order at  $T = 0$  [46].

To benchmark pffRG with DMRG, we again employ the multiplicative Lorentzian cutoff for our pffRG treatment. Therefore, in the DMRG calculations, we solve a modified Hamiltonian where each system site is coupled to a non-interacting fermionic bath. The DMRG data for this project is generated by our group member Andreas Gleis, using a total of 200 spin sites with open boundary conditions. Although the system solved by DMRG is not an infinite

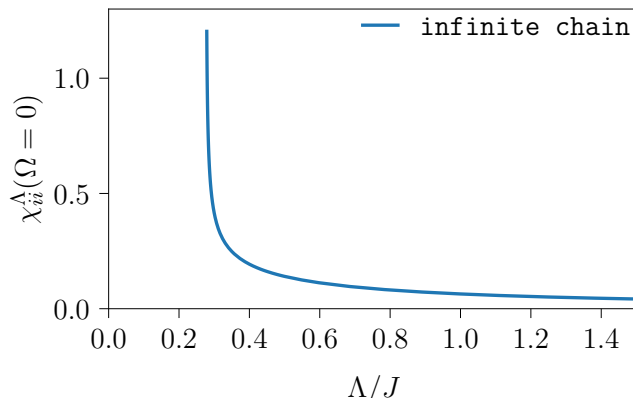


Figure 5.8: Static susceptibility flow of AFM Heisenberg chain obtained from pffRG with Lorentzian cutoff.

chain, open boundary effects should be negligible for the spins in the center of the chain.

In Fig. 5.8, we present the susceptibility flow obtained from pffRG calculations. We observe that the flow exhibits a divergence at  $\Lambda \sim 0.27$ . Typically, a divergence in the susceptibility flow indicates a phase transition. However, such a phase transition is unexpected for the one-dimensional AFM Heisenberg chain, which has no ordered ground state. Similarly, in the DMRG calculations, we have observed a phase transition around  $\Lambda \sim 0.2$ , determined by analyzing the scaling of equal-time correlations at different  $\Lambda$  values. This suggests that the phase transition is influenced by the coupling to the fermionic bath. Further investigation is required to understand the nature of this phase transition.

We benchmark the two methods by comparing the equal-time susceptibility in real space at a given  $\Lambda$  centered around the 100th lattice site. In Fig. 5.9, the equal-time susceptibility obtained from pffRG (DMRG) is depicted in blue (orange). We investigate the equal-time susceptibility at  $\Lambda = 1$  in the top row and at  $\Lambda = 0.5$  in the bottom row. The plots on the left present the data in linear scale, while the plots on the right display the data in log-log scale to observe the scaling behavior.

We observe a good agreement between both methods for  $\Lambda = 1$  and  $\Lambda = 0.5$ . This indicated that pffRG is reliable in the regime around  $\Lambda \sim 0.5$ . However, as discussed above, the pffRG flow diverges around  $\Lambda \sim 0.27$ , preventing us from reaching smaller  $\Lambda$  values.

The ground state of the AFM Heisenberg chain with NNN interactions differs significantly from the NN interactions. While for the NN interactions, there is no magnetically ordered ground state, for the NNN interactions there is a phase transition from magnetically disordered phase to a dimer state at  $J_2/J_1 \equiv \alpha > 0.24$  [47]. In an attempt to reach lower  $\Lambda$  values, we try to utilize the competition between these two phases. We present the flow obtained from

## 5. Benchmark

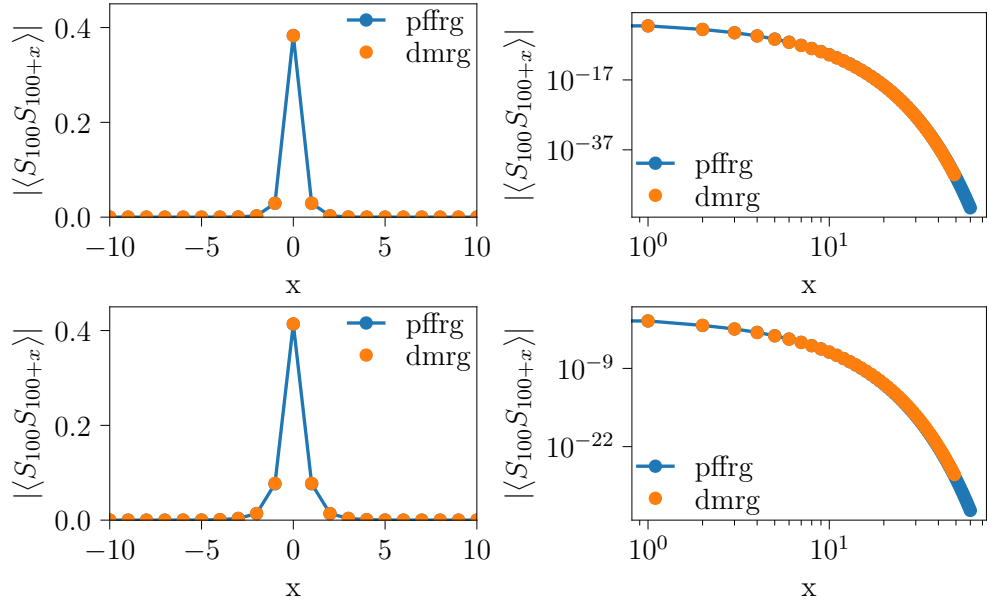


Figure 5.9: Equal-time susceptibility comparison between pffRG and DMRG in real space centered around 100th lattice site at  $\Lambda = 1$  in the first row, and at  $\Lambda = 0.5$  in the second row. The blue (orange) points represent results obtained from pffRG (DMRG).

pffRG for different values  $\alpha$  in Fig. 5.10a. Although we were able to reach lower  $\Lambda$  values with NNN, they are not significantly lower. As a result, we did not produce DMRG data to assess the reliability of pffRG using NNN interactions.

Since pffRG is mainly used for higher dimensional systems, benchmarking the equal-time susceptibility with higher dimensional models can be useful. We investigated coupled AFM Heisenberg chains on a cylinder using periodic boundary conditions along one direction as described in Chapter 3.1.4. We constructed the cylinder by coupling 3 and 4 chains along this direction as well as infinite coupled chains which corresponds to the square lattice. The static susceptibility flow of these coupled chains is illustrated in Fig. 5.10b. We again observe that the static susceptibility diverges at a critical  $\Lambda$ . However, we observe that this critical value increases with the number of coupled chains. The nature of this phase transition is still under investigation. Thus, we did not yet generate data from DMRG to compare with our pffRG results.

Lastly, we revisit the cutoff dependence discussed in Sec. 5.1.4. We test the two different cutoff functions utilized throughout this thesis for the Heisenberg chain with AFM NN interactions. In Fig. 5.11, we present the static susceptibility flow obtained by using the Gaussian cutoff in blue and the Lorentzian cutoff in orange. We note that the flow obtained from the Gaussian cutoff has a smooth flow up to  $\Lambda \rightarrow 0$ , indicating a magnetically disordered phase. On

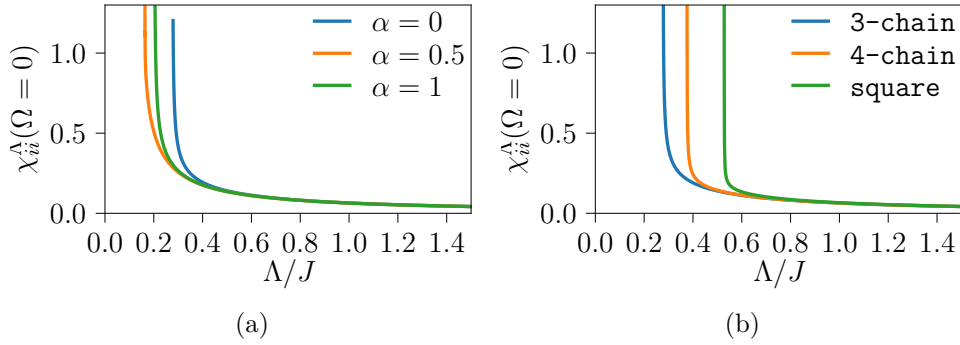


Figure 5.10: The static susceptibility flow obtained by pffRG with the Lorentzian cutoff. On the right, NNN interactions for various values of  $\alpha$  are represented. On the left, coupled chains on a cylinder with different numbers of chains are represented.

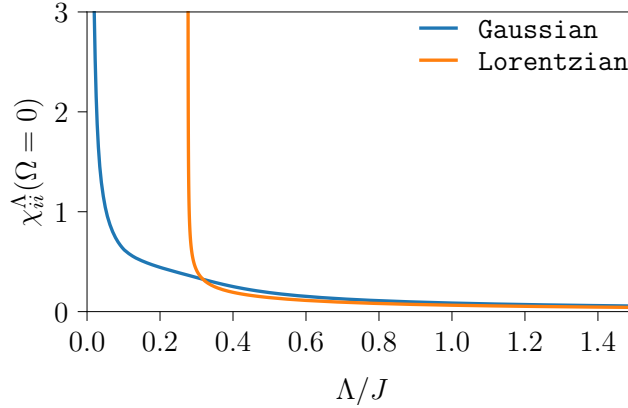


Figure 5.11: The static susceptibility flow of AFM Heisenberg chain with NN obtained by using two different cutoffs. The orange curve represents the flow obtained by employing the Lorentzian cutoff and the blue curve represents the flow obtained by employing the Gaussian cutoff.

the other hand, as discussed, the flow of the static susceptibility obtained by employing the Lorentzian cutoff diverges around  $\Lambda \sim 0.27$  indicating a phase transition to a magnetically ordered phase. This comparison highlights the significant impact of the choice of cutoff on the behavior of the susceptibility flow and the interpretation of the phase found at the end of the flow.

## 5.5 Discussion

In the first part of this chapter, we have examined the different approximations utilized in the construction of mpffRG. We have observed that the pseudofermion constraint is not fulfilled by checking the on-site equal-time susceptibility [5, 24, 33]. Furthermore, our analysis has revealed that the

choice of cutoff can significantly impact the behavior of the susceptibility flow in the first loop order, in agreement with previous findings in Ref. [23].

In the second part of this chapter, we showed that the cutoff function can be interpreted as a coupling to a fermionic bath. We discussed that the multiplicative Lorentzian cutoff corresponds to an impurity-like Hamiltonian, which can be reliably solved by ED for small systems and DMRG for large systems in one dimension. This allowed us to compare the results obtained from pffRG with those from well-established numerical techniques in one dimension.

In the later parts of this chapter, we conducted a benchmark study of pffRG with ED by solving the dimer and with DMRG by solving the infinite chain. We observed that at around  $\Lambda/J = 0.5$ , pffRG results agree well with both methods. For the dimer model, we were able to reach lower  $\Lambda$  values, where we observed that the absolute difference between the two methods increased as  $\Lambda$  decreased. For the infinite chain, we observed an unexpected phase transition at around  $\Lambda \sim 0.27$ , which is also confirmed by DMRG calculations. The nature of this phase transition is still being investigated. Additionally, at the end of this chapter, we revisited the impact of the cutoff choice on the static susceptibility flow. For the infinite AFM Heisenberg chain, we found that the choice of cutoff function led to a drastic change in the behavior of the susceptibility flow.

In conclusion, pffRG can be used as a reliable tool in the weak coupling regime, even for low-dimensional systems. However, we have observed that pffRG results deviate from reliable results in the high coupling limit. Further investigation is required to understand more precisely the domain of reliability of pffRG.

On the other hand, pffRG can simulate larger systems with long-range interactions where other methods fail. Thus, we believe that pffRG can be utilized as a valuable tool for exploring the general behavior of a system, although it may not provide exact results in all cases.

## Summary and Outlook

In this thesis, we employed the multiloop pseudofermion functional renormalization group to investigate the Heisenberg model with antiferromagnetic next-nearest-neighbor interactions and dipolar interactions on the triangular and square lattice. Our one-loop pseudofermion functional renormalization group results for the next-nearest-neighbor interactions on both geometries were compared to previous studies [6–10, 12–15]. Our findings revealed a slightly larger paramagnetic regime for the triangular lattice compared to Refs. [6–10] and a slightly smaller paramagnetic regime for the square lattice compared to Refs. [12–15]. Additionally, we compared our one-loop results for the dipolar interactions with another pseudofermion functional renormalization group study by Keles and Zhao [1, 2]. Our results are mostly in agreement with their study. However, we identified an extended paramagnetic regime spread throughout the phase diagram, which was absent in their work. Furthermore, we extended our analysis to the second loop order calculations for both geometries, but this did not result in significant changes to the phase diagram.

In the second part of this thesis, we conducted a benchmark study to assess the reliability of the pseudofermion functional renormalization group method. We devised a correspondence between the cutoff procedure in the functional renormalization group formalism to an impurity-like Hamiltonian. We compared our results with the exact diagonalization by solving the antiferromagnetic Heisenberg dimer and with the density matrix renormalization group by solving the antiferromagnetic Heisenberg infinite chain. Our findings demonstrated good agreement between the pseudofermion functional renormalization group and these numerical methods in the weak coupling limit. However, we observed an increasing absolute difference between the pseudofermion functional renormalization group and exact diagonalization results in the high coupling limit for the dimer. Additionally, we discovered an unexpected phase transition for the antiferromagnetic infinite chain which is also confirmed by the density matrix renormalization group. Further investigation is needed to fully understand the nature of this phase transition.

To better understand the domain of reliability of the pseudofermion functional renormalization group, we suggest conducting more benchmark studies and exploring different correspondences between the cutoff function and reliably solvable Hamiltonians. Extending this research to higher dimensions would also be beneficial, as the pseudofermion functional renormalization group is commonly used for two and three-dimensional systems. At this stage, we believe that the pseudofermion functional renormalization group is a valuable tool that can simulate large systems with long-range interactions and can be used to understand the general behavior of a system.

Another way to generalize our work would be to implement the Popov-Fedetov trick for finite temperatures [32, 33]. Schneider et al. [33] showed that at finite temperatures in contrast to the zero-temperature, the pseudofermion constraint is fulfilled. By incorporating the Popov-Fedetov trick, the pseudofermion functional renormalization group can provide more quantitatively reliable data for systems at finite temperatures. However, implementing this trick would require breaking some of the symmetries used in the parametrization of Green's functions.

---

## Bibliography

- [1] A. Keleş and E. Zhao, “Absence of long-range order in a triangular spin system with dipolar interactions”, [Physical Review Letters](#) **120**, 187202 (2018).
- [2] A. Keleş and E. Zhao, “Renormalization group analysis of dipolar heisenberg model on square lattice”, [Physical Review B](#) **97**, 245105 (2018).
- [3] L. Savary and L. Balents, “Quantum spin liquids: a review”, [Reports on Progress in Physics](#) **80**, 016502 (2017).
- [4] J. Thoenniss, “Multiloop functional renormalization group studies of heisenberg models on the kagome lattice”, Master’s Thesis (Ludwig-Maximilians-Universität München, Munich, Sept. 12, 2019).
- [5] J. Thoenniss, M. K. Ritter, F. B. Kugler, J. von Delft, and M. Punk, “Multiloop pseudofermion functional renormalization for quantum spin systems: application to the spin-1/2 kagome heisenberg model”, (2020), [arXiv:2011.01268\[cond-mat\]](#).
- [6] M. Drescher, L. Vanderstraeten, R. Moessner, and F. Pollmann, “Dynamical signatures of symmetry broken and liquid phases in an  $s=1/2$  heisenberg antiferromagnet on the triangular lattice”, (2022), [arXiv:2209.03344\[cond-mat\]](#).
- [7] S. Hu, W. Zhu, S. Eggert, and Y.-C. He, “Dirac spin liquid on the spin-1/2 triangular heisenberg antiferromagnet”, [Physical Review Letters](#) **123**, 207203 (2019).
- [8] W.-J. Hu, S.-S. Gong, W. Zhu, and D. N. Sheng, “Competing spin-liquid states in the spin- 1/2 heisenberg model on the triangular lattice”, [Physical Review B](#) **92**, 140403 (2015).
- [9] Z. Zhu and S. R. White, “Spin liquid phase of the  $s = 1/2$   $j_1$   $j_2$  heisenberg model on the triangular lattice”, [Physical Review B](#) **92**, 041105 (2015).

- [10] Y. Iqbal, W.-J. Hu, R. Thomale, D. Poilblanc, and F. Becca, “Spin liquid nature in the heisenberg  $j_1 - j_2$  triangular antiferromagnet”, [Physical Review B](#) **93**, 144411 (2016).
- [11] N. Y. Yao, M. P. Zaletel, D. M. Stamper-Kurn, and A. Vishwanath, “A quantum dipolar spin liquid”, [Nature Physics](#) **14**, 405 (2018).
- [12] S.-S. Gong, W. Zhu, D. N. Sheng, O. I. Motrunich, and M. P. A. Fisher, “Plaquette ordered phase and quantum phase diagram in the spin-  $1/2$   $j_1 - j_2$  square heisenberg model”, [Physical Review Letters](#) **113**, 027201 (2014).
- [13] H.-C. Jiang, H. Yao, and L. Balents, “Spin liquid ground state of the spin-  $1/2$  square  $j_1 - j_2$  heisenberg model”, [Physical Review B](#) **86**, 024424 (2012).
- [14] W.-Y. Liu, S.-S. Gong, Y.-B. Li, D. Poilblanc, W.-Q. Chen, and Z.-C. Gu, “Gapless quantum spin liquid and global phase diagram of the spin- $1/2$   $j_1 - j_2$  square antiferromagnetic heisenberg model”, [Science Bulletin](#) **67**, 1034 (2022).
- [15] J. Richter and J. Schulenburg, “The spin- $1/2$   $j_1 - j_2$  heisenberg antiferromagnet on the square lattice: exact diagonalization for  $n=40$  spins”, [The European Physical Journal B](#) **73**, 117 (2010).
- [16] J. Reuther and P. Wölfle, “ $J_1 - J_2$  frustrated two-dimensional heisenberg model: random phase approximation and functional renormalization group”, [Physical Review B](#) **81**, 144410 (2010).
- [17] H. Zou, E. Zhao, and W. V. Liu, “Frustrated magnetism of dipolar molecules on a square optical lattice: prediction of a quantum paramagnetic ground state”, [Physical Review Letters](#) **119**, 050401 (2017).
- [18] J. Reuther, “Frustrated quantum heisenberg antiferromagnets: functional renormalization-group approach in auxiliary-fermion representation”, PhD thesis (Karlsruher Institut für Technologie (KIT), Apr. 15, 2011).
- [19] J. Reuther and R. Thomale, “Functional renormalization group for the anisotropic triangular antiferromagnet”, [Physical Review B](#) **83**, 024402 (2011).
- [20] F. B. Kugler and J. V. Delft, “Derivation of exact flow equations from the self-consistent parquet relations”, [New Journal of Physics](#) **20**, 123029 (2018).
- [21] F. B. Kugler, “Renormalization group approaches to strongly correlated electron systems”, PhD thesis (Ludwig-Maximilians-Universität München, Munich, Aug. 13, 2019).
- [22] F. B. Kugler and J. von Delft, “Multiloop functional renormalization group for general models”, [Physical Review B](#) **97**, 035162 (2018).

- 
- [23] F. B. Kugler and J. Von Delft, “Multiloop functional renormalization group that sums up all parquet diagrams”, [Physical Review Letters](#) **120**, 057403 (2018).
- [24] Marc K. Ritter, “Multiloop pseudofermion functional renormalization group study of the pyrochlore XXZ model”, Master’s Thesis (Ludwig-Maximilians-Universität München, Munich, May 15, 2021).
- [25] Y. Iqbal, T. Müller, P. Ghosh, M. J. P. Gingras, H. O. Jeschke, S. Rachel, J. Reuther, and R. Thomale, “Quantum and classical phases of the pyrochlore heisenberg model with competing interactions”, [Physical Review X](#) **9**, 011005 (2019).
- [26] A. Kitaev, “Fault-tolerant quantum computation by anyons”, [Annals of Physics](#) **303**, 2 (2003).
- [27] A. Kitaev, “Anyons in an exactly solved model and beyond”, [Annals of Physics](#) **321**, 2 (2006).
- [28] P. W. Anderson, “Resonating valence bonds a new kind of insulator?”, *Mater. Res. Bull.* **8**, 153.
- [29] F. A. Palm, “Renormalization group studies of quantum phase transitions in the heisenberg-kitaev model on the triangular lattice”, Master’s Thesis (Ludwig-Maximilians-Universität München, Munich, Oct. 3, 2020).
- [30] L. Balents, “Spin liquids in frustrated magnets”, [Nature](#) **464**, 199 (2010).
- [31] A. A. Abrikosov, “Electron scattering on magnetic impurities in metals and anomalous resistivity effects”, [Physics Physique Fizika](#) **2**, 5 (1965).
- [32] V. N. Popov and S. A. Fedotov, “The functional-integration method and diagram technique for spin systems”, *Zh. Eksp. Teor. Fiz* **94** (1988).
- [33] B. Schneider, D. Kiese, and B. Sbierski, “Taming pseudofermion functional renormalization for quantum spins: finite temperatures and the popov-fedotov trick”, [Physical Review B](#) **106**, 235113 (2022).
- [34] P. Kopietz, L. Bartosch, and F. Schütz, *Introduction to the functional renormalization group*, Vol. 798, Lecture Notes in Physics (Springer Berlin Heidelberg, Berlin, Heidelberg, 2010).
- [35] M. Kardar, *Statistical physics of fields* (Cambridge University Press, June 2012).
- [36] B. Sbierski, “Condensed matter many-body physics and field theory II (TMP-TA 4), lecture notes”.
- [37] A. A. Katanin, “Fulfillment of ward identities in the functional renormalization group approach”, [Physical Review B](#) **70**, 115109 (2004).
- [38] A. Keleş and E. Zhao, “Rise and fall of plaquette order in the shastry-sutherland magnet revealed by pseudofermion functional renormalization group”, [Physical Review B](#) **105**, L041115 (2022).

- [39] M. K. Ritter, D. Kiese, T. Müller, F. B. Kugler, R. Thomale, S. Trebst, and J. von Delft, “Benchmark calculations of multiloop pseudofermion fRG”, [The European Physical Journal B](#) **95**, 102 (2022).
- [40] D. Skinner, “Quantum field theory II, lecture notes”.
- [41] F. L. Buessen, “A functional renormalization group perspective on quantum spin liquids in three-dimensional frustrated magnets”, PhD thesis (University of Cologne, Cologne, Aug. 23, 2019).
- [42] F. L. Buessen, V. Noculak, S. Trebst, and J. Reuther, “Functional renormalization group for frustrated magnets with nondiagonal spin interactions”, [Physical Review B](#) **100**, 125164 (2019).
- [43] I. Affleck, Z. Zou, T. Hsu, and P. W. Anderson, “SU(2) gauge symmetry of the large-  $u$  limit of the hubbard model”, [Physical Review B](#) **38**, 745 (1988).
- [44] N. Wentzell, G. Li, A. Tagliavini, C. Taranto, G. Rohringer, K. Held, A. Toschi, and S. Andergassen, “High-frequency asymptotics of the vertex function: diagrammatic parametrization and algorithmic implementation”, [Physical Review B](#) **102**, 085106 (2020).
- [45] N. D. Mermin and H. Wagner, “Absence of ferromagnetism or antiferromagnetism in one- or two-dimensional isotropic heisenberg models”, [Physical Review Letters](#) **17**, 1133 (1966).
- [46] A. Altland and B. D. Simons, *Condensed matter field theory*, 2nd ed. (Cambridge University Press, Cambridge, 2010).
- [47] K. Okamoto and K. Nomura, “Fluid-dimer critical point in  $s = 1/2$  antiferromagnetic heisenberg chain with next nearest neighbor interactions”, [Physics Letters A](#) **169**, 433 (1992).

**Declaration:**

I hereby declare that this thesis is my own work and that I have not used any sources and aids other than those stated in the thesis.

München, 22.06.2023

Gün Günal